Adaptive Optics for Laser Processing

Rainer Johannes Beck

A dissertation submitted for the degree of Doctor of Philosophy

Heriot-Watt University

School of Engineering and Physical Sciences

October 2011

This copy of the thesis has been supplied on condition that anyone who consults it is understood to recognise that the copyright rests with its author and that no quotation from the thesis and no information derived from it may be published without the prior written consent of the author or of the University (as may be appropriate).

Abstract

The overall aim of the work presented in this thesis is to develop an adaptive optics (AO) technique for application to laser-based manufacturing processes. The Gaussian beam shape typically coming from a laser is not always ideal for laser machining. Wavefront modulators, such as deformable mirrors (DM) and liquid crystal spatial light modulators (SLM), enable the generation of a variety of beam shapes and furthermore offer the ability to alter the beam shape during the actual process.

The benefits of modifying the Gaussian beam shape by means of a deformable mirror towards a square flat top profile for nanosecond laser marking and towards a ring shape intensity distribution for millisecond laser drilling are presented. Limitations of the beam shaping capabilities of DM are discussed.

The application of a spatial light modulator to nanosecond laser micromachining is demonstrated for the first time. Heat sinking is introduced to increase the power handling capabilities. Controllable complex beam shapes can be generated with sufficient intensity for direct laser marking. Conventional SLM devices suffer from flickering and hence a process synchronisation is introduced to compensate for its impact on the laser machining result. For alternative SLM devices this novel technique can be beneficial when fast changes of the beam shape during the laser machining are required. The dynamic nature of SLMs is utilised to improve the marking quality by reducing the inherent speckle distribution of the generated beam shape. In addition, adaptive feedback on the intensity distribution can further improve the quality of the laser machining.

In general, beam shaping by means of AO devices enables an increased flexibility and an improved process control, and thus has a significant potential to be used in laser materials processing.

Dedication

This thesis is dedicated to:

Diese Dissertation is gewidmet an:

Hans Thoma (1926 – 1999)

and / und

Josef Beck (1934 – 1993)

Acknowledgements

In particular, I would like to thank Professor Duncan Hand for his supervision and guidance throughout the course of this project. Special thanks goes to Dr Jon Shephard, Dr Jon Parry, Dr Andrew Waddie and Dr Robert Maier for their support and contribution. I would like to say thank you to all the members of the Applied Optics and Photonics research group, to other colleagues, and the technical and support staff at Heriot-Watt University. Special thanks must go to Renishaw plc, in particularly to Dr Nick Weston, for their funding, support and input to this project.

Many thanks to Stefan Osten from Holoeye for his product support, to BAE Systems, via Mike Griffith, for providing us with their bimorph mirror, to Hamamatsu, via Dr Raymond Livingstone, and to Boulder Nonlinear Systems, via Kelly Gregoriak, for providing us with a demonstration SLM unit.

My most profound thanks goes to my parents Regina and Alfred for everything they ever did for me. Special thanks goes to my sister Nicole and my grandmothers Katharina and Magdalena for all their continual assistance.

Finally, I would like to thank deeply all my mates including the ‘warden family’ – too many to specify – for all their support and the wonderful time so far and in the future.

Ich bedanke mich von ganzem Herzen bei meinen Eltern Regina und Alfred für alles, was sie bisher für mich getan haben. Ein besonderes Dankeschön gilt meiner Schwester Nicole und meinen Großmüttern Katharina und Magdalena für ihre Unterstützung.

Schließlich möchte ich mich ganz herzlich bei all meinen Freunden – zu viele um sie namentlich aufzuzählen – für die tolle gemeinsame Zeit bisher und zukünftig bedanken.

ACADEMIC REGISTRY
Research Thesis Submission

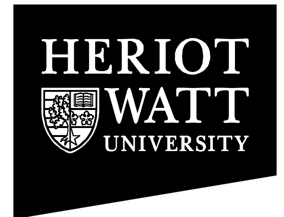

Name:	Rainer Johannes Beck		
School/PGI:	School of Engineering and Physical Sciences		
Version: *(i.e. First, Resubmission, Final)*	Final	Degree Sought:	Doctor of Philosophy

Declaration

In accordance with the appropriate regulations I hereby submit my thesis and I declare that:

1) the thesis embodies the results of my own work and has been composed by myself
2) where appropriate, I have made acknowledgement of the work of others and have made reference to work carried out in collaboration with other persons
3) the thesis is the correct version of the thesis for submission and is the same version as any electronic versions submitted*.
4) my thesis for the award referred to, deposited in the Heriot-Watt University Library, should be made available for loan or photocopying and be available via the Institutional Repository, subject to such conditions as the Librarian may require
5) I understand that as a student of the University I am required to abide by the Regulations of the University and to conform to its discipline.

* *Please note that it is the responsibility of the candidate to ensure that the correct version of the thesis is submitted.*

Signature of Candidate:		Date:	

Submission

Submitted By *(name in capitals)*:	
Signature of Individual Submitting:	
Date Submitted:	

For Completion in Academic Registry

Received in the Academic Registry by *(name in capitals)*:			
Method of Submission *(Handed in to Academic Registry; posted through internal/external mail)*:			
E-thesis Submitted			
Signature:		Date:	

Table of Contents

Abstract ii

Dedication iii

Acknowledgements iv

Table of Contents vi

Lists of Tables and Figures x

List of Publications xx

Chapter 1 - Introduction 1

1.1 Motivation 1

1.2 Summary of chapters 2

Chapter 2 - Background and literature review 4

2.1 Laser material processing 4

2.1.1 Pulsed lasers 4

2.1.2 Interaction of light and matter 5

2.1.3 Beam quality 6

2.2 Fundamentals of beam shaping 7

2.2.1 Reflective optics 8

2.2.2 Refractive optics 9

2.2.3 Diffractive optics 9

2.2.3.1 Iterative Fourier transform algorithm 11

2.3 Adaptive Optics 12

2.3.1 Wavefront sensors 15

2.3.1.1 Interferometric sensing 16

2.3.1.2 Hartmann- / Shack-Hartmann sensor 16

2.3.1.3 Pyramid wavefront sensor 17

2.3.2 Optimisation algorithms 17

2.3.2.1 Simulated annealing algorithm 18

2.3.2.2 Genetic algorithm 18

2.3.3 Deformable mirrors 19

2.3.3.1 Micromachined membrane deformable mirror (MMDM) 20

2.3.3.2 Piezoelectric deformable mirrors 20
2.3.3.3 Bimorph mirrors 21
2.3.3.4 Other types of deformable mirrors 22
2.3.3.5 Overview of applications 22
2.3.3.6 Application to intra-cavity laser beam shaping 23
2.3.3.7 Application to extra-cavity laser beam shaping 24
2.3.4 Liquid crystal spatial light modulators 27
2.3.4.1 Functionality 30
2.3.4.2 Phase response of liquid crystal layer 32
2.3.4.3 Applications to laser beam shaping 33
2.4 Summary 35

Chapter 3 - Experimental results using deformable mirrors 37
3.1 Devices 39
3.1.1 Piezoelectric deformable mirror (PDM) from OKO Technologies 39
3.1.2 Bimorph deformable mirror (BM) from BAE Systems 40
3.1.3 Comparison of response between a PDM and BM 42
3.1.3.1 Phase-stepping interferometry 43
3.2 Simulated annealing algorithm 47
3.3 Beam shaping capabilities of piezoelectric deformable mirror 51
3.3.1 Low power setup 51
3.3.2 Optimisations towards different beam shapes 53
3.4 Beam shaping capabilities of bimorph mirror 56
3.4.1 Setup 56
3.4.2 Optimisations towards different beam shapes 57
3.5 Application of piezoelectric deformable mirror to nanosecond laser machining. 60
3.5.1 Setup 60
3.5.2 Laser machining results 61
3.5.3 Conclusion 63
3.6 Application of piezoelectric deformable mirror to millisecond laser machining. 63
3.6.1 Setup 64

3.6.2 Beam shaping results 65
3.6.3 Laser machining results 67
3.6.4 Discussion and conclusion 69
3.7 Summary 71

Chapter 4 - Experimental results using spatial light modulators (SLM) 72
4.1 LC-R2500 from Holoeye 74
4.1.1 Device 74
4.1.2 Curvature of display and copper mount 75
4.1.3 Calibration of phase response 77
4.1.4 Laser machining setup 82
4.1.5 Damage tests 83
4.1.6 Example laser machining 86
4.1.7 Temporal fluctuations of phase modulation 90
4.1.8 Process synchronisation technique for flicker compensation 98
4.1.9 Speckle reduction technique 100
4.1.10 Laser machining on bulk material 106
4.1.11 Application of modified iterative Fourier transform algorithm (MIFTA) and closed loop feedback 109
4.1.12 Conclusion 113
4.2 X10468-04 from Hamamatsu 115
4.2.1 Device and setup 115
4.2.2 Analysis of temporal response 116
4.2.3 Process synchronisation for ‘on-the-fly’ changes of beam profiles 120
4.2.4 Conclusion 122
4.3 A512-0532 from Boulder Nonlinear Systems 123
4.3.1 Device and setup 123
4.3.2 Analysis of temporal response 125
4.3.3 Discussion 127
4.4 Summary and comparison of used SLM devices 128
4.4.1 Overview of specifications 128
4.4.2 Temporal response 128
4.4.3 Efficiency 130
4.4.4 Suitability for laser machining 132

Chapter 5 - Conclusions and future work 135
5.1 Conclusions 135
5.1.1 Deformable mirrors 136
5.1.2 Spatial light modulators 138
5.2 Future work 140
5.2.1 Affordable deformable mirrors with more actuators 140
5.2.1.1 Extension sensing 141
5.2.2 Spatial light modulators 142
5.2.2.1 Power handling capabilities 142
5.2.2.2 Temporal response 143
5.2.2.3 Devices for ultra-violet light 143

References 145

Lists of Tables and Figures

Tables

Table 3-1: Technical parameters of piezoelectric deformable mirror (PDM) and bimorph mirror (BM). 40
Table 3-2: Overview of beam diameters and resulting hole diameters for drilling with three pulses (average of 10 measurements) 69
Table 4-1: Comparison of SLM devices used in this work. 128
Table 4-2: Efficiency of used spatial light modulators. 132

Figures

Figure 2.1: Illustration of single element lens to focus a collimated laser beam. 7
Figure 2.2: Illustration of diffractive beam shaping using a computer generated hologram to generate a desired intensity distribution at the focal plane of a lens. 10
Figure 2.3: Schematic of iterative Fourier transform algorithm. 11
Figure 2.4: Schematic an Adaptive Optics system, consisting of wavefront modulator, wavefront sensor and control loop, for wavefront correction. 13
Figure 2.5: a) Principle of modulating a wavefront by means of a deformable mirror. The wavefront is altered by introducing a geometrical path difference to the deformable mirror. 14
Figure 2.6: Principle of modulating a wavefront using a liquid crystal spatial light modulator operating in reflection (mirror indicated by dashed box): a) The same grey value is addressed to the liquid crystal layer (blue box) and thus the refractive index and the resulting phase delay are constant across the device. b) Varying the grey values results in a refractive index change and consequently in a varying phase delay altering the wavefront 14
Figure 2.7: Schematic of micromachined membrane deformable mirror. 20
Figure 2.8: Simplified illustration of piezoelectric deformable mirror. 21
Figure 2.9: Simplified illustration of bimorph mirror. The different polarisation of the piezoelectric multilayer is indicated by "+" and "-". The red triangles indicate the lateral movement restrictions by the mirror mount. 22
Figure 2.10: Laser beam intensity profiles for beam shaping using deformable mirror and genetic algorithm (GA). The profile at bottom right represents the elite of the 99th generation of the GA. 25
Figure 2.11: a) Beam shaping result for doughnut profile using 19-element bimorph mirror; cross-sections of doughnut profile along horizontal (b) and vertical (c) axis. 26
Figure 2.12: Different phases and molecular arrangements of liquid crystal materials versus temperature 27
Figure 2.13: Change in the orientation of the liquid crystal molecules with increasing voltage U_{LC}: left for 90° twisted nematic liquid crystal cell and right for linear nematic liquid crystal cell. 29

Figure 2.14: Illustration of functionality of LC spatial light modulator. The incident plane wave is polarised along the x-axis. 30
Figure 2.15: Pulse-width-modulated signal for control of LC cell including inversion of pixel voltage and ITO voltage to prevent deterioration of LC layer. 31
Figure 2.16: Beam steering efficiency of liquid crystal device versus angle limited by fringing field effects. 34
Figure 2.17: a) Beam shaping results of femtosecond laser source imaged in the focal plane; b) corresponding fs laser marking results on stainless steel. 35
Figure 2.18: Direct femtosecond laser micro-structuring of stainless steel with user-defined focal spot shapes: a) circular top-hat, b) square top-hat, c) doughnut profile. 35

Figure 3.1: a) and b) piezoelectric deformable mirror (PDM) with housing partially removed; 39
Figure 3.2: a) Bimorph mirror (BM); b) electrode pattern of BM. 40
Figure 3.3: Illustration of bimorph mirror consisting of multilayer of piezo-ceramics with opposite polarisation directions (indicated by “+” and “-“). The red triangles indicate the lateral movement restrictions by the mirror mount. 41
Figure 3.4: Surface profiles of deformable mirror surface (left part) with illustration of applied actuator voltage for PDM (a, b and c) and BM (d, e and f) determined based on phase-stepping interferometry: a) voltage set applied just to flatten PDM; b) 100 V added to three individual actuators of PDM resulting in local deformation; c) difference between a and b; d) no voltage applied to BM; e) 100 V added to three individual actuators of BM resulting in global deformation; f) difference between d and e. 43
Figure 3.5: Demonstration of wrapped and unwrapped phase profile for a tilted mirrored surface. 45
Figure 3.6: Phase unwrapping technique. 45
Figure 3.7: Setup for phase-stepping interferometry. The dashed grey line indicates additional components and laser source required for the measurements with the SLM (see section 4.1.2 and 4.1.3). 46
Figure 3.8: Schematic representation of simulated annealing algorithm for beam shaping with deformable mirror. 49
Figure 3.9: Setup for closed-loop beam shaping experiments using PDM and low power Nd:YAG laser source. Lens 1: 4x microscope objective, f=18.5 mm; Lens 2:

f=350 mm, Ø=50.8 mm; Lens 3: f=400 mm, Ø=50.8 mm; Lens 4: f=80 mm, Ø=25.4 mm; Lens 5: f=1000 mm, Ø=25.4 mm. 52
Figure 3.10: Surface profile of PDM when 147 V applied to all actuators; b) resulting beam shape at focus of the setup shown in Figure 3.9 (1 pixel = 5.6 μm)... 53
Figure 3.11: Beam shaping results using PDM: a) beam profile for flat reference mirror (1 pixel = 5.6 μm); b) target profile for doughnut shape; c) beam shaping result for doughnut shape after 1000 iterations; d) development of root mean square error throughout iterations. 54
Figure 3.12: Top row: Beam profile with flat reference mirror; below: Use of PDM as variable homogeniser with different circular flat top target profiles (left), the beam shaping result after 2000 iterations of SA (middle) and the cross-sections along the horizontal and vertical direction (right). 1 pixel = 5.6 μm. 55
Figure 3.13: Beam shaping using PDM and SA: a) square flat top target profile; b) beam shaping result after 2000 iterations (1 pixel = 5.6 μm). 56
Figure 3.14: Target profiles (top row) and beam shaping results (bottom row) using bimorph mirror and SA to generate elliptical beam shapes at an angle of 0°, 45°, 60° and 90° (1 pixel = 7.4 μm). 57
Figure 3.15: Root mean square error for beam shaping result shown in Figure 3.14 e). 58
Figure 3.16: a) beam shape for flat reference mirror; b) square flat top target profile; c) beam shaping result after 5000 iterations using BM and SA; d) cross-sections along horizontal and vertical direction of beam shaping result and of target profile (1 pixel = 7.4 μm). 59
Figure 3.17: Setup for nanosecond laser machining experiments (Lens 1: f_1=400 mm, diameter (Ø)=50.8 mm, Lens 1: f_2=150 mm, Ø =25.4 mm, Lens 3: f_3=125.1 mm, Ø =127 mm, Lens 4: f=30 mm, Ø=25.4 mm, and Lens 5: f=500 mm, Ø=25.4 mm). 61
Figure 3.18: a) Beam profile at focus when using an optically flat reference mirror instead of the PDM (1 pixel = 7.4 μm); b) target profile for the optimisation; c) beam shaping result at focus with PDM after 2000 iterations of SA....... 62
Figure 3.19: Laser marking result on stainless steel operating the laser at a repetition rate of 100 kHz and an average power of 20W whilst scanning the beam from left to right at a speed of 2500 mm/s: a) using optically flat reference mirror; b) using PDM to create the flat top beam shape as shown in Figure 3.18 c). 62

Figure 3.20: Experimental setup of PDM embedded into ms laser machining workstation. Machining lens: f=120 mm, diameter=20 mm, Focusing lens: f=1000 mm, diameter=25.4 mm...65
Figure 3.21: Initial beam profile of millisecond (ms) laser using flat reference mirror (1 pixel = 7.4 µm)...65
Figure 3.22: Beam shaping towards circular flat top profile: a) target profile with 100 pixels diameter; b) beam shaping result after 2500 iterations (1 pixel = 7.4 µm)...66
Figure 3.23: Beam shaping towards doughnut profile: a) target profile; b) beam shaping result after 2500 iterations (1 pixel = 7.4 µm). 66
Figure 3.24: Cross section of holes drilled with a single laser pulse into 3 mm thick steel with a) unmodified, b) circular flat top and c) doughnut beam profile........68
Figure 3.25: Cross section of holes with three pulses into 3 mm thick steel with a) unmodified, b) circular flat top and c) doughnut beam profile...................69

Figure 4.1: Control unit and display of SLM LC-R 2500 from Holoeye 74
Figure 4.2: SLM display attached to copper mount with optional water cooling...........75
Figure 4.3: Curvature of SLM display: a) initially; b) after mounting onto copper mount; both height profiles determined experimentally using 5-step phase-stepping interferometry (small phase noise can result in vertical lines due to spatial phase unwrapping)..76
Figure 4.4: Setup for phase calibration of SLM based on Michelson interferometer.....78
Figure 4.5: Alignment of polarisation direction relative to SLM display (front view)...78
Figure 4.6: Image addressed to SLM divided in sectors with reference grey value (Ref) and varying grey value (Var); resulting interference pattern measured with CCD camera and vertical cross sections (along red and blue line as indicated on interference pattern). 79
Figure 4.7: Phase response for linear look-up table...80
Figure 4.8: Look-up table (LUT) for calibration after mounting display onto copper mount...81
Figure 4.9: Phase response after calibration. 81
Figure 4.10: a) Phase response after calibration for different interfaces as indicated on b) example phase map addressed to SLM. 82
Figure 4.11: Setup for nanosecond (ns) laser machining experiments. Details of the setup are given in the text above. 83

Figure 4.13: a) temporal variation of intensity distribution in zero order (black line) and the first diffraction orders (blue and red line) with 14.7W average power being incident on the SLM display (~65ns pulse length; 30kHz repetition rate); b) intensity in the first diffraction orders divided by intensity of zero order. 85
Figure 4.12: Schematic of phase profile of binary grating addressed to SLM and resulting diffraction spots. 85
Figure 4.14: a) intensity distribution of target profile for IFTA; b) phase distribution of resulting kinoform; c) phase map with tiled kinoforms in 3x4 pattern for addressing to SLM. Boundaries between kinoforms are indicated with red dashed lines. 87
Figure 4.15: Example of laser machining using SLM as DOE: a) laser ablation of metal from a metal coated glass slide using single diffraction pattern addressed to SLM based on Inverse Fourier Transform Algorithm (IFTA); b) laser ablation of polymer (purple) from a polymer coated metal using a sequence of six individual IFTA generated kinoforms. Local positioning is achieved by the kinoform addressed to the SLM rather than a mechanical motion system. The ablated area at the bottom right of a) and the centre of the middle square are due to the inherent zero order beam. 88
Figure 4.16: Setup for laser machining experiments with SLM used for beam shaping and steering. 89
Figure 4.17: Schematic of beam steering: a) initial phase map to generate beam shape for marking sqaure shape in top middle in Figure 4.15 b); b) wrapped phase gradient, c) resulting phase profile when combining a) and b) with periodic boundary conditions to generate beam shape for top left mark in Figure 4.15 b). 89
Figure 4.18: Fluctuations of intensities of zero and first diffraction orders due to flickering of the SLM (temperature of display 24°C). 91
Figure 4.19: Fluctuations of the first diffraction order when addressing binary gratings with grey levels (255/192), (255/128) and (255/192) constantly to the SLM. The period of the flickering is ~13.3 ms in all cases, though the individual course of the flickering severely depends on the grey values. 92
Figure 4.20: Fluctuations of the first diffraction order when addressing binary gratings with grey levels (0/64), (0/128) and (0/192) constantly to the SLM. The

period of the flickering is ~13.3 ms in all cases, though the individual course of the fluctuations severely depends on the grey values. 93
Figure 4.21: a) Example beam shape of "smiley face" with zero order beam blocked off; b) Temporal course of average intensity of smiley face. The period of the flickering is ~13.3 ms. 94
Figure 4.22: a) Laser machining using scan head (scanning direction left to right, speed 12.5mm/s) of metal coated glass slide with binary grating addressed to SLM; b) modelled machining results based on intensity data shown in Figure 4.18. 95
Figure 4.23: Temperature dependence of flickering for zero and first diffraction order intensities: maximum and minimum intensity values for flickering (top section); difference between maximum and minimum values (bottom section). 96
Figure 4.24: Average intensities of zero order and first diffraction orders when addressing two similar but shifted binary gratings with phase difference of π alternating to SLM with a delay of 100 ms. 98
Figure 4.25: Machining result after scanning a laser beam modulated by a constant binary grating at a speed of 40 mm/s across stainless steel: a) without and b) with flickering compensation using process synchronization. 99
Figure 4.26: Demonstration of periodic shift of hologram respectively kinoform in horizontal and vertical direction with increments m of a quarter of the size of the initial kinoform. The red circle tracks a single feature. 101
Figure 4.27: Images of holograms formed at the end of a 6-f optical system taken using a CCD camera: A) Result for the original calculated kinoform (without application of speckle reduction technique), B) 16 images taken for randomly shifted kinoforms, combined and normalised in software, C) 16 images taken for periodically shifted kinoforms, combined and normalised in software. 102
Figure 4.28: Plot of normalised intensity values taken from each image shown in Figure 4.27. Plots are also shown for the ideal case and for the case where the image is still pixelated but each pixel is of uniform intensity. 103
Figure 4.29: A) Star pattern used to derive kinoform for hologram. B) Star pattern marked on thin layer of aluminium coated on glass. A kinoform was marked 9 times with 100 ms exposure. 104

Figure 4.30: Marks on a thin layer of aluminium coated on glass created using an SLM to produce an off-axis image: A) Single kinoform marked 16 times with 200ms exposure; B) 16 randomly shifted kinoforms marked for 200 ms each; C) 16 periodically shifted kinoform marked for 200 ms each. 105
Figure 4.31: a) Data matrix pattern representing character "A" marked on thin layer of aluminium coated on glass. 16 periodically shifted kinoforms were marked for 10 ms each. b) Data matrix marked in photo-resist using 16 periodically shifted kinoforms marked for 300 ms each. The stainless steel substrate is untouched by the machining process. 106
Figure 4.32: Data matrix representing the letters "AOP" marked on stainless steel. A) Using a 50 mm single element lens and 16 periodically shifted kinoforms marked for 100ms each. B) Using a 30 mm doublet lens four overlapping patterns are marked using a total of 36 periodically shifted kinoforms each marked for 1.7 ms. C) The four separate patterns used to build up the mark shown in B. 108
Figure 4.33: Illustration of the MIFTA principle: a) Far-field intensity distribution of previous iteration; b) modified constraint; c) desired output. It can be seen that the modified constraint is a mirror image of the output from the previous iteration about the desired output. 110
Figure 4.34: Setup of SLM embedded into laser machining workstation including CCD camera for adaptive feedback. 111
Figure 4.35: Top row: Intensity distribution measured with CCD camera: a) initial kinoform; b) software calculated average of 16 images taken for periodically shifted kinoform; c) calculated average of 16 images taken for periodically shifted kinoform based on MIFTA and feedback loop; Bottom row: Laser marks on thin metal layer coated on glass: d) single kinoform machined 16 times with 13.3 ms exposure time; e) IFTA generated kinoform shifted periodically 16 times and marked for 13.3 ms each; f) kinoform based on MIFTA and feedback loop, shifted periodically 16 times and marked for 13.3 ms each. The slight colour change in the upper one third of the images is due to using two tiled images because of the limited viewing area of the microscope. 112
Figure 4.36: LCoS SLM X10468-04 from Hamamatsu: Controller unit and display head. 115

Figure 4.37: Temporal course of intensities of first diffraction orders for binary grating being addressed constantly to SLM. 117
Figure 4.38: Top: driving voltage for liquid crystal layer using analogue driving at refresh rate of 480 Hz and alternating refresh rate of 240 Hz; bottom: Resulting response of phase modulation. 117
Figure 4.39: a) example intensity distribution as measured with high speed camera; b) temporal course of average intensity of "smiley face" as shown in part a). 118
Figure 4.40: a) Average intensities of first diffraction order when addressing two similar but shifted binary gratings with phase difference of π rad alternating to SLM with a delay of 50 ms; b) zoom of response during the change. 119
Figure 4.41: Average intensities of first diffraction order when alternating two shifted binary gratings with a phase difference of π rad on a single-frame basis. . 120
Figure 4.42: Periodic variations of intensities of zero and first diffraction orders when alternating on a single-frame basis between two similar binary gratings addressed to the SLM. The intensities of the first diffraction orders are almost identical. 121
Figure 4.43: a) Machining result when alternating two binary gratings with different periodicities on the SLM on a single-frame basis while scanning the laser beam at a speed of 25 mm/s across stainless steel (scanning direction from left to right); b) schematic for process synchronization technique indicating when process is ‘on’ and ‘off’. 121
Figure 4.44: Machining results with settings as described in Figure 4.43 but utilising the process synchronization technique to remove deep and blackened marks from zero order. 122
Figure 4.45: Display of SLM A512-0532 from Boulder Nonlinear Systems. 123
Figure 4.46: Schematic of cross section of XY Nematic Series of BNS: Planar high efficiency mirror and smoothing of the electric field eliminate most of the grating effects associated with pixelated SLMs. 124
Figure 4.47: Average intensities of first diffraction orders for binary grating with phase difference of π addressed constantly to BNS SLM. The average intensity of the zero order is not shown to increase the visibility of the fluctuations of the first diffraction orders. 125

Figure 4.48: Average intensities of first diffraction orders when addressing the SLM with two alternating, similar but phase shifted (by π rad) binary gratings with a delay time of 20 ms. 126
Figure 4.49: Average intensities of first diffraction orders when addressing two similar but shifted binary gratings with phase difference of π alternating to SLM on single frame basis. 127
Figure 4.50: Comparison of response when alternating between similar, but shifted binary gratings with a phase difference of π rad on the SLMs. The average intensities of the first diffraction orders are displayed normalised, but with additional offset. 129

List of Publications

Journal publications:

1) R. J. Beck, J. P. Parry, J. D. Shephard, and D. P. Hand: “Compensation for time fluctuations of phase modulation in a liquid-crystal-on-silicon display by process synchronization in laser materials processing”, Applied Optics 50(18), 2899–2905 (2011).
2) J. P. Parry, R. J. Beck, J. D. Shephard, and D. P. Hand: “Application of a liquid crystal spatial light modulator to laser marking”, Applied Optics 50(12), 1779-1785 (2011).
3) R. J. Beck, J. P. Parry, W. N. MacPherson, A. Waddie, N. J. Weston, J. D. Shephard, and D. P. Hand: "Application of cooled spatial light modulator for high power nanosecond laser micromachining", Optics Express 18, 17059-17065 (2010).

Conference publications:

4) R. J. Beck, A. J. Waddie, J. P. Parry, J. D. Shephard, M. R. Taghizadeh, and D. P. Hand: “Adaptive laser beam shaping for laser marking using spatial light modulator and modified iterative Fourier transform algorithm“, in Proc. LiM2011, Munich, Germany (2011).
5) R. J. Beck, J. P. Parry, J. D. Shephard, and D. P. Hand: “Adaptive extracavity beam shaping for application in nanosecond laser micromachining”, SPIE paper 7913-12, in Proceedings of Photonics West, San Francisco, United States (2011).
6) J. P. Parry, R. J. Beck, N. Weston, J. D. Shephard, and D. P. Hand: “Application of Adaptive Optics to laser micromachining”, in Proc. ICALEO2010, Anaheim, California, United States (2010).
7) R. J. Beck, J. P. Parry, A. Waddie, W. N. MacPherson, N. Weston, J. D. Shephard, and D. P. Hand: “Application of spatial light modulator for beam shaping in nanosecond laser machining”, in Proc. LPM2010, Stuttgart, Germany (2010).
8) D. P. Hand, J. P. Parry, R. J. Beck, R. Carrington, A. Waddie, N. J. Weston, and J. D. Shephard: “Application of adaptive optics to nanosecond pulsed laser micro-machining”, Invited Presentation, in Proc. PICALO2010, Wuhan, China (2010).
9) R. J. Beck, R. Carrington, J. P. Parry, W. N. MacPherson, A. Waddie, D. T. Reid, N. J. Weston, J. D. Shephard, and D. P. Hand: “Adaptive optics for optimization of laser processing", in Proceedings of LAMP09 , Kobe, Japan (2009).

Conference presentations:

10) R.J. Beck, J. P. Parry, W. N. MacPherson, A. J. Waddie, N. Weston, J. D. Shephard, and D. P. Hand: "Piezoelectric actuated deformable mirrors for application in laser micromachining", IWPMA, Antalya, Turkey (2010).
11) J. P. Parry, R. J. Beck, N. Weston, J. D. Shephard, and D. P. Hand: "Application of a spatial light modulator to laser machining in the nanosecond regime", Photon 10, Southampton, United Kingdom (2010).
12) D. P. Hand, R. J. Beck, J. P. Parry, R. Carrington, W. M. MacPherson, A. J. Waddie, D. Reid, N. Weston, and J. D. Shephard: "Adaptive optics for laser-based manufacturing processes", Invited Presentation, Laser Application of Adaptive Optics Workshop, UK Astronomy Technology Centre, Edinburgh, United Kingdom (2009).
13) R. J. Beck, J. D. Shephard, E. Ramsay, D. Reid, and D. P. Hand: "Adaptive optics for optimization of laser processing", Photon 08, Edinburgh, United Kingdom (2008).

Other publications:

14) J. P. Parry, R. J. Beck, J. D. Shephard, and D. P. Hand: "Adaptive optics enter materials-processing arena", Laser Focus World, Volume 46, Issue 12 (2010).
15) J. P. Parry, R. J. Beck, J. D. Shephard, and D. P. Hand: "Dynamic beam shaping for laser material processing", The Laser User Magazine, Issue 060, Autumn (2010).

Chapter 1

Introduction

This PhD project was concerned with the application of adaptive optics (AO) for beam shaping for the application to laser materials processing. Two different types of beam shaping devices, i.e. deformable mirrors and liquid crystal spatial light modulators, were investigated. The majority of the work has been carried out with a nanosecond laser machining workstation although millisecond laser pulses were also used, dependent on the particular application.

1.1 Motivation

The Gaussian beam shape typically generated from a high beam quality laser is not always ideal for an intended application or task; instead alternative intensity distributions such as flat tops (circular or square), or doughnut shapes can in some cases be more suitable for the application and result in better machining results or more economical use of the available laser power. Laser beams with sharply defined edges, for example, are more suitable for drilling applications [1], whilst elliptically-shaped laser beams are known to be beneficial for cutting and dicing applications [2, 3]. Creating an elliptically-shaped beam along the cutting direction can improve the ablation efficiency and can also increase the cutting speed. Other, more complex intensity distributions might be beneficial for surface micro structuring.

Using diffractive optical elements or refractive optics a huge variety of different beam profiles can be generated [4, 5, 6], yet each different output shape requires a new and distinct optical element and minor changes in the input beam profile can completely change the resultant output beam profile rendering a bespoke optical element useless. Adaptive optics (AO), however, have the distinct advantage of enabling the user to dynamically change between a wide range of laser beam profiles. This means that the beam shape could be altered 'on-the-fly', i.e. during the actual machining process, by means of AO. Originally, AO techniques based on deformable mirrors were mainly developed and applied in astronomy and the military. More recently, comparatively low-cost but nevertheless powerful and robust deformable mirrors have become

available and as a result AO have started to play a substantial role in research, industry and medicine.

The aim of this PhD project was to investigate the application of AO devices to laser machining. Two different types of wavefront modulating optics, namely deformable mirrors (DM) and spatial light modulators (SLM), were used in the work presented here: DM have a fast response and exhibit the ability to withstand very high laser powers, though in most cases have only a comparatively small number of active elements. Liquid crystal spatial light modulators (SLM) on the other hand, have a very high spatial resolution with the drawback of a slower response and severe limitations in terms of their power handling capabilities which is of overriding importance in laser-based machining applications. In laser-based manufacturing processes, DM have been mainly applied for controlling fundamental laser beam parameters such as the focus position [7, 8] and have been used to a much more limited extend in the modification of the spatial intensity distribution for laser machining. The application of SLMs to laser materials processing is limited by their comparatively low damage threshold for optical radiation. As a result, research into SLMs for micromachining has been limited to femtosecond [9, 10] and picosecond [11] laser pulses. However, in industry, nanosecond pulsed laser machining is much more common. The investigation of the applicability of AO to nanosecond pulsed lasers is the driver for the work presented in this thesis, especially if AO techniques are to be considered for the development of practical laser machining applications.

1.2 Summary of chapters

This thesis is divided into five chapters as detailed below:

- ***<u>Chapter 1: Introduction</u>***

This chapter.

- ***Chapter 2: Background and Literature Review***

Chapter 2 provides background knowledge and information on the methods, techniques, algorithms and devices used for this research project. A comprehensive literature review, presenting the state of the art and prior knowledge forms the core of this chapter. The fundamentals of laser materials processing and beam shaping are described. Adaptive optics including the beam shaping devices and applications are reviewed.

- ***Chapter 3: Experimental results using deformable mirrors***

This chapter describes the application of deformable mirrors to beam shaping for application in laser material processing. The beam shaping capabilities of a piezoelectric deformable mirror (PDM) and a bimorph mirror (BM) are assessed. The PDM is applied to modify the high beam quality of a nanosecond laser used for surface marking. In addition, the device was utilised to improve the drilling of through holes with a millisecond system having a multimode laser beam.

- ***Chapter 4: Experimental results using spatial light modulators***

Three different spatial light modulators (SLM) based on liquid crystal displays are applied to beam shaping of a nanosecond pulsed laser. Limitations due to the power handling and the optical addressing are discussed and methods to overcome these are presented. Complex beam shapes can be generated with sufficient intensity for direct laser marking. Utilizing the dynamic nature of the SLMs including adaptive feedback enables to significantly improve the quality of the laser marking that can be achieved.

- ***Chapter 5: Conclusions and future work***

Chapter 5 summarizes the major results and overall conclusions on the application of adaptive optics to beam shaping in laser materials processing. Benefits and limitations of the devices used, and techniques developed, are discussed. Finally, future work suggestions are proposed, some of which are being investigated in a follow-on project.

Chapter 2

Background and literature review

It can be argued that the laser is one of the most important discoveries in the past century and the laser is ubiquitous in every day life. In the context of this thesis, I will focus on the use of lasers in manufacturing in particular and research to a lesser extent. Lasers are used extensively in laser processing of a vast range of materials and on greatly varying scales [12, 13]. The laser material interaction and the processes taking place depend heavily on the energy distribution, i.e. the beam shape, of the laser beam in the interaction zone. By controlling and adapting the beam shape, the processes can be modified and optimised to provide a required outcome. Adaptive optics (AO) are a flexible and adaptable technique which can provide such control over the intensity distribution of the laser beam. In the research presented and described in this thesis, Adaptive Optics have been used to modify beams of laser systems used in pulsed laser materials processing. This chapter presents background information on the fundamental technology, techniques and various implementation of AO and a review of the current state of the art as presented in the open literature.

2.1 Laser material processing

2.1.1 Pulsed lasers

Lasers can produce either a continuous wave (cw) output beam or laser pulses. Pulsed lasers are preferable for processes for which it is important to locally confine the deposition of energy to a work piece. Pulse lengths can range from milliseconds to attoseconds; in practice pulses in the range of milliseconds to femtoseconds are used for materials processing. There is a broad range of techniques available to the laser designer to achieve a pulsed output, such as pulsed pumping, Q-switching and mode-locking (see [13] for further details). These techniques can be used to control the energy storage within the laser cavity and its release in form of laser pulses with certain pulse durations, pulse energies, peak intensities and repetition rates.

When applying a pulsed laser to laser-based manufacturing applications the pulse characteristics have a strong impact on the process. The pulse duration, in conjunction

with the peak intensity, is particularly important for the type of interaction between the laser light and the material and thus industrial laser machining systems are typically referred to as milli-, micro-, nano-, pico- or femtosecond systems.

2.1.2 Interaction of light and matter

For the experimental results described in this thesis mainly a nanosecond (ns) laser machining workstation, but also a millisecond (ms) system was used, and the characteristic light matter interactions for these regimes are summarised in the this section. An in depth explanation of these processes can be found in [12, 13, 14].

The interaction between laser light and matter depends on the characteristics of the laser, such as wavelength, intensity, angle of incidence and illumination time, and on the physical and chemical properties of the material. For laser light incident on a material, part of the light is reflected and part is absorbed with the absorption being strongly dependent on the material and the wavelength used. The laser radiation absorbed by a material typically results in excited free electrons for a metal, in lattice vibrations for an insulator and in both excited electrons and vibrations for a semiconductor [14]. The absorbed energy of the laser is dissipated as heat. For low laser intensities, the laser beam simply acts as a heat source and results in an increased temperature of the surface and the bulk of the material depending on its thermal conductivity. For increased laser intensities, the temperature can increase and give rise to phase transitions such as melting or vaporisation.

The most common laser based manufacturing processes, such as drilling, cutting or surface structuring, utilizes ablative techniques. In these cases, a material removal occurs in form of a liquid, vapour or plasma. Yet, for the removal of molten material an additional gas jet is required.

The spread of heat varies significantly for different materials. For metals, electron-electron relaxation occurring over a timescale of 10^{-12} – 10^{-14} s and electron-phonon relaxation occurring over a timescale of 10^{-10} – 10^{-12} s are the main heat and energy transfer processes within the material. In comparison, non-metals typically exhibit a significantly reduced thermal conductivity and the relaxations occur over a timescale of 10^{-6} – 10^{-12} s [14]. As a consequence, for laser materials processing using high power

ms laser pulses, being orders of magnitude longer than these relaxation times for the heat transfer within the work piece, the absorbed laser irradiation is spread to a significantly larger area compared to the laser spot size. For ms laser machining melting is the predominant phase transition and the molten material is typically removed by means of a gas jet. For nanosecond and especially picoseconds laser machining, the pulse durations are similar to the relaxation times for the heat transfer. This results in better confined heat and hence a direct vaporization can occur in addition to melting. For high laser powers and intensities, the laser induces a vapour and plasma plume and the interactions between the laser irradiation and this plume have a severe impact on the process. For further information please see references [12, 13, 14, 15].

2.1.3 Beam quality

For laser-based machining applications, a sufficiently high laser intensity at the work piece is essential. In the context of the work presented in this thesis, the laser beam is typically focussed to a small spot. The ability to focus a laser beam can be quantitatively described by the beam quality product M^2. This parameter relates the dimensions of the focussed laser spot compared to a diffraction limited focussed spot based on the fundamental Gaussian beam (TEM_{00}) according to Equation 2-1.

$$M^2 = \frac{\omega_{0(real)} \cdot \theta_{(real)}}{\omega_{0(Gaussian)} \cdot \theta_{(Gaussian)}};$$ Equation 2-1

Where $\omega_{0(real)}$ and $\omega_{0(Gaussian)}$ are the radius of the beam waist of the real laser beam and the ideal Gaussian beam respectively. The angle θ describes the half angle of the divergence of the real beam and of the ideal Gaussian beam. The ideal Gaussian beam has an M^2 value of 1, but real lasers have a value greater than this and contain a certain amount of higher order modes in the output beam.

The radius of the beam waist of the focussed spot can be calculated using Equation 2-2 and considering, the beam quality factor M^2, the focal length f of the lens, the wavelength λ and the beam waist ω_0 of the collimated beam (see illustration in Figure 2.1).

$$\omega_{spot} = \frac{M^2 \cdot f \cdot \lambda}{\pi \cdot \omega_0};$$ Equation 2-2

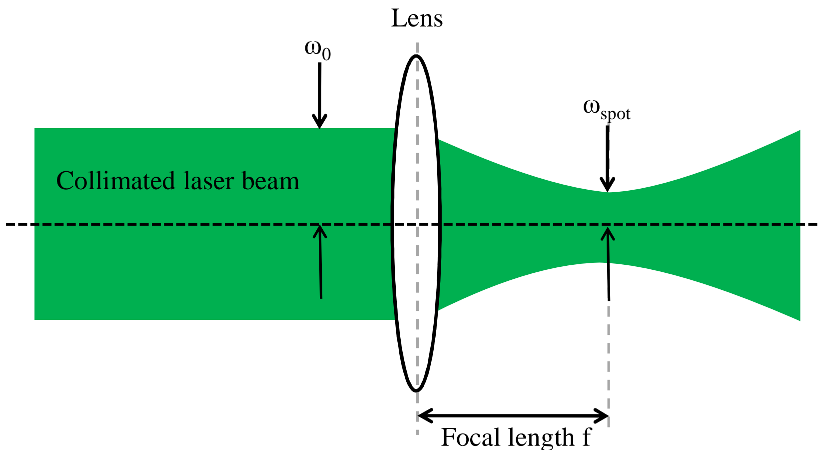

Figure 2.1: Illustration of single element lens to focus a collimated laser beam.

The beam quality product of a laser can be determined for example using a knife-edge technique [16]. For the work presented in Chapters 3 and 4, a semi-automated beam profiling software was used to measure the M^2-values [17].

2.2 Fundamentals of beam shaping

In many laser applications some form of beam shaping is beneficial to the manufacturing or machining process taking place in the laser material interaction zone. Beam shaping controls the energy distribution across a beam and can also be used to reconfigure a typically circular beam outline to an outline shape optimised for a particular task. Many lasers emit a beam with a more or less Gaussian intensity distribution. Lasers with a small M^2 value typically emit near perfect Gaussian beams.

For many laser applications some form of beam shaping is used to modify or redistribute the typically Gaussian intensity distribution coming from the laser towards a beam shape that is more suitable for the task. The simplest and widely used approach to achieve a different beam shape is to expand the beam and then to use a mask in order to laser mark only a specific areas [18]. For example, masking is the most common beam shaping approach in laser lithography. Spatially graded absorbers or reflectors can be used e.g. to generate a flat top profile, i.e. a uniform intensity distribution, from a Gaussian beam shape. Such masks however typically result in significant loss of laser

radiation and hence are less appropriate for application to high power laser materials processing.

Since a laser typically emits coherent radiation in a narrow spectral profile with a planar wavefront, alternative phase and wavefront control mechanisms can be used to generate a redistribution of the irradiance of the laser. A significant benefit of such an approach is that they are near lossless.

For example, the laser beam can be altered by means of an arbitrary shaped continuous mirror to introduce a change of the geometrical path lengths and also by a segmented or pixelated reflective surface in a diffractive optics approach (see section 2.2.3). Furthermore, transparent materials can be applied with continuous or segmented surfaces to introduce an optical path difference. Generating a collimated flat top beam profile for example by means of reflective optics, i.e. typically aspheric mirrors, can be beneficial for interferometric applications [19]. A flat top intensity distribution at focus, generated by means of refractive optics, can also be beneficial for drilling applications [20, 21]. A diffractive optics approach enables the generation of much more complex intensity distributions for direct laser marking [22] or of multiple laser spots for parallel processing [23] and optical tweezers [24]. Reflective, refractive and diffractive beam shaping are described in more detail in the following three sub-sections:

2.2.1 Reflective optics

Shaped reflective surfaces can be used to modify the intensity distribution of a laser. A ‘simple’ curved mirror surface with a spherical, parabolic or toroidal profile for example leads to a focussing effect of the incident beam. More complex shaped and not necessarily rotationally symmetric mirrors can be used for a further redistribution of the irradiance. The design of the beam shaping setup, typically consisting of two mirrors, can be determined based on geometrical optics [25]. For this, the two basic conditions that the optical path lengths for all rays must be the same and the conservation of the total energy through the system must be considered. Reflective beam shaping elements typically can withstand much higher laser powers compared to beam shaping elements working in transmission and are thus particularly suitable for very high power laser applications.

2.2.2 Refractive optics

When entering a transparent medium with a different refractive index at an angle, the wavefront changes its direction according Snell's Law which is the fundamental principle of refractive optics. Although refractive optics are the underlying concept in the vast majority of focussing or imaging optics, they are mostly based on rotationally symmetric elements with spherical or near spherical surfaces. However, refractive beam shaping optics are typically based on non-spherical and freeform optics. Their smooth and continuous surface shape can be determined analytically based on geometrical optics and the principle of conversion of energy [5, 6, 26]. A single refractive surface enables the generation of a desired intensity distribution in a particular target plane. A second beam shaping optic, e.g. another refractive element, is required to control the phase distribution and hence the propagation of the wavefront beyond this target plane [5]. The advantage of refractive beam shaping optics is their typically high efficiency and also that they can be used over an exceptionally wide range of wavelengths [6]. However, standard manufacturing process by wafer based elements or moulds for embossing in glass imply limitations on the fine scale of the surfaces and hence limit the complexity of the intensity distributions that can be generated [6]. Also, materials which are best for moulding are not necessarily best for high power laser transmission.

2.2.3 Diffractive optics

An alternative way to control and modify a wavefront is by means of diffraction rather than refraction. The properties and designs of so-called diffractive optical elements (DOEs) are typically much more complicated than those for refractive optics. While reflective and refractive optics can be generally treated with geometric ray tracing methods, diffractive optics operate in the Fourier domain and hence require computer-based algorithms to calculate transfer functions of a diffractive optical system.

DOEs can be used in a holographic approach considering the inherent Fourier transform in the far field of the hologram for coherent illumination. An illustration of such an approach to modify, for example, an incident Gaussian intensity distribution towards a custom target distribution at the focal plane of a lens is shown Figure 2.2. Various algorithms exist to transform a known incident spatial intensity distribution towards a desired, custom output profile, i.e. image, in the far field based on a phase-only

hologram [27, 28, 29, 30]. The Gerchberg-Saxton algorithm (GS) [27] or the iterative Fourier transform algorithm (IFTA) [28] enable the retrieval of the required phase profile in the plane of the DOE which yields the desired intensity distribution in the target plane in the far field. The IFTA is described in more detail in the next section. Such a phase profile, also referred to as computed generated hologram or kinoform, can be imprinted into a transmissive or reflective phase plate with discrete thickness or height steps respectively, to create phase differences in the output beam. Such devices are for example widely used in the creation of symbols, shapes or simple graphical elements in conjunction with simple laser pointers or other coherent sources. Precision elements manufactured in materials such as fused silica can be used in high power laser processes. These elements are typically produced by an etching process and prices are in the order of £5k [31]. The disadvantage is that they are static and even a minor modification requires a complete change of the fundamental design creating significant cost.

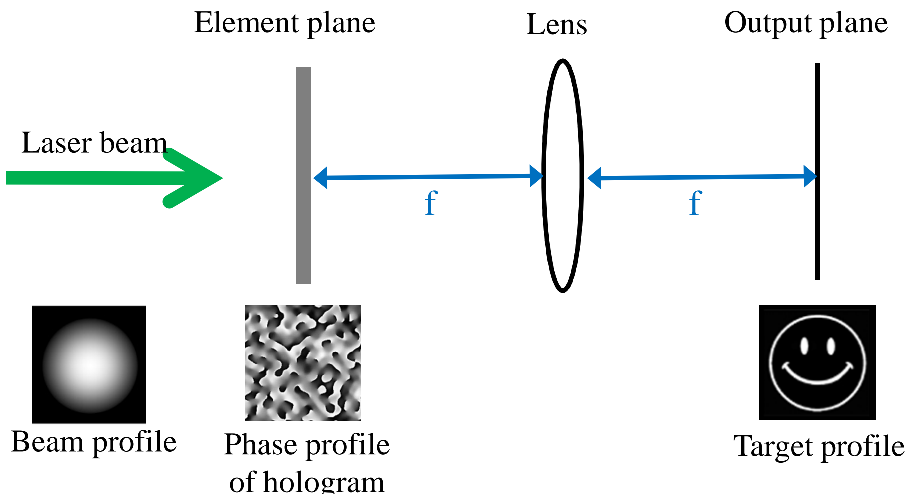

Figure 2.2: Illustration of diffractive beam shaping using a computer generated hologram to generate a desired intensity distribution at the focal plane of a lens.

Alternatively, and much more flexible, is the approach to use a liquid crystal spatial light modulator (SLM, see description in section 2.3.4). In a SLM, each pixel of the device can produce a variable and controlled phase delay and hence the SLM can be utilized as variable diffractive optical element.

2.2.3.1 *Iterative Fourier transform algorithm*

The iterative Fourier transform algorithm (IFTA) enables the design of diffractive optical elements which transform a known initial spatial intensity distribution towards a custom target profile. Characteristic of this approach is the propagation back and forth between the spatial and the frequency domain by means of a Fourier transform for each iteration, giving the name for this approach. A review of the different types, approaches and developments of the IFTA in the context of laser beam shaping can be found in [30].

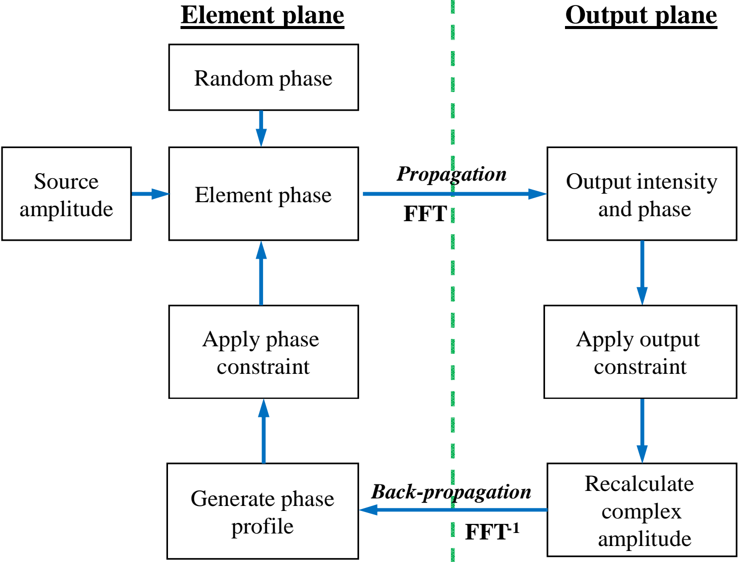

Figure 2.3: Schematic of iterative Fourier transform algorithm.

A schematic of the IFTA is shown in Figure 2.3. The algorithm utilizes a fast Fourier transform (FFT) and the inverse FFT (FFT^{-1}) to propagate back and forth between the element plane and the object plane. In order to achieve a convergence of the algorithm and accordingly the beam shape towards the target profile, constraints need to be imposed in both the element and output plane. The phase constraints are for example the quantised phase levels and the pixelated lateral structure of the diffractive optical elements. The output constraint is the actual target profile. The approach by which these constraints are imposed has a critical impact on the ability of the IFTA to converge to an ideal solution [32]. An iterative quantisation is applied for the phase constraints in the element plane and the direct quantisation is only applied during the final iterations. This feature is added to overcome the stagnation problem of the Gerchberg-Saxton algorithm and is thoroughly described in [28, 33, 34].

2.3 Adaptive Optics

Adaptive optics (AO) is a technology originally introduced for astronomy as a solution to overcome fluctuating aberrations introduced by changes in the transmission path through the atmosphere such as turbulence, temperature and density gradients which degrade the quality of images. Horace W. Babcock is regarded as the first to propose the use of AO [35] in observational astronomy. In 1953, he suggested using a deformable optical element controlled by a wavefront sensor to cancel out atmospheric distortion in order to improve telescope images.

Initially, AO techniques were hugely expensive and so were mainly developed and applied to astronomy and to military applications. They quickly became essential parts of astronomical telescopes and military imaging systems [36]. More recently, comparatively low-cost but nevertheless powerful and robust adaptive optics have become available thereby enabling the use of AO in research and industry. Furthermore, AO are nowadays even mass-produced and integrated in consumer electronics. A Japanese maker employs AO in a DVD player in order to compensate for aberrations caused by slight bends of the DVD disc [37].

AO are usually used for two main purposes (according to [36]):

- Dynamic compensation of optical distortions and aberrations in real time: these corrections can provide a vast improvement in the spatial resolution and contrast of an optical system and are applied to imaging, confocal microscopy, laser beam delivery (see section 2.3.3.7) and in instruments for ophthalmic diagnosis (section 2.3.3.5).
- Modification of the characteristics of an optical system in order to obtain an intended optical output. In this context, both control of laser beam profile and control of laser pulse are important with potential applications to a wide range of laser machining applications (see sections 2.3.3.7 and 2.3.4.3).

A standard AO system consists of three main elements, i) a wavefront modulator, ii) a wavefront sensor and iii) a control or feedback system (see Figure 2.4). These elements are also referred to as hand, eye and brain of the AO system.

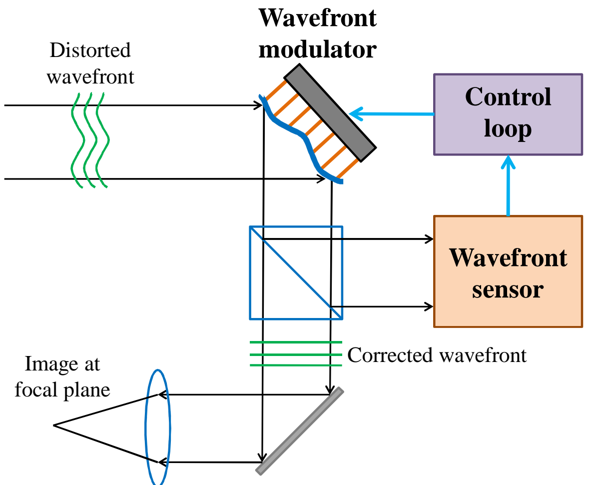

Figure 2.4: Schematic an Adaptive Optics system, consisting of wavefront modulator, wavefront sensor and control loop, for wavefront correction.

A wavefront modulator (WFM) is used in order to modify the optical phase profile of a wavefront. For this purpose the control of the optical path difference (OPD) is essential, where n is the refractive index and Δz is the difference of the geometrical path lengths:

$$OPD = n \cdot \Delta z; \qquad \text{Equation 2-3}$$

This can be related to the phase φ of a wave with wavelength λ:

$$\varphi = \frac{2\pi \cdot OPD}{\lambda}; \qquad \text{Equation 2-4}$$

Some wavefront modulators are based on a continuous mirror surface as opposed to a segmented or pixelated reflective surface. The most common wavefront modulators for AO are deformable mirrors and an illustration of a typical device is shown in Figure 2.5. The shape of the mirror can be controlled and mechanically changed in real time and therefore Δz of the wavefront can be modified (see Equation 2-3 and Figure 2.5). The different types of deformable mirrors are described in more detail in section 2.3.1.

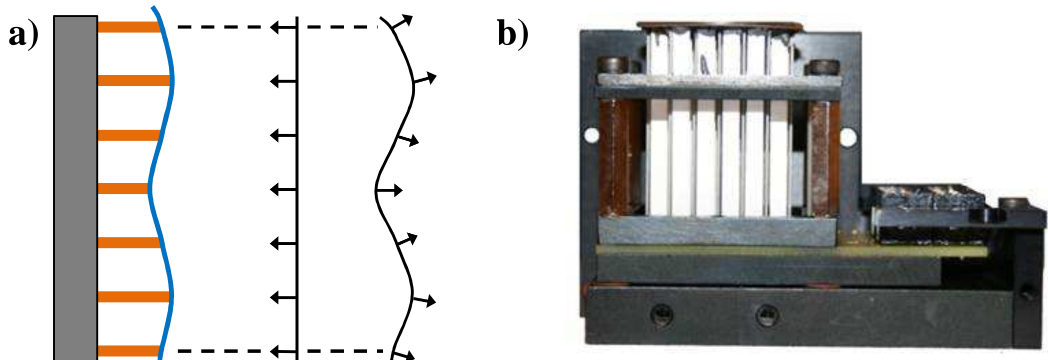

Figure 2.5: a) Principle of modulating a wavefront by means of a deformable mirror. The wavefront is altered by introducing a geometrical path difference to the deformable mirror. b) Piezoelectric deformable mirror from Oko Technologies with housing partially removed.

The phase profile of a wavefront (see Equation 2-4) can also be changed by controlling the refractive index n of a transmissive element, for example in a liquid crystal phase modulator. In this case the optical path difference (OPD) is changed by controlling the refractive index n of the transmissive element (see Figure 2.6). SLMs are described in more detail in section 2.3.4.

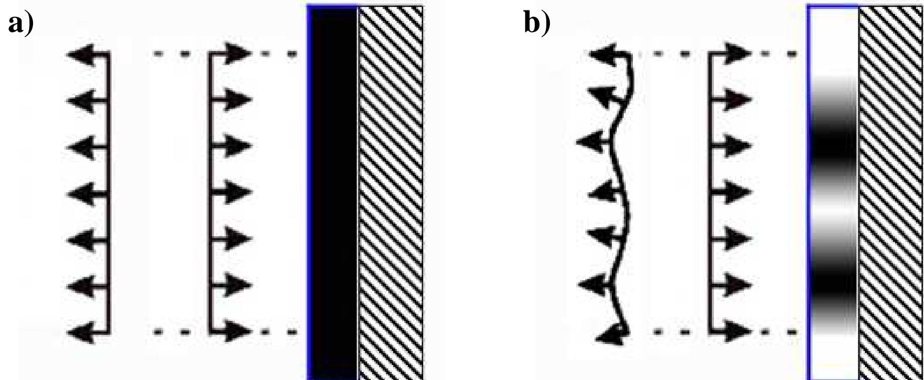

Figure 2.6: Principle of modulating a wavefront using a liquid crystal spatial light modulator operating in reflection (mirror indicated by dashed box): a) The same grey value is addressed to the liquid crystal layer (blue box) and thus the refractive index and the resulting phase delay are constant across the device. b) Varying the grey values results in a refractive index change and consequently in a varying phase delay altering the wavefront.

Liquid crystal phase modulators, i.e. SLMs, provide more freedom for the manipulation of the phase profile since single pixels of this device can be addressed and controlled individually. Typical currently available SLMs have up to 1024 x 768 or even higher pixel counts allowing the creation of highly complex and detailed phase profiles. This is in marked contrast to deformable mirrors which have a much smaller number of

control elements, typically 37 or up to 241 [38]. This limits the shape and range of shapes a deformable mirror can take on and furthermore, the shapes are influenced by the stiffness of the mirror layer and the stroke of the actuators. This key difference makes liquid crystal devices particularly suited to the correction of high-order aberrations. Liquid crystal based systems are widely used in display devices and are hence low cost. They also require only low-voltage drive electronics, unlike the high voltages required with piezoelectric devices [36]. However, liquid crystal wavefront modulators have a non-negligible absorption, especially in the visible and near infrared limiting their applications for high power beams. In addition, there are currently no liquid crystal materials with a high transmission at wavelength below 430nm [39].

In order to determine the best shape of the wavefront modulator for a certain purpose two different approaches, open-loop and the closed-loop control, can be used. Open-loop control means that there is no additional feedback control of the optical output. This approach mainly requires the knowledge of the response of the wavefront modulator and based on this the shape and properties of the wavefront modulator can be determined for a constant and known wavefront [40, 41]. The influence matrix, describing this response, may not be available for certain devices, due to non-linear characteristics, for instance hysteresis effects for piezoelectric deformable mirrors (see section 2.3.3). Additionally, unpredictable and random changes of the incident wavefront may occur. In order to compensate for this, feedback through a direct measurement of characteristic of the wavefront, such as phase, phase gradient or phase curvature [42, 43] or other desired characteristics of the resultant beam is required, which is called closed-loop control. Wavefront sensors are a powerful tool in this context and are described in the following section.

2.3.1 Wavefront sensors

For dynamic modifications or corrections of the wavefront or the beam shape, appropriate feedback is required which provides a fast measurement with sufficient resolution of the optical profile. The optical wavefront cannot be measured directly and thus different wavefront sensing techniques have been developed, based on an intensity measurement which has a defined relationship to the wavefront profile [36, 42]. Using this relationship, the shape of the optical wavefront can be reconstructed and then applied as feedback for correction or manipulation. In the following sub-section the

most popular methods for wavefront measurement are described. However, a complete wavefront measurement is not necessarily required, especially if the wavefront has to be optimised with respect to only a single target plane.

For the experimental work described in this thesis, the quality of laser machining results is the ultimate criterion for the optimisation. For certain processes and materials, like laser ablation of non-transparent coatings on transparent materials, this can be directly measured [44]. However, for laser machining processes with bulk materials, a direct feedback of the laser machining outcome would require the development of a complex sensing method. Hence the laser beam will be optimised regarding the intensity distribution of the focussed laser beam at a target plane, i.e. typically the work piece. Hence, a measurement of the phase of the wavefront, e.g. using a Shack-Hartmann wavefront sensor, can be simplified and an intensity measurement can be sufficient for the closed-loop feedback.

2.3.1.1 Interferometric sensing

The standard interferometric sensing method uses a coherent light beam which is split into two near identical parts where one beam is allowed to interact with a target and the second beam is a reference beam. The phase difference introduced in the two beams by the interaction with the target by one beam contains all the pertinent information on the shape or phase differences introduced by the target. In order to get reliable feedback, multiple measurements or intensive calculations are required limiting the applications for real-time wavefront modifications [42].

2.3.1.2 Hartmann- / Shack-Hartmann sensor

Hartmann- and Shack-Hartmann wavefront sensors are widely used within AO systems and classified as a geometric sensing technique. A Hartmann plate consists of an opaque mask with holes placed in the pupil plane of an optical system. Each hole acts as an aperture resulting in an array of spots within the shadows of the mask as image of the Hartmann plate. The position of each spot can be determined using a 2D detector array; each is directly related to the slope of the incoming wavefront as an average over the aperture area. The reconstruction of the shape of the wavefront is then achieved by an integration of each gradient of the wavefront through the spot position [36].

Shack improved the light-gathering efficiency of a Hartmann plate by replacing the mask of holes with an array of lenses or lenslets which furthermore also reduced the disturbing diffraction effects of the holes. The detectors are located at the focal plane of the lenslet. Shack-Hartmann type wavefront sensors enable fast measurements of the wavefront with high accuracy and inexpensive commercial devices are available for various applications. Although a closed-loop adaptive optics system controlled by a Shack-Hartmann sensors enables a good improvement of the wavefront, it does not necessarily provide the best possible result [45].

2.3.1.3 Pyramid wavefront sensor

A pyramid wavefront sensing method is introduced as an alternative to Shack-Hartmann-sensors [46, 47, 48]. A four-facet pyramid refractive element is located with its tip aligned to the optical axis. The intensity distribution of the four pupil images of this system provides information about the wavefront gradients along two orthogonal directions. The big advantage of a pyramid wavefront sensor compared to a Shack-Hartmann sensor is the variable sensitivity [48].

2.3.2 Optimisation algorithms

For a closed-loop control of the shape of deformable mirrors including its inherent non-linear response and the resulting beam shape, an optimisation algorithm is required. A systematic search is impossible in this context due to the huge solutions space for the mirror voltages. As an example a 37-element piezoelectric deformable mirror with 292 discrete voltage levels (see section 3.1.1) has a solution space with 292^{37} ($\sim 10^{91}$) elements. Hence some sort of search algorithm is essential to find a global minimum solution for a beam shaping task. Different types of stochastic algorithms are suitable and capable of finding a global minimum (or maximum) of some error function and enable the ideal control voltages and deformation of the deformable mirror to be obtained [49]. The most popular algorithms in this context are the genetic algorithm (GA) and the simulated annealing (SA) algorithm, which are described in the following sub-sections. Additionally, a number of other algorithms were successfully applied to adaptive optics:

(i) the evolutionary strategy, a technique for general optimisation similar to GA (for more information please see [50]);

(ii) the modified hill-climbing algorithm [51];

(iii) the gradient descent control algorithms [52, 53, 54];

(iv) the phase conjugate algorithm [55];

(v) and the Nelder-Mead simplex algorithm [56].

These algorithms typically require a large number of iterations which implies limitations to applications where high speed is essential. A much more efficient optimisation can be achieved by utilising mathematical modelling based on a representation of the deformable mirror surface by modes with an orthogonal basis [57, 58].

2.3.2.1 Simulated annealing algorithm

The SA algorithm is a probabilistic method for finding a global optimum for many individual variables. This is based on the theoretical description of the annealing process in solid state physics, where e.g. a molten metal is slowly cooled until it freezes at its minimum energy configuration [59, 60]. SA includes heating up and then cooling down again in order to overcome local energy-minima and to find the global minima, as the best solution of the given problem.

Within the Ultrafast Optics Group at Heriot-Watt University, the SA algorithm was successfully applied to an AO optimisation in order to create and control Gaussian and super-Gaussian beam profiles in the femtosecond (fs) regime [49]. For a detailed description of the process see [49, 59, 60]. Using the SA algorithm 100 – 2000 iterations were required, which took 5 – 100 minutes, depending on the desired target beam profile to find a good convergence for a 37 element deformable mirror (compare [49]).

The actual algorithm and its application to beam shaping using a piezoelectric deformable mirror and a bimorph mirror used in the experimental work contained in this thesis is based on the above described principles and is described and discussed in detail in section 3.2.

2.3.2.2 Genetic algorithm

The genetic algorithm (GA) is a powerful, evolutionary technique for the optimisation of non-linear systems with a large number of variables [61]. A population of

individuals is created with characteristic chromosomes. For the application within AO, each individual is equal to the shape of the deformable mirror and each chromosome corresponds to a voltage of the actuator, e.g. 37 chromosomes for a 37-element mirror. Then each individual of the population is compared regarding the fitness within the environment, i.e. the fitness to the given purpose. The best individuals of each generation are chosen to generate a new population by randomly crossing the chromosomes, i.e. the actuator voltages. In addition to that, some chromosomes are randomly altered, so-called mutated. The resulting fitness of the new generation is tested and an new generation is generated, as before until the optimum solution is achieved [61]. Regarding the application of the GA to control an AO system different timescales are reported for achieving a good convergence to the optimum solution: In [61] a maximum of 15 generations requiring 3 minutes is required for correction of aberrations in multi-photon microscopy using a deformable mirror with 37 actuators. However, others have reported between 10-50 minutes to achieve a global optimum using a 19 element deformable mirror for beam shaping of femtosecond pulses to Super-Gaussian beam profiles [62]. Further examples of the application of the GA to adaptive optics beam shaping can be found in [63, 64, 65].

2.3.3 Deformable mirrors

As mentioned before, wavefront modulators can be based on continuous, segmented or pixelated reflective surfaces. A continuous mirror enables a smooth modulation of the wavefront and is ideal for correcting low-order aberrations, such as distortions caused by the optical system or caused by smooth and continuous processes [36]. Examples for wavefront modulators based on continuous mirror surfaces are the micromachined membrane deformable mirror (section 2.3.3.1), the piezoelectric deformable mirror (section 2.3.3.2) and the bimorph mirror (section 2.3.3.3).

Devices based on segmented or pixelated mirror surface enable distinct and discontinuous modifications of the wavefront. This can be particularly beneficial for high-order or discontinuous aberrations. Segmented or pixelated devices exhibit the distinct drawback of a potential scattering from the edges of the individual mirror surfaces and also the gaps between them. This can restrict their application to high power and high precision laser applications. Example devices are described in section 2.3.3.4.

2.3.3.1 *Micromachined membrane deformable mirror (MMDM)*

The micromachined membrane deformable mirror (MMDM) consists of a very thin (0.5 to 10 µm) membrane and is controlled using a two-dimensional array of electrodes (see Figure 2.7, source [66]). Through electrostatic forces (only attractive forces) between each electrode and the membrane the shape of the mirror can be modified. The membrane is fixed at its edges leading to a significantly smaller light aperture than the mirror diameter. The standard MMDMs are produced with a diameter up to 50 mm and provide a mechanical stroke of up to 15 µm, with typically 37 active elements. It should be mentioned that the membrane mirrors are comparatively fragile and can pick up acoustic signals, which is a problem in noisy environments. Prices lie typically between $3000 and $25000 (based on [36]).

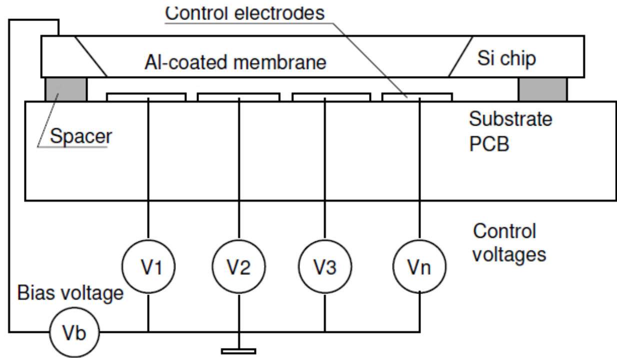

Figure 2.7: Schematic of micromachined membrane deformable mirror.

2.3.3.2 *Piezoelectric deformable mirrors*

A piezoelectric deformable mirror (PDM) consists of a thin solid plate bonded to a two-dimensional array of piezoelectric actuators (see Figure 2.8). The solid plate can be made of glass, fused silica or silicon and a coating for high reflectivity is possible. The reflective plate can be deformed by applying a voltage to an individual piezoelectric actuator leading to elongation or contraction. After setting a high voltage to a particular actuator the reflective plate is deformed and since the mechanical stiffness of the mirror surface generates a stress acting on neighbouring actuators, they are also slightly deformed. Due to this dependence two parameters are required to describe the response of a PDM, i.e. the maximum stroke of a free actuator and the maximum difference between the neighbour actuators. Commercially available PMs have a free actuator stroke of up to 8µm and, depending on the stiffness of the plate, an inter-actuator stoke of about 3µm. Common applications of PDM are corrections of low and high-order

aberrations [36]. It is important to note that piezoelectric actuators exhibit an inherent hysteresis. The application of a 37-element PDM to nanosecond and millisecond laser based manufacturing process will be described in section 3.5 and 3.6.

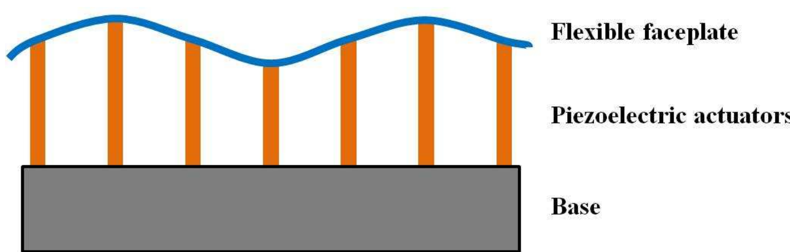

Figure 2.8: Simplified illustration of piezoelectric deformable mirror.

2.3.3.3 Bimorph mirrors

A bimorph mirror (BM) consists of a reflective surface being bonded onto a multilayer of piezo-ceramics and an appropriate pattern of electrodes [36, 39, 67]. The multilayer of piezo-ceramics has an opposite polarisation direction (see Figure 2.9) with the electrodes located in between the multilayers. Adding a voltage (V_i) to one of the electrodes results in an in-plane expansion of one layer and an in-plane contraction of the other layer. Due to the lateral confinement of the device (see Figure 2.9) this results in a bending and thus a deformation of the reflective surface which is bonded onto the piezo-ceramics. The different geometry of the actuators leads to different shapes of the mirror which can be achieved compare to a PDM. According to [68] single-channel bimorph mirrors provide a much better spherical behaviour than a single channel PDM mirror. The wavefront modulators are available up to 120 mm with different substrates, amongst others glass, copper or silicon, and water cooling channels can be integrated for high-power laser applications. Bimorph mirrors are reported to exhibit a non-negligible hysteresis of the piezoelectric layers (10.6% for a single-channel mirror [69], 2% for 35 element device from AOptix [70], and a generally non-linear voltage dependence [68]. Alternating control voltages result in a heating up of the piezoelectric multilayer which can result in significant thermal strains at the surface and an increased capacitance of the actuators [71]. Typical prices for a 40 mm diameter mirror with 19 control elements including a substantial power supply are around $10000 - $20000 (based on [36]). Further details the developments of bimorph deformable mirrors can be found in [72]. The experimental results on the application of a non-commercial 37-element BM will be presented in section 3.4.

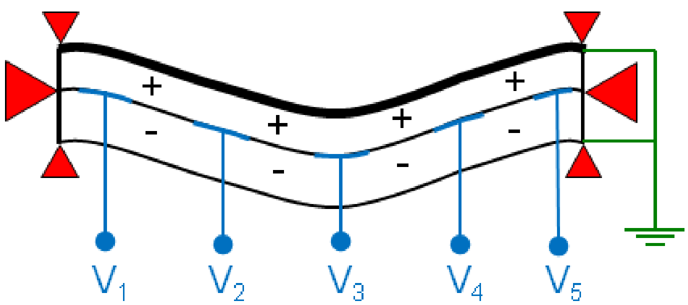

Figure 2.9: Simplified illustration of bimorph mirror. The different polarisation of the piezoelectric multilayer is indicated by "+" and "-". The red triangles indicate the lateral movement restrictions by the mirror mount.

2.3.3.4 Other types of deformable mirrors

<u>MEMS mirrors</u>

Micro-electro-mechanical systems (MEMS) mirror are available both as segmented mirrors, with typically piston but also tip-tilt control, and as continuous mirrors with discrete actuators. Their advantage is the comparatively low electric driving requirements for each actuator. Typically resolutions are 32 x 32 actuators with a stroke of approximately 2 μm [36].

<u>Digital micromirror devices</u>

Digital micromirror devices (DMD) are a special case of MEMS mirrors and were initially developed for display applications. DMD consist of an array of microscopic tilt mirrors, typically several hundred thousand. They can be tilted to two discrete states representing on-off: One state to reflect the incident light towards the optical system (on) and one towards a beam dump (off). DMDs are ubiquitous in digital computer display projectors and the mass production has led to low prices for what in effect is a highly complex device. However, they are effectively dynamic masks rather than wavefront modulators. DMD are being used in laser based manufacturing process as a dynamic mask for laser marking [73] and laser lithography [74].

2.3.3.5 Overview of applications

Deformable mirrors have been utilized in variety of adaptive optics applications which can roughly be divided into two main purposes, i.e. the correction, compensation and elimination of optical distortions on one side and conversely the modification of an optical system to generate a particular output that is the introduction of a controlled optical distortion [36]. The traditional applications for real-time compensation are in

astronomy for the correction of aberrations and distortions caused by the atmosphere and for defence applications [42]. Furthermore, deformable mirrors are widely used for microscopy [61, 75] and for ophthalmologic applications such as retinal imaging [76], vision assessment [77], cataract and cornea assessment [78]. The suitability of various types of deformable mirrors for ocular adaptive optics was analysed in [70, 79]. The following two sections focus on the applications of the different types of deformable mirrors to laser beam shaping inside and outside a laser cavity.

2.3.3.6 Application to intra-cavity laser beam shaping

If one of the cavity mirrors in a laser cavity is replaced by a deformable mirror, the geometrical properties of the laser resonator can be modified and hence allow control of the transverse and the temporal intensity profile of the beam emerging from the cavity. By reason of restrictions regarding the dimensions of the deformable mirror for the design of the laser cavity, bimorph mirrors are typically more compact and thus are favoured over piezoelectric deformable mirrors. Initial intra-cavity applications of single channel bimorph mirrors were the compensation for aberrations like astigmatism [80] or compensation for thermal lensing [81]. The application of AOs inside the cavity requires a high sphericity of the deformable surface. According to [68] single-channel bimorph mirrors provide a much better spherical behaviour than a single channel mirror with a piezoelectric actuator, which is referred to have a Gaussian-like behaviour (compare [82]). Vinewich et al. [71] showed that a single channel bimorph mirror can be used to control and stabilize the output power of an industrial CO_2 laser in the single-mode regime and also in the multi-mode regime until they reached a shape which led to laser quenching. They suggest applying this quenching as a potential optical switch for the laser cavity [71]. By applying a rectangular pulsed voltage to the deformable mirror in a dynamic control they were able to change the laser from a cw lasing mode to a repetitively pulsed mode (pulse repetition rate f= 10 – 400 Hz, pulse duration τ_p=0.6 – 50 ms) for a multimode regime.

A 37-element micromachined membrane deformable mirror (MMDM) was used by Lubeigt et al. [83] to optimise the transverse mode profile of a Nd:YVO_4 rod. The average output power from the laser could be increased from initially ~20 mW to 120 mW. In order to support this optimisation an additional tilt mirror and cavity length control are recommended. A bimorph mirror with 37-elements used as the end-mirror of a solid state laser (Nd:YAG slab laser) enhanced the far-field brightness of the laser

by a factor of 2.2 and significantly improved the beam quality product (M^2 reduced from 4.2 to 2.8) [84]. Using a 37-element MMDM mirror controlled by means of a genetic algorithm inside a solid state laser resonator, the brightness can be increased by a factor 10 [85]. The GA is reported in this context to be reliable in finding an optimum solution, though the required optimisation time could potentially limit its application. Simulated annealing was also successfully applied for this application being by a factor 3 faster in finding an optimum solution compared to the GA. However, a careful and rather time intensive adjustment of the parameters of the SA to the particular optimisation task was essential [85]. Using a random search algorithm is therefore recommended as compromise solution between the quality of the optimisation and the required time for the application [85]. Furthermore, [86] reports the use of a BM intra-cavity to significantly reduce the required time-to-full-brightness of a solid state laser.

With femtosecond lasers, BM were successfully applied intra-cavity for phase compensation as part of the compressor [39] and for phase shaping and optimising the pulse duration [87].

2.3.3.7 Application to extra-cavity laser beam shaping

Outside the laser cavity AOs can provide benefits for various applications such as laser scanning, laser communications, laser materials processing and laser fusion [36]. In the area of laser materials processing deformable mirrors have been applied to beam delivery, focus control and furthermore, but so far only to a limited extent, for the control of the beam shape:

A piezoelectric driven deformable mirror can compensate for the varying distances between the laser source (CO_2) and processing head when using a flying optics arrangement [88]. By locating the mirror between resonator and beam waist of the unfocussed beam, it is possible to keep the distance between beam waist and focussing optics constant and by doing so to obtain constant focal position and radius despite a movement of the scanhead. Locating the mirror behind the beam waist of the unfocussed beam and close to the focussing lens enables modifications to the focal position (compare [88]). By using a combination of two deformable mirrors one can enhance the control characteristics, e.g. the range of focussing, regarding flying optics [89, 90]. The application of only one deformable mirror, nevertheless, provides sufficient control over the main characteristics of a focussed beam in a laser machining

workstation such as beam waist diameter and position, radiation intensity and length of caustic [91, 92, 93]. [8] reports using a bimorph mirror for the control of these main characteristics, resulting in a reduction of the surface roughness of a cut by a CO_2-laser system by a factor of 1.5 and simultaneously in an increase of the depth of high-quality cutting by a factor of 3.

Besides the possibility of using deformable mirrors in an AO setup to control the focal position and focal spot size of a laser system, the ability to modify the spatial beam profile is very promising regarding laser machining applications. A beam shaping system using a deformable mirror with 9 moveable and 4 stationary elements controlled using a genetic algorithm was demonstrated to modify an initial Gaussian shape towards a square contour with limitations caused by the deformable mirror [64] (see Figure 2.10, source [64]).

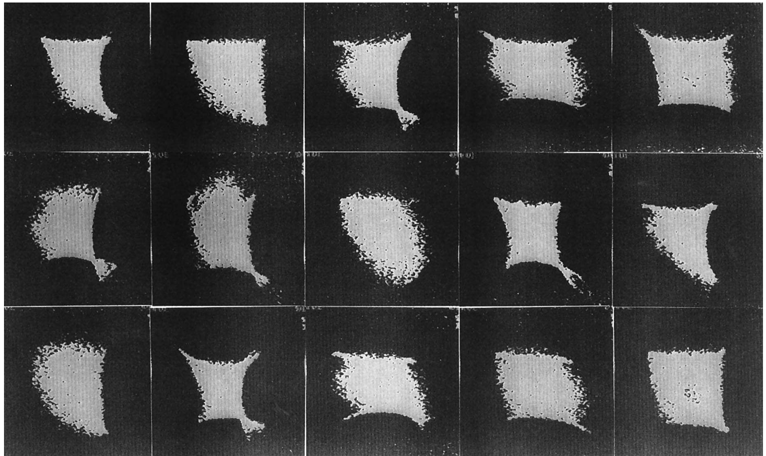

Figure 2.10: Laser beam intensity profiles for beam shaping using deformable mirror and genetic algorithm (GA). The profile at bottom right represents the elite of the 99th generation of the GA.

A 37-element micromachined deformable mirror controlled by means of a simulated annealing algorithm was shown to be capable of modifying the initial Gaussian beam shape of a femtosecond laser, on demand, towards Gaussian and super-Gaussian beam shapes with different diameters [49]. Dependent on the target profile, optimisations required between 100 and 2000 iterations of the SA to achieve a good convergence and this typically required 5 – 100 minutes (see [49]).

An AO system based on a 19-element bimorph deformable mirror and a genetic algorithm control was shown to successfully compensate for phase aberrations and to

significantly improve the far-field intensity distribution [62]. A timescale of 10 - 50 minutes was required for this optimisation.

A method to use a bimorph deformable mirror with 19-elements to change a Gaussian intensity profile towards a doughnut profile in the focal region is presented by Boyko et al. [94]. This approach is based on inducing a π-phase shift to the central region of the beam causing a destructive interference at focus resulting in a ring of high intensity around a minimum intensity. The so-called doughnut profile can be applied to optical trapping and is typically generated by conventional static optics. When using a deformable mirror instead, constraints arise due to the stiffness of the reflective surface and sudden phase jumps cannot be achieved. Nevertheless, an intensity distribution with a lower intensity at the centre compared to the outer ring was demonstrated (see Figure 2.11, source [94]). The beam shaping result exhibits wings with a six-fold symmetry that can be attributed to the arrangement of the deformable mirror electrodes. The surface constraints of the bimorph mirror are reported to be the limiting factors for this beam shaping application [94]. In these experiments a Shack-Hartmann wavefront sensor (see section 2.3.1.2) was utilized to determine the response of the device to voltage changes for each actuator. Based on this response function the command matrix for the correction can be calculated. The experiment was carried out in a so-called servo-loop control which means that the initial wavefront was measured by means of the Shack-Hartmann sensor and then the required mirror voltages are calculated and applied to this device. It is reported that the correction or beam shaping is achieved in a single iteration most of the time [94].

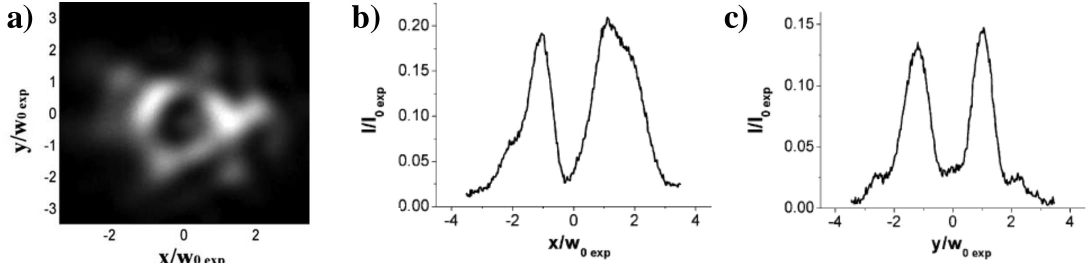

Figure 2.11: a) Beam shaping result for doughnut profile using 19-element bimorph mirror; cross-sections of doughnut profile along horizontal (b) and vertical (c) axis.

2.3.4 *Liquid crystal spatial light modulators*

The application of liquid crystals (LC) for low-cost displays is omnipresent and LC are currently extensively exploited amongst others for screens for televisions, computers, laptops and mobile phones. This section describes the basic operating principles of LC devices and displays including their distinct eletro-optic properties. Furthermore, their wide range of applications for modification of the properties of a laser beams are presented with a particular emphasis on laser processing. A good overview on the applications of liquid crystals to photonics can be found in [95].

Liquid crystals were first observed by Friedrich Reintzer, an Austrian botanist, in 1888. He discovered that cholesteryl benzoate has two distinct transition points. At one point the organic material changed into a cloudy liquid and at the other point it turned transparent [96]. Liquid crystals are a phase of matter with both physical properties of solids and ordinary liquids. They are organic molecules with a 'cigar-shape' that exhibit a lack of positional order, like ordinary liquids, however have an orientational order on a large scale (see Figure 2.12). The majority of LC materials used in displays or wavefront modulators are thermotropic which means that their distinct properties only exist within a certain temperature range [95]. A variety of different LC materials have been discovered and the most common LC mesophases are nematic, smectic A, smectic C and choloestric. LC molecules are typically rod-shaped and contain a long chain structure.

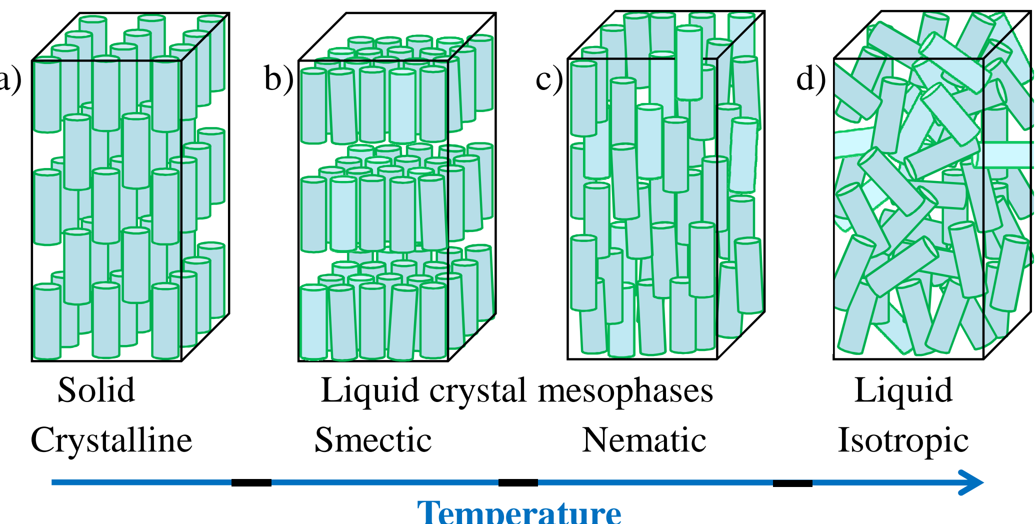

Figure 2.12: Different phases and molecular arrangements of liquid crystal materials versus temperature.

The positional and structural order of the LC molecules depends on the chemical structure and on temperature. Two mesophases exist, named smectic and nematic, with certain ordering properties (see Figure 2.12 b) and c)). A reversible transition between both phases is possible for certain temperatures. In the nematic phase, the rod-like LC molecules favour a parallel alignment along their long axes, but their centres are randomly distributed within the layer. The orientational order is stronger than thermal fluctuations in this case, however no long-range order of the molecules can be observed [95, 97]. In the smectic phase the molecules show a one dimensional translational order in addition to the orientational order. This means, that in addition to the favoured parallel orientation of the rod-like molecules the centres of the molecules are in parallel layers. The cholesteric phase also shows a nematic type of LC arrangement, however that the structure is composed of chiral molecules. As a result, the structure exhibits a twist about a helical axis that is normal to the long-axis of the rod-like molecules.

The nematic phase of LC is mostly utilized for the various applications since its eletro-optical properties are very well understood and its manufacturing and preparation is comparatively simple. Appropriate alignment layers at the interfaces of the LC layer give rise to a certain orientation of the LC molecules in their relaxed state. As a result of the rod-like structure, LC molecules exhibit a dielectric anisotropy. Thus by applying an external electric field, the orientation of the LC molecules can be changed. As a consequence, the optical anisotropy, i.e. birefringence, of the LC changes according to its orientation and hence alters the induced phase retardation of polarised light transmitted through the LC layer. This electrically controllable birefringence is the crucial property of LC for most display applications [95].

The alignment of the nematic LCs can be controlled by coating a soft alignment layer, often polyimide, onto the material the LC is sandwiched in-between, e.g. two glass plates, followed by a polishing of this layer with strokes in the desired alignment direction [97]. The rod-like molecules adjacent to this alignment layer align their long axes parallel to the direction the scratches resulting from the polishing process. In consequence of the orientational order as characteristic of the nematic phase, the molecules in the centre of the LC layer have a tendency to align in the same direction as the molecules at the interface with the alignment layer. If the alignment layers are polished in orthogonal directions, the orientation of the long axes of the molecules remains parallel in the plane parallel to the alignment layer and the glass plates.

However, in order to match the boundary conditions of the orthogonal alignment layers, the orientation of the molecules gradually rotates and a helical structure is formed in absence of an electric field (see Figure 2.13 left side, based on [98]). Such a design based on orthogonal directions of the alignment layer is called twisted nematic liquid crystal. When a voltage is applied across the LC cell, the molecules align with their long axis along the electric field and consequently the helical structure is altered to a straight alignment (see Figure 2.13, left). Due to the birefringence of the LC molecules a phase change is induced for either reflected or transmitted light, together with a change in polarisation [99].

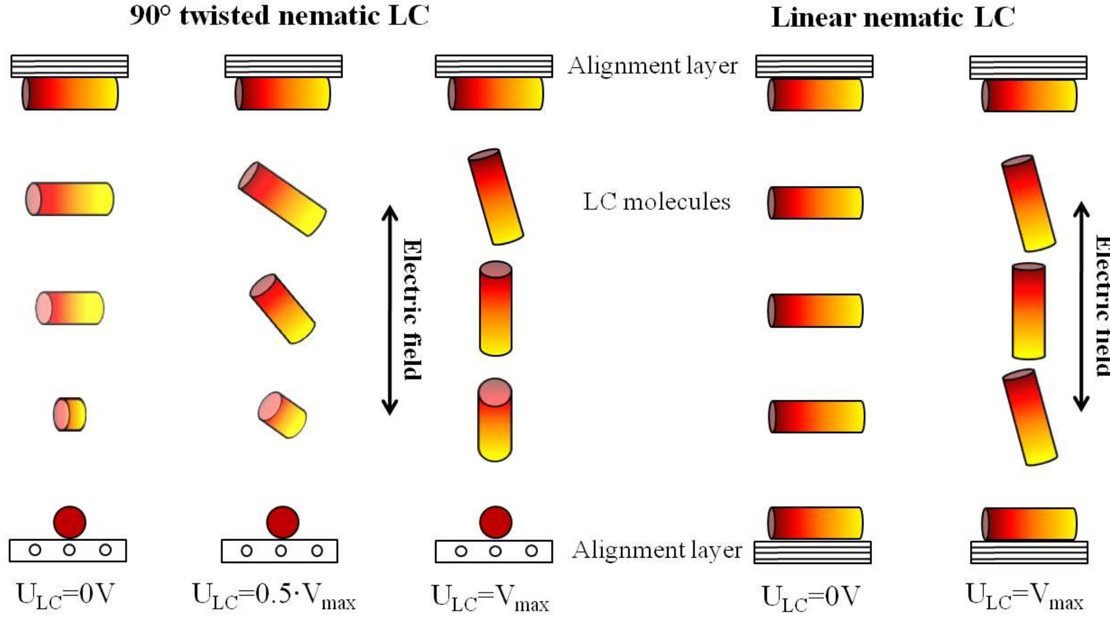

Figure 2.13: Change in the orientation of the liquid crystal molecules with increasing voltage U_{LC}: left for 90° twisted nematic liquid crystal cell and right for linear nematic liquid crystal cell.

If both alignment layers are orientated parallel to each other, the system is referred to as a linear nematic liquid crystal. An increasing voltage across to LC cell results in an in-plane rotation of the nematic molecules (see Figure 2.13, right side). Consequently, the phase modulation and the polarisation modulation do not exhibit a coupling and a pure phase modulation can be achieved for linear polarised light incident on the display.

The twisted nematic LC cell is the most common type, as the change in polarisation is important for the use as displays devices with the LC layer typically sandwiched between crossed polarisers. The LC layers acts as a variable phase retarder and phase plate which modulates the polarisation of the light and thus the transmitted intensity of

the incident light. Application areas for this approach are amongst others screens for televisions, laptops and mobile phones but the total number of applications where liquid crystals are utilized is enormous.

Aside of liquid crystal spatial light modulators based on nematic liquid crystals, ferroelectric SLMs utilize liquid crystals in the smectic phase and descriptions of their functionality and response can be found in [97].

2.3.4.1 Functionality

Spatial light modulators based on liquid crystal microdisplays are very versatile tools to modify the amplitude and phase of a wavefront. They can operate either in transmission or reflection. An illustration of the functionality when using the SLM as a phase modulator is shown in Figure 2.14 (source [95]). The SLM consists of a thin layer of LC, primarily nematic LC, sandwiched between transparent electrode layers, usually made from indium tin oxide (ITO), to control the alignment of the LC layer by means of an electric field. For SLMs working in transmission, the LC layer and the electrodes are sandwiched between typically glass substrates. A polished alignment layer as described above is added to the glass substrate (not shown in Figure 2.14). For SLMs operating in reflection, a mirror coating, typically metallic or dielectric, is added to the substrate at one side.

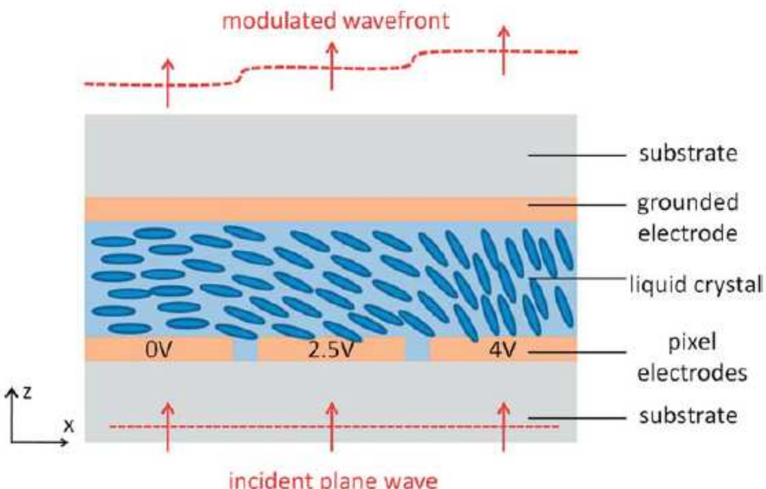

Figure 2.14: Illustration of functionality of LC spatial light modulator. The incident plane wave is polarized along the x-axis.

Besides the optical anisotropy of the LC molecules, they also exhibit a larger dielectric constant in the long axis of the molecule compared to normal to that axis. Applying an electric field between the control electrodes results in an induced electric dipole to each LC molecule and the resulting torques can change the orientation of the molecule. LC molecules sufficiently away from the alignment layer will rotate freely for strong applied electric fields and align their long axis of the molecule with the electric field [97]. Electrolytical effects caused by a DC electric field can result in physical deterioration and decomposition of the liquid crystals (see [98]). In order to prevent this, AC driving voltages are used, typically in the order of kHz. Alternatively for a pulse-width-modulated (PWM) control signal, the voltage of the ITO layer is grounded relatively to PWM pixel voltage for half of the control cycle (frame); for the second half of the frame both pixel voltage and the ITO voltage are inverted to prevent the LC deterioration (see Figure 2.15, source [100]). Once the electric field reverses, the induced dipole moment to the nematic molecules reverses accordingly and hence the alignment of the molecule relative to the electric field remains the same [97].

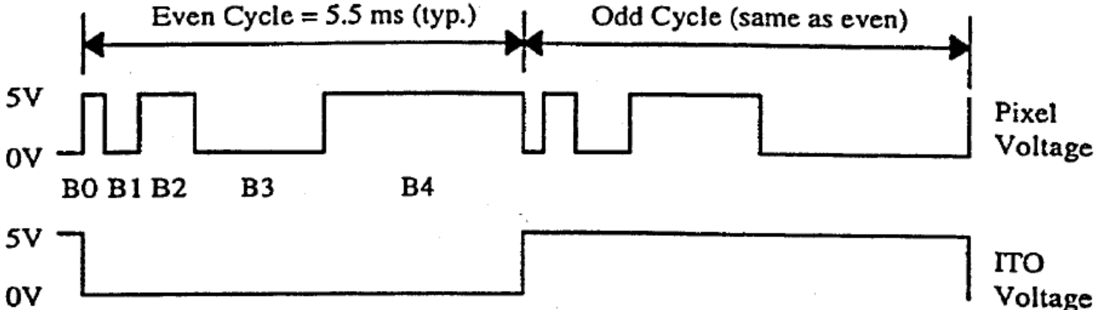

Figure 2.15: Pulse-width-modulated signal for control of LC cell including inversion of pixel voltage and ITO voltage to prevent deterioration of LC layer.

The response of the LC molecules to changes in the electric field depends on two key properties described below:

<u>Elastic constants</u>

Liquid crystals exhibit curvature elasticity and the elastic constants of the molecules describe the restoring torques for changes in the orientation due to a changing electric field. However, those restoring torques are typically weak in liquid crystals [101].

Viscosity

The viscosity of fluids determines its internal resistance to flow and movements. The dynamic characteristics of the LC layer are in particular controlled by the viscosity parameters and especially by the rotational viscosity coefficient, describing the resistance to a rotation of the molecule [101]. As with most liquids, the viscosity decreases for higher temperatures as a consequence of the higher molecular kinetic energy [101]. According to an empirical rule, for every temperature rise of 10 – 15 °C, the rotational viscosity decreases by a factor of 2 [102].

2.3.4.2 Phase response of liquid crystal layer

To quantitatively describe the anisotropic optical properties and in particularly the birefringence of the liquid layer including polarisation effects the mathematical formalism of *Jones calculus* can be used. Further details about the Jones vectors and matrixes can be found in [96, 97, 101].

For the experiments described in Chapter 4.1, the spatial light modulator LC-R 2500 from Holoeye was used containing 45° twisted nematic liquid crystals in the display. This means that the alignment layers are orientated at an angle of 45° relative to each other. The display works in reflection, giving a total rotation of the polarisation of 90°, and was originally developed for visual applications.

Different configurations regarding the polarisation state and the angle of the incident light are suggested in the literature in order to achieve a so called *phase-only* or *phase-mostly* operation for displays based on 45° twisted nematic liquid crystals [103, 104, 105]. The reported approaches use either linear or elliptical polarised light incident on the SLM and an analyzer after the display. The Jones matrix describing the phase and amplitude modification characteristics of the SLM can be determined and hence a suitable configuration deduced [103, 106]. In [107] linear polarised light incident on the SLM (LC-R 2500 from Holoeye) is suggested without an additional analyser after the SLM. This is the approach chosen for the experiments described in Chapter 4. With respect to nanosecond laser machining, high average laser powers are essential and a polarising element after the display would result in a loss of laser intensity. On the other hand, the coupling of phase and polarisation modulation can potentially also cause intensity losses of the diffraction pattern and result in an increased intensity of the inherent zero order beam [108, 109].

An alternative approach to decoupling phase and polarisation modulation is to combine four pixels of the twisted nematic liquid crystal by spatial filtering to a so-called 'superpixel' [99]. This results in independent phase and amplitude modulation characteristics of the display.

The devices used in section 4.2 and 4.3 use parallel linear nematic liquid crystals and thus induce a pure phase delay to the wavefront without affecting the polarisation direction [110, 111].

2.3.4.3 Applications to laser beam shaping

Liquid crystal spatial light modulators have a very high spatial resolution and can be programmed easily and directly to manipulate the amplitude or phase of a wavefront. This section will focus on non-display applications where the light is modulated by means of the SLM and in particular on the application of SLMs to laser beam shaping and laser materials processing:

Liquid crystal devices are widely used as tuneable filters and switches (see [95]) and as liquid crystal lenses [112, 113, 114, 115] including confocal microscopy [116]. The control of the phase delay across the SLM enables the application similarly to mirrors, prisms or blazed gratings [95]. The phase retardation due to the change of the refractive index for the pixels results in an optical path difference. A linearly variable phase delay across the display, for example left to right, introduces a tilt to the wavefront and deflects the beam at an angle depending on the level of phase shift between the left and the right side [117]. The phase retardation and the resulting tilt of the wavefront can be increased by introducing abrupt phase changes of 2π and wrapping the phase profile in a saw-tooth shape between 0 and 2π for the corresponding wavelengths. As a consequence, continuous steering of the laser beam can be achieved by altering the period or the blaze of the phase profile addressed to the SLM [118, 119]. The beam steering capabilities of are limited by potential non-linearities of the discrete phase response of the device and especially by a potential cross-talk between adjacent actuators at the locations of the abrupt 2π rad phase step. When such a transition of 2π is addressed to the display, the electric field between the adjacent pixel electrodes typically changes between its maximum and minimum value. Fringing effects of the electric field occur resulting is smear out of the phase transition [120, 121]. As a result,

for higher deflection angles the resulting steering efficiency drops significantly (see Figure 2.16, source [121]).

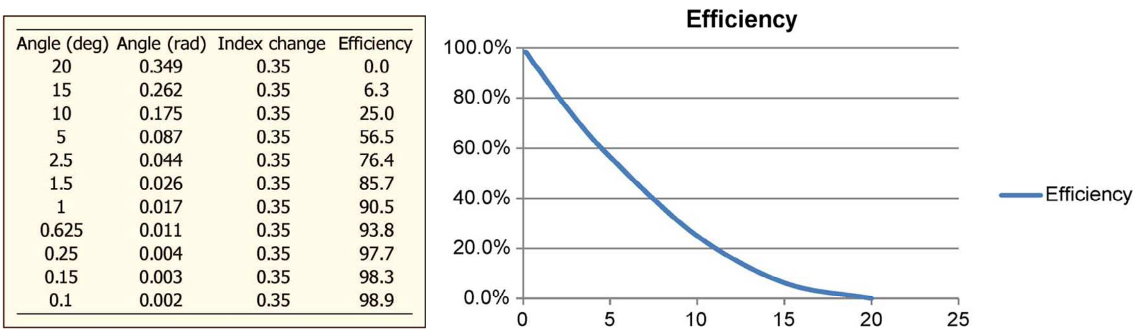

Angle (deg)	Angle (rad)	Index change	Efficiency
20	0.349	0.35	0.0
15	0.262	0.35	6.3
10	0.175	0.35	25.0
5	0.087	0.35	56.5
2.5	0.044	0.35	76.4
1.5	0.026	0.35	85.7
1	0.017	0.35	90.5
0.625	0.011	0.35	93.8
0.25	0.004	0.35	97.7
0.15	0.003	0.35	98.3
0.1	0.002	0.35	98.9

Figure 2.16: Beam steering efficiency of liquid crystal device versus angle limited by fringing field effects.

SLMs are extensively used for optical tweezers [103, 104, 122, 123] to trap and move particles based on forces generated by intensity gradients [124]. Conventional approaches use static diffractive beam splitting optics that result in multiple focussed laser spots with sufficient intensities for trapping the particles. The SLM can similarly create multiple focussed spots, but in this case their positions relative to each other can be changed dynamically.

With regards to laser materials processing, SLMs have been mainly applied to femtosecond (fs) [9, 10, 125, 126] and picoseconds (ps) [23] processes due to their limited average power handling capabilities. In these cases the SLM was utilized to create multiple laser spots for parallel processing or to create certain beam shapes for the laser writing of waveguides. For laser processing in the fs and ps regime, high peak intensities but rather low average optical powers are typical. Based on the references above for fs and ps laser processing, the display seems to cope well with these laser characteristics. The successful application of an SLM with a nanosecond laser is reported in [127], however with a much shorter pulse length and a much lower average power compared to the experimental results presented in Chapter 4.

The application of a SLM for beam shaping in the context of laser processing has been demonstrated for a wide range of applications, including laser photolithography where the SLM can be used as dynamic mask [128] or a variable diffractive optical element [129, 130], in both cases using a femtosecond laser source.

Besides pixelated, electrically control liquid crystal spatial light modulators as described above, non-pixelated optically addressed liquid crystal light valves are also available. Typically a video projector is used to define the phase delay of a matrix on the light valve and a description of the functionality can be found in [97, 131]. Such an optically addressed light valve exhibits limited power handling capabilities and as a consequence has been only utilized to spatially shape femtosecond laser pulses. Applications include fs laser micromachining [131, 132, 133] (see Figure 2.17 and Figure 2.18, source [133]) and fs laser writing of waveguides [134].

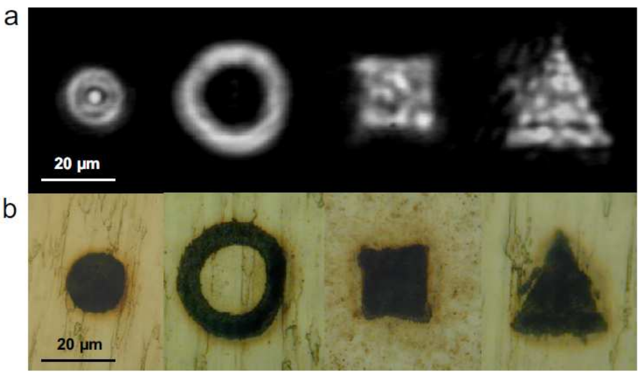

Figure 2.17: a) Beam shaping results of femtosecond laser source imaged in the focal plane; b) corresponding fs laser marking results on stainless steel.

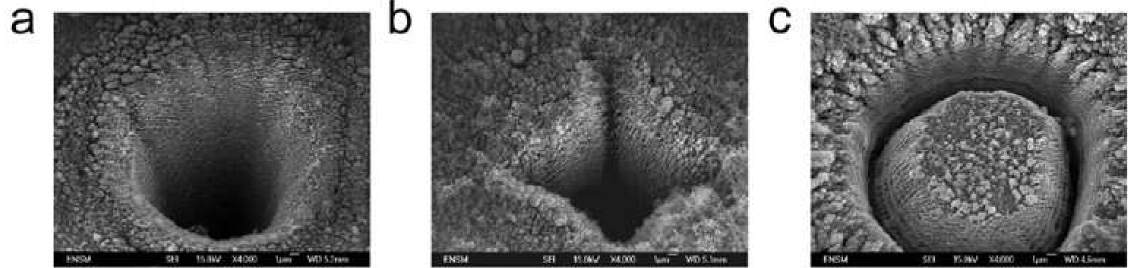

Figure 2.18: Direct femtosecond laser micro-structuring of stainless steel with user-defined focal spot shapes: a) circular top-hat, b) square top-hat, c) doughnut profile.

2.4 Summary

A Gaussian beam shape, as is typically emitted from a laser, is not always best for an application in laser processing. Whilst standard beam shaping techniques based on reflective, refractive or diffractive optics use static optical elements, Adaptive Optics have the distinct advantage that they enable dynamic modifications and furthermore enable to compensate for variations in the laser beam. Various applications, both inside

and outside the laser cavity, benefit from using a deformable mirror as fast and robust wavefront modulator. Spatial light modulators based on liquid crystal displays have a much higher spatial resolution compared to deformable mirrors and hence offer an increased control over the laser beam, however, at a lower speed. Advantages of using a SLM for laser beam shaping have been demonstrated for a variety of applications; however in the context of laser processing, the application of SLMs has been mainly limited to femtosecond and picosecond lasers due to the limited optical power handling capabilities of the devices. Overall, Adaptive Optics have a significant potential to be applied to laser-based manufacturing processes.

Chapter 3

Experimental results using deformable mirrors

This chapter describes the application of two different types of deformable mirrors, i.e. a Piezoelectric Deformable Mirror (PDM) and a Bimorph Mirror (BM), to laser beam shaping outside the laser cavity. This beam shaping technique is demonstrated with both nanosecond and millisecond pulsed laser machining workstations.

Adaptive optics (AO) based on deformable mirrors have been initially developed for astronomy and military applications with their wider application being limited by the enormous costs of these devices [36]. More recently, comparatively low-cost but nevertheless powerful and robust adaptive optics have become available, and as a result deformable mirrors have started to play a substantial role in research and industry.

The typical Gaussian intensity distribution generated at focus of a laser machining workstation is not always ideal for the application; instead other shapes such as ellipses, flat-tops (circular or square), or doughnuts can in some cases give better results. Also, other more complex beam profiles or the generation of specific patterns might be beneficial for surface micro-structuring. Using fixed optics, e.g. refractive optics (see section 2.2.2) or diffractive optical elements (DOE, see section 2.2.3), a wide variety of different beam profiles can be created by using a customised fixed element [4, 6, 135]. Adaptive Optics (AO) in contrast have the advantage of enabling highly dynamic changes on the timescale of milliseconds which means that the beam shape can be altered 'on-the-fly', i.e. during the actual machining process. In order to realise, and rapidly change between such beam shapes, an AO approach was investigated based on using an iterative Simulated Annealing algorithm (SA) (see sections 2.3.2.1 and 3.2) to control the actuators of a deformable mirror in a closed-loop optimisation. Two different types of deformable mirrors, a 37-element piezoelectric deformable mirror (PDM) and a 37-element bimorph mirror (BM) were tested with respect to their extracavity beam shaping capabilities. Each of these wavefront modulators are common choices in the context of Adaptive Optics where a PDM is perceived as the more flexible and adaptable device. A BM is reported to exhibit better spherical behaviour

compared to the PDM [68] and also has a more compact design, which favours this type of deformable mirror especially for intracavity applications.

The devices and their distinct response are described in section 3.1 and the simulated annealing algorithm used for the closed-loop control of the deformable mirrors in section 3.2. The beam shaping capabilities of both devices are discussed in sections 3.3 and 3.4 for a low power continuous wave (cw) laser source. The integration of the piezoelectric deformable mirror into a nanosecond (ns) laser machining workstation is described in section 3.5 and benefits of using a square flat top beam for surface marking are presented. The next section 3.6 shows the application of the PDM for beam shaping with a millisecond (ms) laser. The laser used here has a low beam quality, i.e. is multimode, and does not exhibit an ideal Gaussian shape, unlike for the ns laser described in 3.5. Nevertheless, beam shaping can be carried out and the advantages gained by using a PDM for the laser drilling of through-holes are presented. The actual beam shaping and laser machining work presented in section 3.6 was carried out in collaboration with Dr. Jonathan Parry and resulted in the co-authorship of publication [136]. The PDM setup and configuration were based on previous research and findings by the author of this thesis as described in the sections prior to section 3.6. The author prepared and provided the control software including the simulated annealing algorithm. A typical PDM does not exhibit a perfectly flat mirror surface when at its rest position, i.e. no voltages applied. Phase stepping interferometry (see section 3.1.3.1) has been used by the author of this thesis to determine sets of actuator voltages that must be applied to the PDM to generate a flat mirror surface. In addition, an actuator voltage set that results in a phase retardation of π rad for a circular disc at the centre of the mirror have been determined using this technique in order to optimise of the beam towards a doughnut beam profile.

3.1 Devices

3.1.1 Piezoelectric deformable mirror (PDM) from OKO Technologies

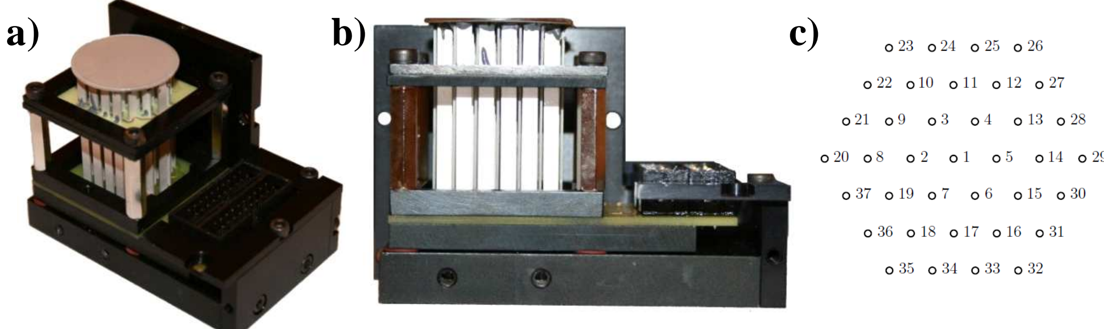

Figure 3.1: a) and b) piezoelectric deformable mirror (PDM) with housing partially removed; c) hexagonal geometry of PDM actuators including actuator numbers.

The piezoelectric deformable mirror (PDM) used in this work is a commercially available device manufactured by OKO Technologies with 37 elements arranged in a hexagonal pattern (see Figure 3.1 and Table 3-1) [137]. The individual actuators are column actuators with a thin, rectangular cross section. The electrodes are coated onto the two largest faces of the cubical actuators. The resulting electric field is applied across the thin side of the rectangular cross section resulting in a vertical expansion or contraction of the actuator in order to drive the shape of the deformable mirror substrate which is bonded on top of the actuators. The maximum free stroke of the actuators is 8 μm at a voltage of 400 V and the inter-actuator stroke, i.e. the maximum difference of expansion between adjacent actuators, is up to 3 μm due to the stiffness of the mirror substrate. The hysteresis, an inherent problem for piezoelectric actuators, is reported to be 10% [66]. The actuator capacitance is 5 nF and the frequency range is 0 – 2 kHz for the deformable mirror itself and 0 – 1 kHz for the deformable mirror unit when driven from a standard, manufacturer supplied, electronic driver board [138]. The actuators are bonded and sandwiched in between the base holder and the substrate for the deformable mirror, with an actuator pitch of 4.3 mm. The mirror substrate is a circular disc made from fused silica with a diameter of 30 mm and a thickness of ~0.8 mm. It has a high reflectivity dielectric coating for a wavelength of 1064 nm and was tested to be suitable for application with a high power nanosecond laser system (pulse length 65 ns, beam diameter 1.5 mm at the output, repetition rate 15 kHz and average power 24.5 W)[1].

[1] Damage test carried out by Dr. Jonathan Shephard (Heriot-Watt University)

The deformable mirror is driven using a high-voltage power amplifying unit from OKO Technologies providing voltages between 0 and 400 V for up to 40 channels. The output voltages used for the experiments are limited to 292 V as recommended by OKO Technologies to increase the lifetime of the actuators. The power amplifying unit is connected to a 40-channel digital-to-analogue converter unit 'DAC-40-USB' which is computer controlled via USB interface. The output resolution of the DAC unit is 12-bits providing 4096 output levels.

	PDM	**BM**
Aperture shape	Circular, Ø30 mm	Circular, Ø18 mm, Ø7 mm active area
Number of electrodes	37	37
Actuator voltages	0 … 400 V	-30 … +180 V
Hysteresis of actuators	~10%	~5%
Dielectric mirror coating	λ=1064 nm	λ=1064 nm

Table 3-1: Technical parameters of piezoelectric deformable mirror (PDM) and bimorph mirror (BM).

3.1.2 Bimorph deformable mirror (BM) from BAE Systems

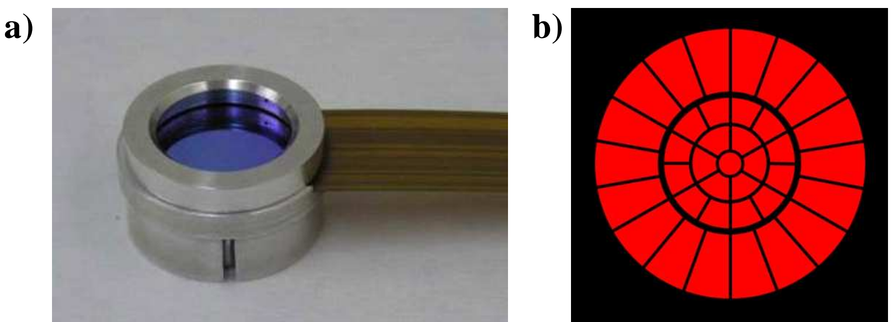

Figure 3.2: a) Bimorph mirror (BM); b) electrode pattern of BM.

The bimorph mirror (BM) used in this project was developed and manufactured by BAE Systems for their intracavity adaptive optics project (INCAO) and is not commercially available to date. The unit employs 37 active elements, i.e. the same number as the

PDM mirror by OKO, although they are arranged in a different pattern (see Figure 3.2). While the exact design of this device is confidential, a typical BM consists of a multilayer of piezo-ceramics with opposite polarisation direction (see Figure 3.3) with the electrodes located in between the multilayers. Adding a voltage (V_i) to one of the electrodes results in an in-plane expansion of one layer and an in-plane contraction of the other layer. Due to the lateral confinement of the device (as indicated in Figure 3.3) this results in a bending and thus a deformation of the reflective surface which is bonded onto the piezo-ceramics. The range of the driving voltages for each actuator of this device is between -30 V and +180 V. Positive voltages applied to the electrodes result in a transverse expansion of the actuators driving the mirror concave [139]. The lowest resonance frequency of the bimorph mirror is 2 kHz, so a maximum bandwidth of the applied signal is advised by the manufacturer to be limited to 500 Hz [139]. The hysteresis of the piezoelectric actuators is reported by BAE System to be smaller than 5% [72]. The high-voltage power amplifying unit manufactured from OKO Technologies for the PDM (see section 3.1.1) is used to drive the bimorph mirror, however, an additional DC power supply is required providing a 30 V offset in order to match the different voltage requirements. The mirror surface has a high-reflectivity dielectric coating for a wavelength of 1064 nm. The physical aperture and mirror diameter of the BM are both 18 mm but the recommended active aperture is 7 mm in diameter due to the actuator layout (see Table 3-1). A very similar mirror was successfully applied in an intracavity arrangement for enhancing the far-field brightness of a solid state laser, and extracavity for a far-field beam steering application [140].

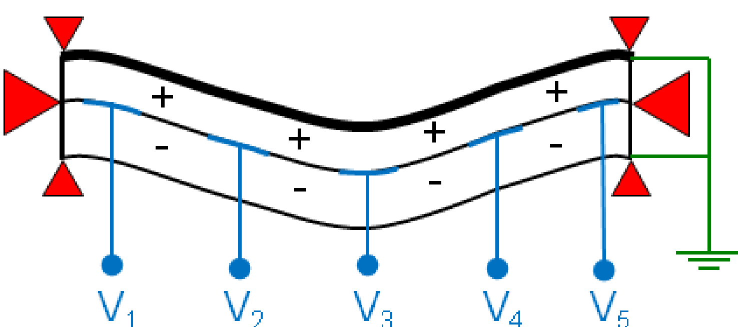

Figure 3.3: Illustration of bimorph mirror consisting of multilayer of piezo-ceramics with opposite polarization directions (indicated by "+" and "-"). The red triangles indicate the lateral movement restrictions by the mirror mount.

3.1.3 Comparison of response between a PDM and BM

A phase-stepping interferometer was constructed to measure the surface shape of both the PDM and BM and to investigate the response to changing actuator voltages on the surface shape. A detailed description of the setup and the measurement technique can be found in section 3.1.3.1 and the setup is shown in Figure 3.7. The interferometer is a Michelson arrangement and uses a HeNe laser source with a wavelength of 633 nm. The flat reference mirror in one arm of the Michelson interferometer is mounted on a computer-controlled piezoelectric translation stage to enable phase-stepping. This mirror is moved to five equidistant positions for the measurement and an intensity image is captured of each resulting fringe pattern using a monochrome CCD camera. Using appropriate algorithms [141, 142] and a standard phase unwrapping technique [143, 144], the height profile of the reflective target object, in this case the deformable mirror surface, located in the second interferometer arm can be determined. The PDM and the BM have a dielectric coating for a wavelength of 1064 nm and therefore their reflectivity at the wavelength of 633 nm, as used for the phase-stepping interferometry, is not ideal but the resulting fringe pattern still has sufficient contrast for the measurement.

Both the PDM and the BM exhibit an initial arbitrary curvature of the reflective surface as a result of the manufacturing and assembly process. In order to compensate for the initial curvature of the PDM surface a set of voltages can be determined based on phase-stepping interferometry. This set of voltages is added to the intended actuator voltages before addressing them to the device but for simplicity are not displayed in the voltage illustrations in Figure 3.4 where a) shows the flat surface profile for the PDM when only the compensational set of voltages is applied. In Figure 3.4 b) a voltage of 100 V is added to three individual actuators resulting in a strong local deformation of the mirror surface. When determining the difference between both surface profiles (Figure 3.4 c) the cross-talk between adjacent actuators is comparatively small. This behavior is also referred to as a local or zonal response.

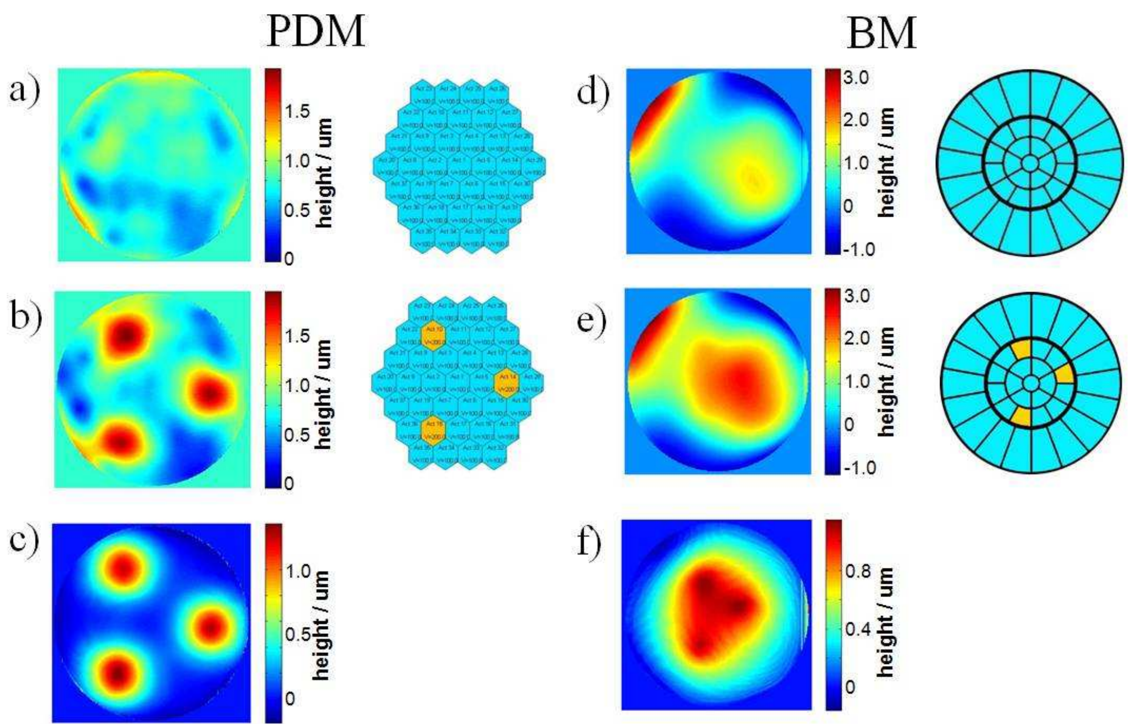

Figure 3.4: Surface profiles of deformable mirror surface (left part) with illustration of applied actuator voltage for PDM (a, b and c) and BM (d, e and f) determined based on phase-stepping interferometry: a) voltage set applied just to flatten PDM; b) 100 V added to three individual actuators of PDM resulting in local deformation; c) difference between a and b; d) no voltage applied to BM; e) 100 V added to three individual actuators of BM resulting in global deformation; f) difference between d and e.

The initial surface profile of the BM is shown in Figure 3.4 d) in its rest state with no voltage applied to the actuators. Addressing a voltage of 100 V to three individual actuators of the device results in a spatially extended deformation of the mirror surface (Figure 3.4 e). The difference between both surface profiles (Figure 3.4 f) shows a strong cross-talk between the actuators of the BM; this behaviour is called a modal response.

3.1.3.1 Phase-stepping interferometry

Phase-stepping interferometry is a powerful technique to measure the topology of optical surfaces with high accuracy [145, 146]. It enables the determination of the phase difference in interferometric measurements. Based on a single interference pattern for two interfering coherent waves the relative phase difference can be determined, however, there is an ambiguity regarding the direction of the phase change. This limitation can be overcome by analysing multiple interference patterns where the relative phases between the interfering waves are changed by a fraction of the

wavelength used in the measurement. Typically this is achieved by having a piezoelectric driven mirror in the reference arm of the interferometer.

The phase can be calculated based on at least three measurements of the intensity distribution of the resulting interference pattern at different phases [141]. Several methods and algorithms to retrieve the phase are suggested in literature: e.g. for three measurements with a phase step of π/2 or 2π/3 or for four measurements with a phase step of π/2 (see [141]). For high measurement accuracy precisely-controlled phase shifts are essential and in practice this requirement can be problematic [142]. The piezoelectric translation stages typically used to move the reference mirror for the phase stepping can exhibit for example a non-linear response and hysteresis affecting the accuracy of the phase step [146]. Furthermore, secondary effects such as temperature changes in air which alter the optical path length can cause drifts affecting the accuracy of the measurement. To address this, phase retrieval algorithms with multiple measurements based on unknown phase shifts have been presented [141, 147, 148].

The following equation for the retrieval of the phase φ based on five intensity measurements A_i (i=1,2,3,4,5) requiring equal but arbitrary phase steps was used for the experiments described in section 3.1.3 based on [141]:

$$\varphi = \arctan\left\{ \frac{2(A_2 - A_4)}{(2A_3 - A_1 - A_5)\cdot\sqrt{1 - \left[\frac{A_1 - A_5}{2(A_2 - A_4)}\right]^2}} \right\}; \qquad \text{Equation 3-1}$$

The phase step was chosen to be π/2 rad. Although the acquisition and processing of five intensity measurements, rather than four, results in an increased processing time, inaccuracies due to the increments of the phase change and vibrations are significantly reduced [141]. The result of combining the five intensity measurement using **Equation 3-1** is a phase map with values wrapped between –π/2 rad and + π/2 rad (see Figure 3.5 left column).

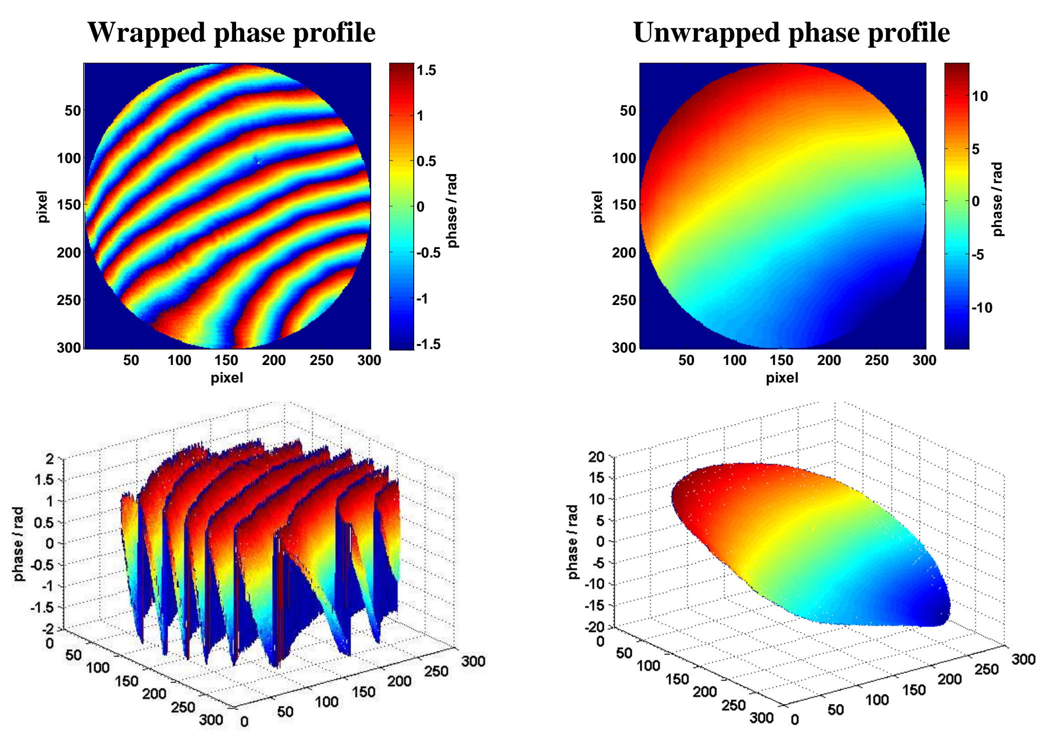

Figure 3.5: Demonstration of wrapped and unwrapped phase profile for a tilted mirrored surface.

Step 1: Reshape of matrix into vector: φ(i); (i = number of element of vector)
Step 2: Calculate phase differences: D(i) = φ(i+1) - φ(i);
Step 3: Calculate wrapped phase difference: Δ(i) = arctan { sinD(i) / cosD(i) };
Step 4: Unwrapping: Φ(i)= φ(i-1) + Δ(i);

Figure 3.6: Phase unwrapping technique.

The retrieval of the phase is followed by phase unwrapping to restore the multiples of 2π rad (see Figure 3.5 right column). An iterative unwrapping technique based on [143] is applied here. A pseudo-code of the unwrapping technique is shown in Figure 3.6. This approach compares the phase difference of adjacent actuators and removes phase jumps by π rad using trigonometric functions. More advanced but also much more computationally-intensive techniques exist for the phase unwrapping and are described in [149] and [144]. Once the phase is unwrapped (Φ(i)), height values (x(i)) can be determined by considering the wavelength λ of the used laser source based on Equation 3-2:

$$x(i) = \Phi(i) \cdot \frac{\lambda}{2\pi \cdot rad}; \qquad \text{Equation 3-2}$$

The setup for the measurements is shown in Figure 3.7. It consists of a Michelson interferometer and uses a HeNe laser source with a wavelength of 633 nm. The laser beam is expanded using a Keplerian telescope consisting of a microscope objective (20x magnification) and lens with a focal length of 300 mm. A non-polarising beam splitter cube (50 mm edge length) separates the wave into two segments with a ratio of 50:50. The flat reference mirror in one arm of the interferometer is mounted on a computer-controlled piezoelectric translation stage (Piezosystem Jena 1062) to enable the phase-stepping. The reflective surface to be measured, e.g. the deformable mirror, is located in the second arm of the interferometer. The two reflected waves are united by the beam splitter and an interference pattern is formed on a screen. A monochrome CCD camera (Basler A602f) in combination with an objective captures the interference pattern. In order to calibrate the interferometer the deformable mirror is replaced with an optically flat reference mirror (flatness λ/20 at λ=633 nm) and a phase stepping measurement is carried. This provides a measurement of the phase distortion of the optical system which can then be subtracted from all further measurements.

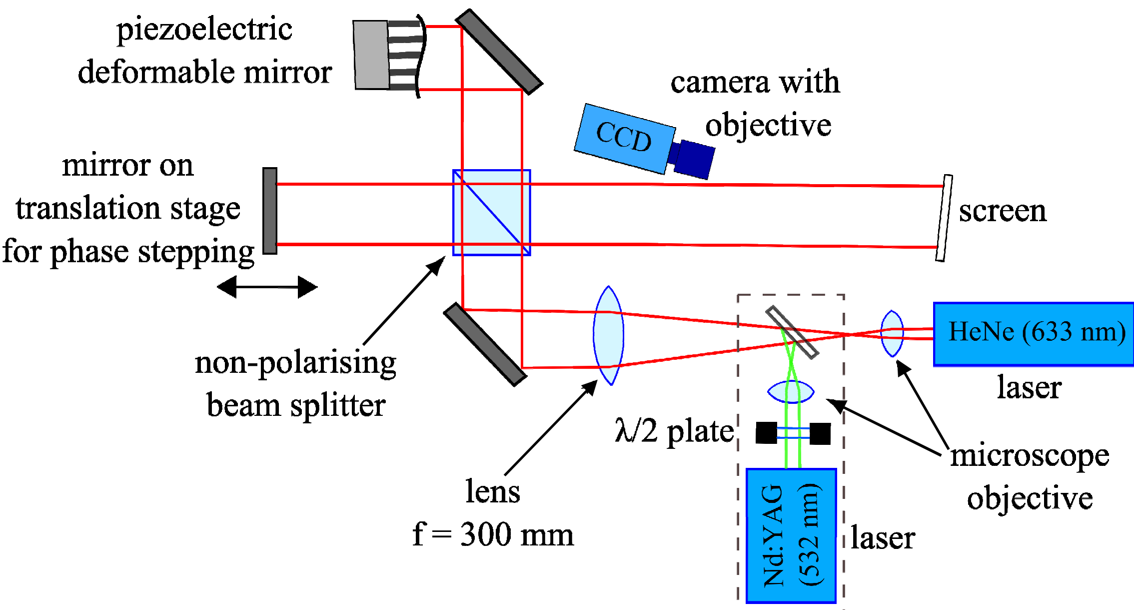

Figure 3.7: Setup for phase-stepping interferometry. The dashed grey line indicates additional components and laser source required for the measurements with the SLM (see section 4.1.2 and 4.1.3).

This phase stepping interferometer has also been used to determine the level of phase shifting present in a liquid crystal spatial light modulator as described in sections 4.1.2 and 4.1.3. For this purpose, the system was operated with a frequency-doubled

Nd:YAG laser source at a wavelength of 532 nm (see grey dashed box in Figure 3.7) and the voltages for the translation stage were adapted to achieve a phase step of π/2 for the different operating wavelength.

The laser source is embedded into the setup using a flip mirror and a microscope objective (20x magnification) for the telescope. The liquid crystal layer of the spatial light modulator consists of a birefringent material and hence an additional half-wave plate is required to align the polarisation direction of the laser relative to the display. The mirrors are all silvered and the beam splitter cube works between 400 and 700 nm, so no further amendments to the setup are required.

3.2 Simulated annealing algorithm

In principle, the voltages required to achieve a particular desired shape of the deformable mirror could be calculated on basis of an influence matrix. However, due to the actual device characteristics such as nonlinear deflections as a function of applied voltage, hysteresis, and cross sensitivities between neighbouring elements, it is beneficial to use a closed-loop control in order to optimise the actual mirror [49]. A suitable measurement system is hence required to provide feedback.

There are two main techniques applied in this context:
(i) the measurement of the wavefront e.g. using a Shack-Hartmann wavefront sensor;
(ii) the measurement of a single desired and measureable variable, like intensity, intensity distribution or beam diameter.

In the case of laser machining, the ultimate aim is the control of the beam intensity profile at focus, so the second technique is more appropriate [150]. Furthermore, the outcome of laser ablation itself can be used for the feedback as presented in [44].

Two of the most popular optimisation algorithms for finding global optimum solutions are the genetic algorithm (GA) [61, 62] and the simulated annealing algorithm (SA) [59, 60]. A more detailed discussion of the optimisation algorithms can be found in section 2.3.2. The SA is well-suited for application to control adaptive optics since it enables the optimisation of many variables at one time [151], i.e. the actuator voltages of the deformable mirror. In order to measure the variable used for the iterative optimisation,

point detectors resulting in a single scalar output [50] or CCD cameras are applied. As suggested in [49], a CCD camera at the focus of an optical system was used to measure the spatial beam profile.

The overall process flowchart of the SA algorithm is shown in Figure 3.8. The software for the algorithm was initially written by Dr. Reda El-Agmy [49] for controlling a micromachined membrane deformable mirror. It has been modified by Simon Triphan for shaping a femtosecond laser [44] and by Anja Englert for fibre coupling by means of the membrane mirror as part of their final year MPhys projects. For the application described in this chapter, the Matlab code was further adapted to control the piezoelectric deformable mirror and furthermore extensive modifications have been carried out in order to increase the speed of the optimisations.

At the beginning of the algorithm two crucial parameters of the SA need to be defined, i.e. the ‘change factor’ and the ‘temperature’ of the algorithm. The change factor is part of the ‘move class’ [152] and defines the magnitude of the random changes to generate the new set of actuator voltages, also referred to as the neighbour state, based on the current or initial set of actuators. Voltages of all the actuators are altered at the same time, though each voltage changes by a random number [0,1] multiplied by the change factor. This factor needs to be chosen carefully since if the random perturbations are too small it is likely that the algorithm gets trapped in a local minimum solution and is unable to escape due to a too small step size. On the other hand, if the change factor is too high the SA turns into a random search which is unable to zoom in to any minima solutions. The temperature of the algorithm is part of the Boltzmann probability test and will be explained below (see Equation 3-3).

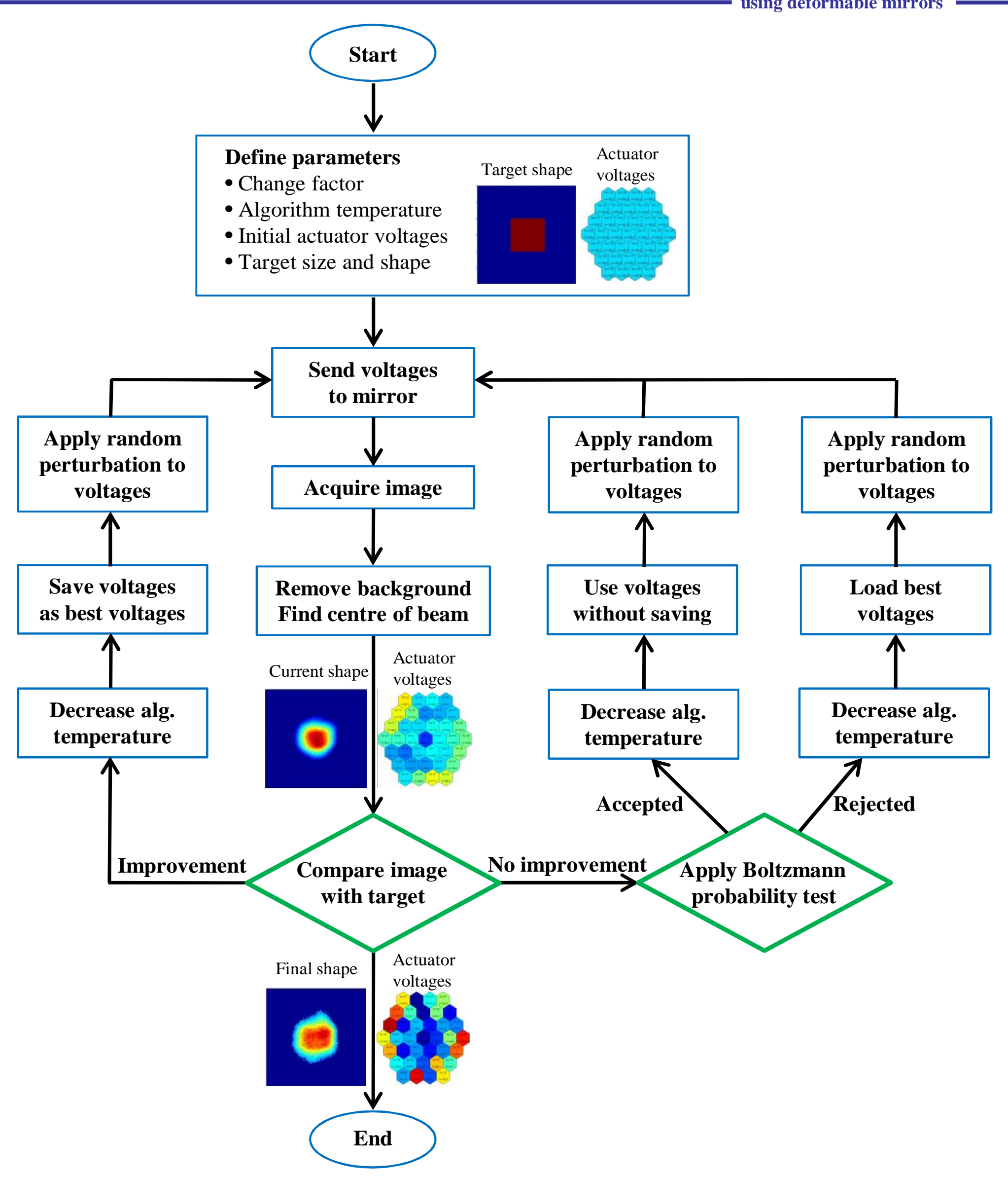

Figure 3.8: Schematic representation of simulated annealing algorithm for beam shaping with deformable mirror.

In addition to the above, a custom target profile and the initial set of actuator voltages need to be defined. Choosing appropriate starting conditions for the actuator voltages can significantly reduce the required number of iterations of the SA for the optimisation. The voltages are sent to the deformable mirror and an intensity image of the resulting beam shape is captured by means of a monochrome CCD camera. A background removal based on a subtraction of the average intensity of the four corner regions of the image is carried out. Due to the limited pointing stability of the laser the laser beam fluctuates slightly on the camera. This effect is enhanced by the comparatively long optical setup required to image the laser beam onto the camera (see sections 3.3.1 and 3.5.1). To compensate for these fluctuations, the centre of the beam

was determined by calculating its 'centre of mass' for comparison with the custom target profile.

As a quantitative measure of the correlation between current beam shape and target profile, the root mean square error (rms) between the measured intensity profile of the laser beam (I_{CCD}) and the target profile (I_{target}), both normalized, is determined in software using Equation 3-3. In the context of the simulated annealing algorithm, the rms error may be considered as the energy function that needs to be reduced towards the global minimum solution [152].

$$rms = \sqrt{\frac{1}{N_x \cdot N_y} \sum_x \sum_y (I_{CCD}(x,y) - I_{target}(x,y))^2}; \qquad \text{Equation 3-3}$$

If the new set of voltages results in an improved fitness between the beam shape and the target profile, and hence a reduced rms error, the voltages are saved and the voltages for the new iteration are altered based on the move class.

$$if \left\{ \exp\left[\frac{-(rms_{current} - rms_{best})}{T} \right] \right\} \geq rand[0,1]; \qquad \text{Equation 3-4}$$

If there is an increased rms error between beam shape and target, however, the current voltages are not always rejected. A Boltzmann probability test which is dependent on the current rms error ($rms_{current}$), the rms error of the best result (rms_{best}) and the algorithm temperature T (see Equation 3-4) is applied. The temperature T is chosen such that with a comparatively low probability (typically < 5%) the voltages are still accepted for the new iteration despite an unfavourable optimisation solution. This feature of temporarily accepting non-ideal solutions is essential to avoid the SA getting stuck in local minima solutions. The temperature T is reduced during each iteration of the optimisation by 0.1% using a standard cooling scheme [152]. Consequently, the probability of accepting solutions with an increased rms error reduces throughout the optimisation process and the algorithm is more likely to reach the global minimum solution.

The change factor, the algorithm temperature and, to a lesser extent, the cooling scheme, all have a significant impact on the performance of the SA optimisation and the required number of iterations, and thus need to be selected carefully depending on the actual optimisation problem. Typically between 1000 and 5000 iterations have been chosen for an optimisation, each time carried out with two to three different temperature values and four different change factors. Change factors resulting in a relative change between 1% and 5% worked best in this context. Each iteration of the algorithm took ~0.22 s. This could be reduced by using a camera with a higher frame rate than the 10 Hz rate used in this case and also by using a more efficient programming language than Matlab. When defining appropriate starting conditions for the mirror voltages the number of iterations required for the optimisation can be significantly reduced. However, for many laser processing applications the time required for the optimisations is not a limiting factor. Appropriate voltage values for the desired beam shape can be determined and optimised prior to the laser machining and then addressed to the deformable mirror during the process with little or no further optimisations required.

3.3 Beam shaping capabilities of piezoelectric deformable mirror

3.3.1 Low power setup

Initially, the piezoelectric deformable (PDM) mirror is tested with a low power laser source (a continuous wave (cw) Nd:YAG laser with a wavelength of 1064 nm). The setup used is shown in Figure 3.9. The laser intensity is attenuated by means of a half-wave plate and a polarising beam splitter resulting in an 'eye-safe' experiment. A telescope arrangement with a magnification of 19x is required to increase the beam diameter to match the diameter of the PDM. The laser beam diameter was increased to 27 mm ($1/e^2$ of intensity) and the beam was incident on the PDM at an angle of 10° to the surface normal. After the PDM a second 5x de-magnifying telescope (focal lengths 400 mm and 80 mm) arrangement and a focusing lens (f = 1 m) create a focused spot of suitable size on a monochrome CCD camera placed into the focal plane of the system for the optimisations. Neutral density filters placed in front of the camera are used to attenuate the intensity and prevent saturation. Small variations in the lateral position of the focused beam on the CCD camera due to vibrations and the limited pointing stability of the laser (amplified by comparatively long optical path length) are compensated by determining the centre of the laser beam by a centre of mass technique in software. The actuator voltages are controlled closed-loop by means of the simulated

annealing algorithm (SA, see section 3.2). The parameter to be minimised using this algorithm is the root mean square error between the current beam profile and a custom defined target profile according to Equation 3-3.

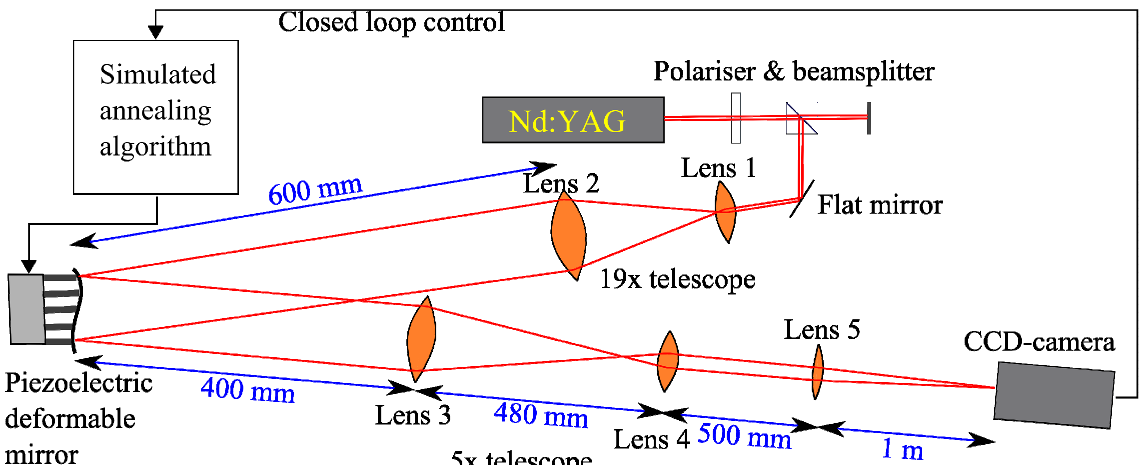

Figure 3.9: Setup for closed-loop beam shaping experiments using PDM and low power Nd:YAG laser source. Lens 1: 4x microscope objective, f=18.5 mm; Lens 2: f=350 mm, Ø=50.8 mm; Lens 3: f=400 mm, Ø=50.8 mm; Lens 4: f=80 mm, Ø=25.4 mm; Lens 5: f=1000 mm, Ø=25.4 mm.

The surface profile of the PDM exhibits an intrinsic curvature when the same voltage is applied to all actuators. Hence it has been necessary to determine a set of voltages resulting in a flat mirror surface by means of the phase-stepping interferometer (see section 3.1.3.1). These voltages were applied to the PDM as starting conditions for the SA optimisations. At some point during the actual use of the PDM, the device developed a fault causing a relatively strong curvature, acting like a cylindrical lens (see Figure 3.10). After this fault, the operating conditions of the device became somewhat limited in that around 50% of the available stroke of the actuators was required to compensate for this curvature. Fortunately, the remaining actuator stroke was sufficient for our application. In general, the voltages required for a flat mirror surface varied significantly over time with use of the device indicating a strong ageing effect of the actuators used in this PDM device. Hence a rather time-intensive determination of the actuator voltages for a flat surface had to be carried out prior to any experiment. It is unclear how far this is a generic characteristic of these devices or just an unfortunate fault with this particular unit. However, it is potentially a severe drawback for any application of the PDM in a ns laser machining application to generate 'on-the-fly' changes of beam shapes based on pre-determined and pre-optimised actuator voltages.

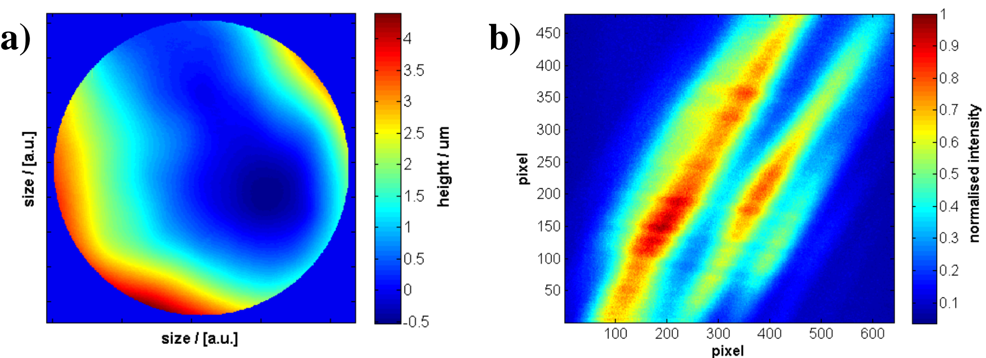

Figure 3.10: Surface profile of PDM when 147 V applied to all actuators; b) resulting beam shape at focus of the setup shown in Figure 3.9 (1 pixel = 5.6 µm).

3.3.2 Optimisations towards different beam shapes

<u>Doughnut shape</u>

Figure 3.11 a) shows the Gaussian beam profile of the beam focused on the camera when the deformable mirror in the setup shown in Figure 3.9 is replaced with an optically flat reference mirror. The first beam shape that was attempted to be formed was a ring focus, or "doughnut" profile. As a starting point, a flat mirror surface was determined by means of phase-stepping interferometry (see section 3.1.3.1). Voltages corresponding to a phase delay of π rad were added to the central 7 actuators following Boyko et al. [94]. Ideally, a circular disc at the centre with a phase difference of π rad changes a Gaussian beam shape into a doughnut shape at focus [153, 154]. The dimensions of the resulting beam profile are a guide to the choice of the dimensions of the doughnut target profile. Thus any requirement for the PDM to provide global focusing or defocusing in addition to beam shaping is avoided. Good alignment between the centre of the PDM and the centre of the incoming laser beam is beneficial and particularly important when optimising towards circular symmetric target profiles like the doughnut profile. The target profile and the beam shaping result after 2000 iterations using SA are shown in Figure 3.11 b) and c). The result has, as desired, a higher intensity in at the outer part of the beam compared to the centre. However, a closed ring structure and an even intensity distribution around the ring could not be achieved. At the centre of the beam shape a triangular structure can be observed implying a link to the hexagonal arrangement of the actuators. Figure 3.11 d) shows the development of the rms error throughout the optimisation. The main improvements are achieved within the first ~200 iterations and then optimisation appears stuck at this solution except a minor improvement after ~670 iterations.

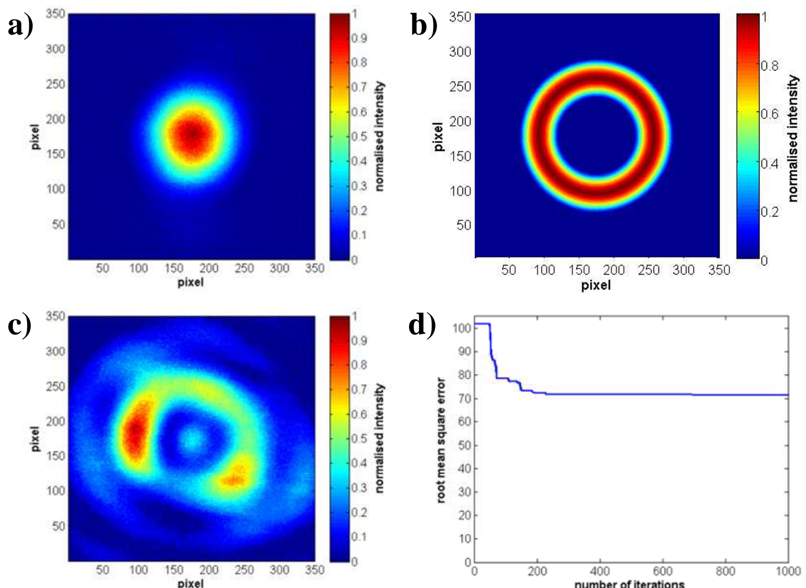

Figure 3.11: Beam shaping results using PDM: a) beam profile for flat reference mirror (1 pixel = 5.6 µm); b) target profile for doughnut shape; c) beam shaping result for doughnut shape after 1000 iterations; d) development of root mean square error throughout iterations.

Variable homogenizer

In the next step, the application of the PDM as a "variable homogenizer" was tested. For certain surface micro-structuring applications a flat and homogeneous intensity distribution at the centre of the beam might be beneficial compared to the Gaussian shape. Optimisation towards circular flat top profiles with different target diameters were carried out by means of the PDM and the SA and the results are shown in Figure 3.12. There is an obvious trade-off between beam quality and beam shape since the beam quality product M^2 increases from ~1.4 to ~2.7 for increased target profiles. The PDM enables the generation of an increased size of uniform intensity distributions at the centre of the beam; however, the intensity gradient at the slopes is still apparent and can have a potential impact on the laser machining.

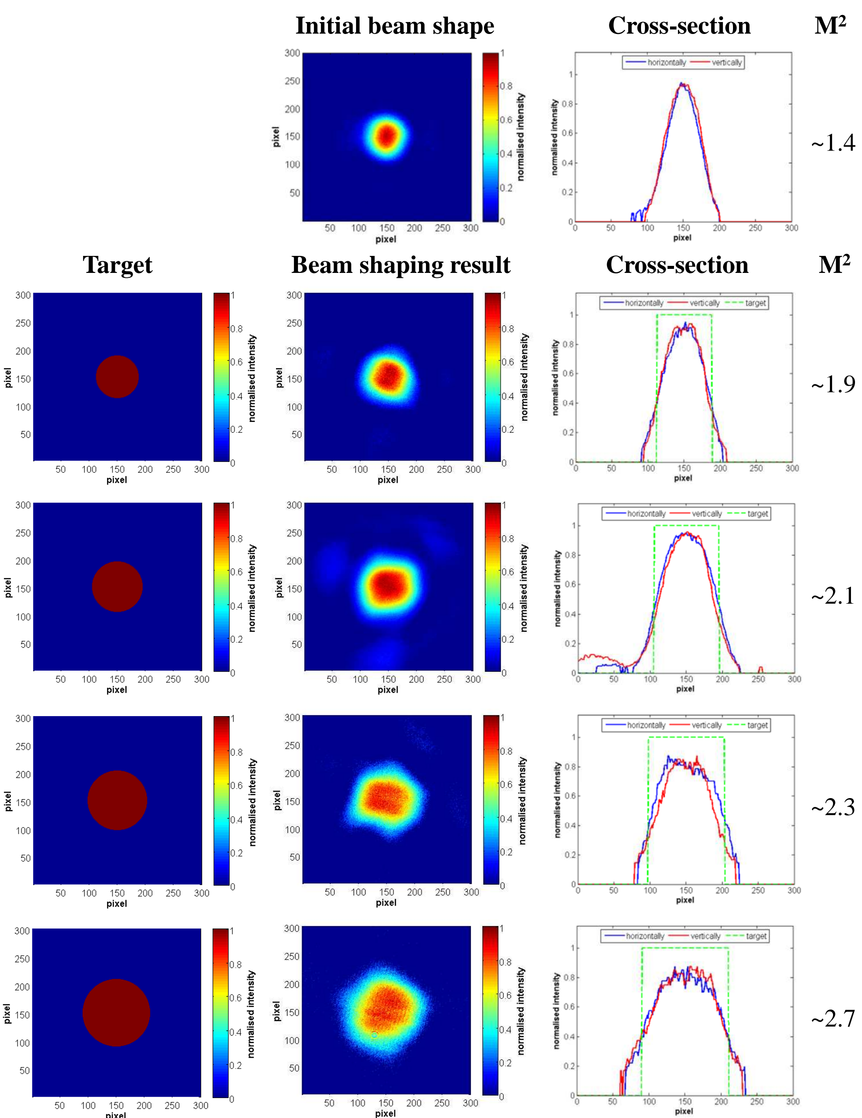

Figure 3.12: Top row: Beam profile with flat reference mirror; below: Use of PDM as variable homogeniser with different circular flat top target profiles (left), the beam shaping result after 2000 iterations of SA (middle) and the cross-sections along the horizontal and vertical direction (right). 1 pixel = 5.6 µm.

<u>Square flat top</u>

A beam shape of particular interest for laser machining of larger surfaces is a square flat top profile. A uniform overlap of consecutive laser pulses can be achieved with this beam shape compared to the Gaussian beam and thus a homogeneous machining of the surface can be expected. As a starting condition a flat mirror surface was chosen. The target profile and the beam shaping result after 2000 iterations are shown in Figure 3.13. At the centre of the beam there is an expanded area with uniform intensity in a square-like shape as desired. The hexagonal shape of the lower intensity region is again implying a link to the actuator arrangement.

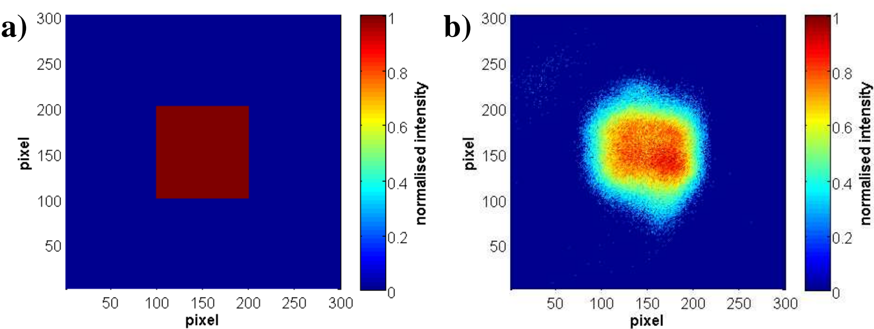

Figure 3.13: Beam shaping using PDM and SA: a) square flat top target profile; b) beam shaping result after 2000 iterations (1 pixel = 5.6 µm).

Besides the beam shaping results presented above, a variety of target profiles with different sizes and shapes and optimisation parameters of the SA have been tested, however, in most cases with a rather limited success. Besides that, the laser beam diameter incident on the PDM was changed by altering the first telescope and also the position of the second telescope and the focussing lens relative to the PDM was varied. Nevertheless, a significant improvement of the beam shaping capabilities of the PDM compared to the results presented above could not be achieved. The small number of active elements of the PDM, the crosstalk between adjacent actuators, and the constraints on the maximum achievable slopes of the deformable mirror are the limiting factors for the beam shaping.

3.4 Beam shaping capabilities of bimorph mirror

3.4.1 Setup

For testing the bimorph mirror (BM) a very similar setup to that explained in section 3.3.1 and shown in Figure 3.9 is realized except that the first telescope has a smaller magnification factor, i.e. ~5 (10 times magnification microscope objective with f=15.8 mm and f=80 mm lens), due to the much smaller active aperture of the mirror, i.e. 7 mm. This also means that the second telescope after the deformable mirror is not required. As before, the BM was located at the back focal plane of the 1 m focusing lens.

3.4.2 *Optimisations towards different beam shapes*

Elliptical beams

Given the measured modal response (see section 3.1.3) of the BM and in contrast to the zonal response of the PDM, the BM may be considered more as a "deformable lens" rather than as a phase plate. The benefits of the circular symmetry of the arrangement of the electrode pattern of the mirror (see Figure 3.2 b) can be observed when optimising an incident circular Gaussian beam towards an elliptical beam profile that is orientated in different directions as shown in Figure 3.14. The elliptically shaped target profiles for this optimisation were generated based on Gaussian intensity distributions with an aspect ratio of 3:1. The different orientations were obtained by a standard rotation of the coordinate system. For these optimisations 5000 iterations with the simulated annealing algorithm were carried out starting with a fairly flat mirror surface. The optimisation with 5000 iterations took 18 minutes. The biggest improvement of the beam shape happened in all cases within the first 500 iterations and just slight improvements occurred after that. A typical development of the rms error throughout the optimisation is shown in Figure 3.15 for the beam shaping result shown in Figure 3.14 e). No particular preferred orientation was observed which indicates that the mirror responds equally in all elements and has no preferential mode of deformation. As observed in 3.2.2, this is not the case for the PDM.

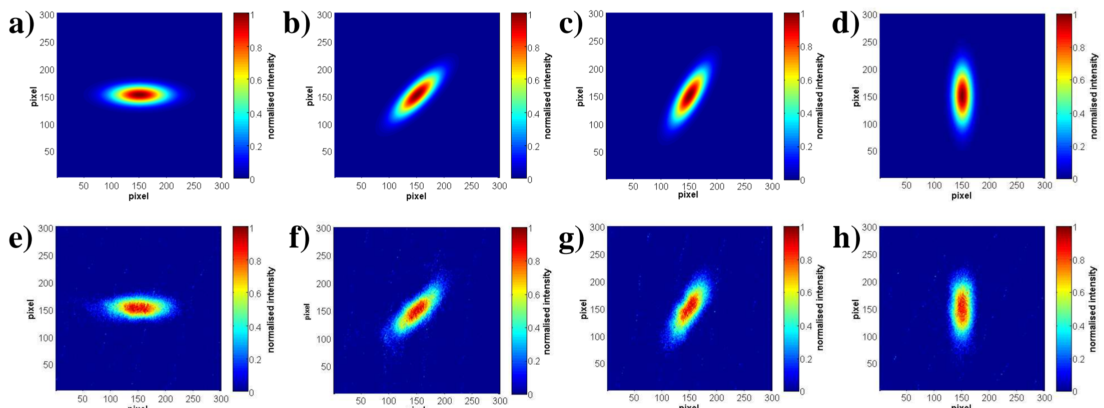

Figure 3.14: Target profiles (top row) and beam shaping results (bottom row) using bimorph mirror and SA to generate elliptical beam shapes at an angle of 0°, 45°, 60° and 90° (1 pixel = 7.4 µm).

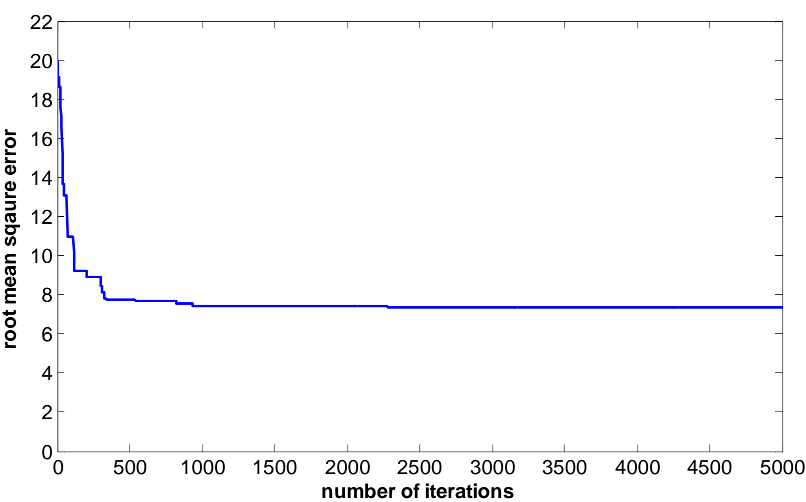

Figure 3.15: Root mean square error for beam shaping result shown in Figure 3.14 e).

A possible application of such beam shapes might be cutting and dicing applications where benefits on the cutting speed are reported when using an elliptically shaped beam where the long axis is aligned with the cutting direction [2, 3]. To date, such beam shapes have been generated using fixed optics such as cylindrical lenses. However, a deformable mirror for beam shaping has the distinct advantage that the orientation of the long axis of the ellipse can be changed during the cutting process to be aligned with the cutting direction if required. The results presented in reference [3] for dicing silicon wavers were achieved by using such an alignment technique albeit using a cylindrical lens. The work reported in [3] used a laser wavelength of 355 nm but similar benefits can be expected at any wavelength provided the laser-material interactions as a function of wavelength are considered. Provided an appropriate high-reflectivity coating is applied to the BM, the unit could equally well be used with a wavelength of 355 nm.

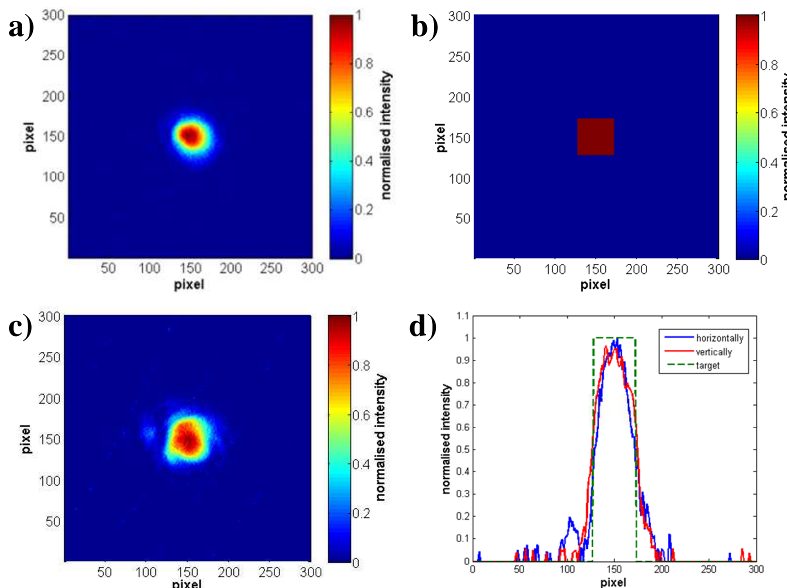

Figure 3.16: a) beam shape for flat reference mirror; b) square flat top target profile; c) beam shaping result after 5000 iterations using BM and SA; d) cross-sections along horizontal and vertical direction of beam shaping result and of target profile (1 pixel = 7.4 µm).

Square flat top

As described earlier, flat top target profiles are beneficial for a range of machining tasks and experiments were carried out to demonstrate the generation of a square flat top beam profile. Figure 3.16 a) shows the initial beam profile at focus for a flat reference mirror instead of the BM. Some aberrations of the Gaussian shape are apparent which are most probably due to misalignment of one of the telescope arrangements. Part b) of Figure 3.16 presents the target profile and part c) the beam shaping result after 5000 iterations using the BM and SA. The resulting beam shape has an increased area with a close to uniform intensity distribution at the centre. Although a square-like intensity distribution can be observed, the beam shape differs significantly from the desired target profile and it appears not to be possible to achieve a more optimised, square shaped beam pattern using the BM in combination with the simulated annealing algorithm.

Conclusions

There are a range of possible applications of this device to laser machining, for example in cutting, where elliptically shaped beams have been shown to be more efficient and enable higher cutting speeds compared to using a Gaussian beam shape [2, 3]. Also, tailoring the ellipticity of the beam to compensate for changes in the scanning speed of the galvo scanner would be a possible application. In this context, pre-optimised and

pre-determined voltage values for the desired beam shape would be used being much more repeatable due to the reduced hysteresis of the BM compared to the PDM.

For optimisation towards more complex beam shapes, such as a square flat top profile, the small number of active elements, the stiffness of the device and the strong cross-talk between adjacent actuators are the limiting factors. However, an optimisation by means of probabilistic algorithms such as the SA might not be ideal, because of the zonal response of the device, which is caused by the strong interaction between adjacent electrodes and the design based on piezoelectric multilayers. However, a more deterministic approach for example using a Shack-Hartmann wavefront sensor (see section 2.3.1.2) or using an interferometric characterisation method, e.g. according to [70, 79], to analyse the response of each individual actuator might be beneficial in this context.

3.5 Application of piezoelectric deformable mirror to nanosecond laser machining

3.5.1 Setup

The piezoelectric deformable mirror (PDM) was embedded into a high power nanosecond (ns) laser machining workstation. It is a diode pumped and Q-switched Neodymium Ytterbium Vanadate (Nd:YVO_4) system operating at a fundamental wavelength of 1064 nm with a beam quality product M^2 ~ 1.3. The pulse length is ~65 ns, the maximum average power 30 W and the laser repetition rate can be varied in the range 15 – 100 kHz. The overall setup with the PDM is shown in Figure 3.17. In order to match the beam diameter of the laser and the deformable mirror a 10x magnification Galilean telescope is required (not shown in Figure 3.17). The focal lengths of the lenses used are -30 mm and 300 mm and beam diameter was increased to 25 mm ($1/e^2$ of intensity). The angle of incidence of the laser on the PDM is 10° to the surface normal. After the PDM a second telescope is required to reduce the beam diameter to match the input aperture diameter of 10 mm of a galvanometer laser scan head system. The telescope is a Keplerian arrangement with focal lengths of the lenses of f_1 = 400 mm and f_2 = 150 mm. The galvo scanhead is equipped with an f-theta lens with f_3= 125.1 mm. Using a planar reference mirror instead of the PDM, the beam diameter in the focal plane of the scanhead is ~22 μm ($1/e^2$ of intensity).

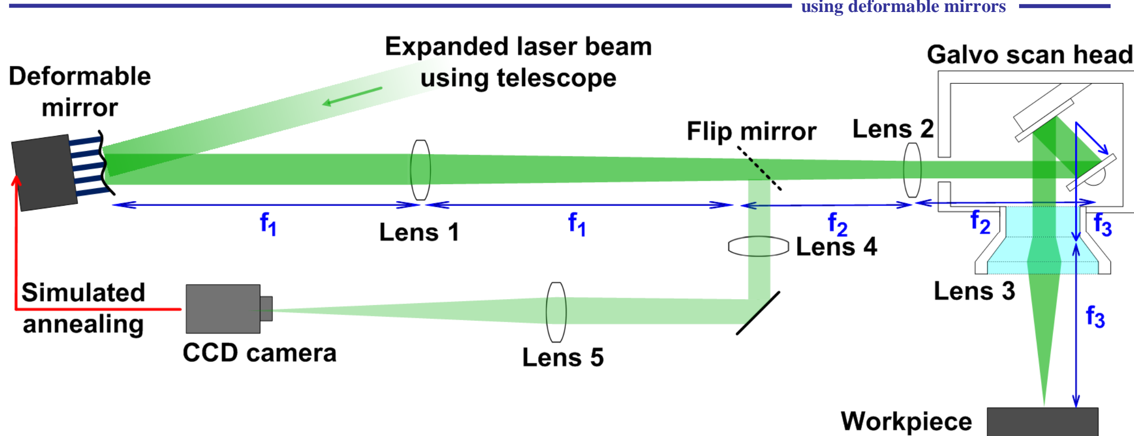

Figure 3.17: Setup for nanosecond laser machining experiments (Lens 1: f_1=400 mm, diameter (Ø)=50.8 mm, Lens 1: f_2=150 mm, Ø =25.4 mm, Lens 3: f_3=125.1 mm, Ø =127 mm, Lens 4: f=30 mm, Ø=25.4 mm, and Lens 5: f=500 mm, Ø=25.4 mm).

Using a flip mirror and two lenses (f = 30 mm and f = 500 mm) the laser beam can be focussed, as before in a 6-f arrangement, onto a monochrome CCD camera for the closed loop beam shaping. The final lens before the camera with a focal length of 500 mm ensures a sufficiently large laser spot on the CCD array. Additional neutral density filters are applied to attenuate the laser intensity. The measured beam shape is fed back to the simulated annealing algorithm (SA) for controlling the actuator voltages of the PDM. For the initial proof of concept experiment, the first step was to determine the actuator voltages for a desired beam shape by focussing the laser onto the camera and using the SA for the closed-loop control. In the second step, the flip mirror is removed and the previously determined shape of the PDM is used for the laser machining using the galvo scanhead. With regards to an industrial application of such an extracavity beam shaping technique, the flip mirror would be replaced with beam splitter reflecting a small part of the light onto the camera to monitor and if required to modify the beam shape as the laser processing takes place.

3.5.2 Laser machining results

Figure 3.18 a) shows the initial beam profile of the laser beam focussed onto the CCD camera when using an optically flat reference mirror instead of the PDM. Using the PDM, the initial Gaussian beam shape is then altered towards a square flat top profile (target profile, see Figure 3.18 b). After 2000 iterations of the simulated annealing algorithm a beam shape with an increased uniform intensity distribution was achieved (Figure 3.18 c).

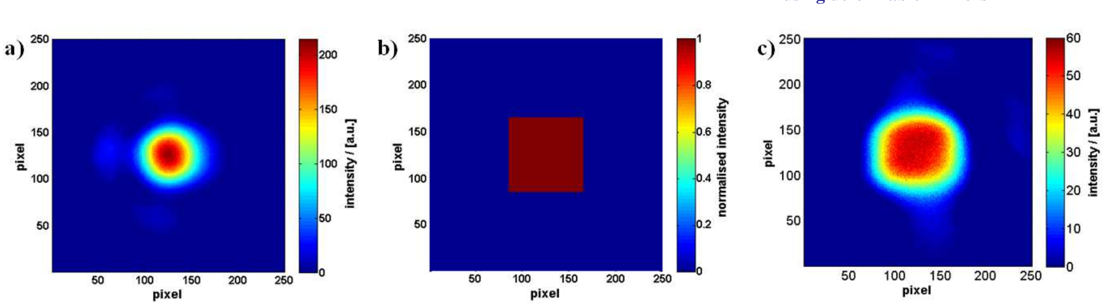

Figure 3.18: a) Beam profile at focus when using an optically flat reference mirror instead of the PDM (1 pixel = 7.4 µm); b) target profile for the optimisation; c) beam shaping result at focus with PDM after 2000 iterations of SA.

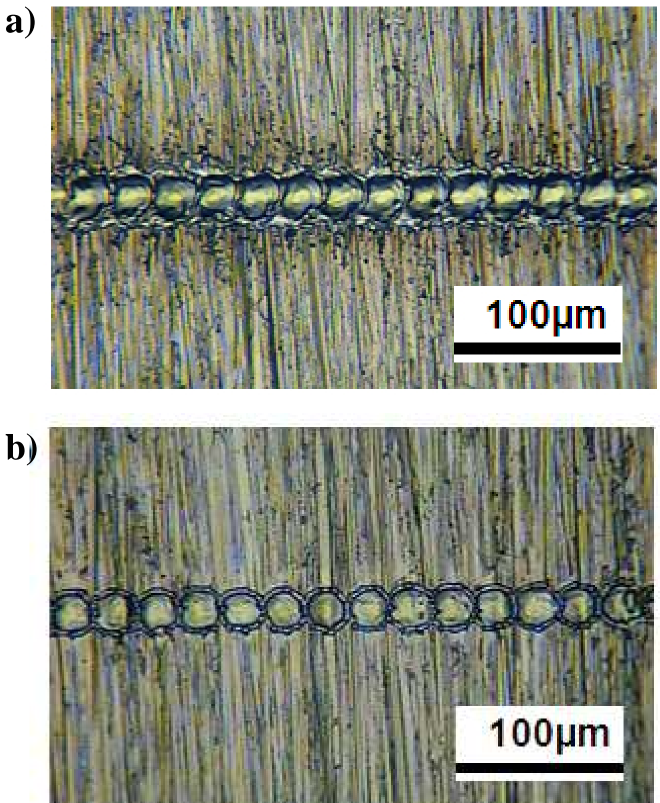

Figure 3.19: Laser marking result on stainless steel operating the laser at a repetition rate of 100 kHz and an average power of 20W whilst scanning the beam from left to right at a speed of 2500 mm/s: a) using optically flat reference mirror; b) using PDM to create the flat top beam shape as shown in Figure 3.18 c).

Both the initial Gaussian beam shape using a flat mirror and the modified square flat top beam shape using the PDM have been applied to laser marking of bulk stainless steel. The work piece was located with the top surface at the focus of the optical system underneath the galvo scanhead (see Figure 3.17). The laser was operated at a repetition rate of 100 kHz and the average power was 20 W. The laser beam was scanned across

the work piece at a speed of 2500 mm/s with the scanhead. At this speed, the laser repetition rate and spot size of individual laser pulses provide only a very small overlap between consecutive laser pulses on the surface of the work piece. The laser machining results are shown in Figure 3.19: For the unmodified Gaussian beam shape (Figure 3.19 a) the area affected by melt and particulates, i.e. re-solidified melt and possibly condensed material, is significantly larger than for the square flat top intensity distribution (Figure 3.19 b), whilst all other process parameters are the same. The high peak intensity at the centre of the Gaussian beam is most likely causing some vaporisation in the centre of the laser mark which is driving the melt out further and is resulting in spatter, whereas the square flat top intensity distribution with a much lower peak intensity is causing more uniform melting and little or no vaporisation. The marks in Figure 3.19 b) have a slightly square shape as expected due to the laser beam shape.

3.5.3 Conclusion

This initial laser machining experiment clearly reveals that modifying the beam shape, whilst all other laser parameters remain the same, has a strong impact on the achievable quality of laser generated markings. The benefit of converting a Gaussian beam shape to a top hat profile was demonstrated for marking stainless steel with a ns laser machining workstation. The resulting laser marks for the square flat top beam shape exhibit a smaller area with deposited material than the marks made with the Gaussian beam despite the modified laser beam diameter being slightly larger. The high intensity at the centre of the Gaussian beam results in an increased melt ejection which is in marked contrast to the uniform flat top intensity distribution with lower peak intensity. However, further work is required to investigate this particular machining process and the melt ejection mechanisms forming the spatter for the Gaussian intensity distribution.

3.6 Application of piezoelectric deformable mirror to millisecond laser machining

This section including the subsections presents collaborative work carried out with Dr Jonathan Parry. For the work described so far in this chapter, the piezoelectric deformable mirror (PDM) was applied to laser system with a good beam quality (M^2 ~ 1.3 to 1.4), i.e. where the initial beam had a Gaussian intensity distribution or at least a close approximation towards the Gaussian shape. For the experiments described later in this section using a millisecond (ms) pulsed laser the output beam is multimode and the

beam quality product M^2 is significantly worse at ~10 (see Figure 3.21). Nevertheless, the PDM was applied in order to alter the beam shape towards custom designed target profiles controlled closed-loop using the SA. The beam shape was optimised towards a circular flat top and a doughnut profile and those shapes were used to drill holes in 3 mm thick steel. Adaptive beam shaping enables both an improvement in the intensity distribution and also the drilling results as presented below.

3.6.1 Setup

The laser used in for this experiment is a JK Lasers JK705 with a fundamental wavelength of 1064 nm. It is a neodymium-doped yttrium aluminium garnet (Nd:YAG) laser, pumped using xenon filled flashlamps. For the experiments described here, the laser was operated at a repetition rate of 6 Hz with a pulse length of 1 ms and a pulse energy of 8 Joules (measured using the internal power meter). The beam quality product M^2 is ~10. The beam diameter from the laser was expanded to approximately 22 mm by adjusting an internal beam expanding telescope of the laser unit. The laser beam was incident onto the deformable mirror at an angle of ~5° to the surface normal (see setup in Figure 3.20). Using a 45° turning mirror it was directed into the machining head which includes a 120 mm focal length lens, a protective cover slip, and a co-axial gas nozzle. The distance between the PDM and the machining lens was 1.3 m. Compressed air at a pressure of 4 bar was used as an assist gas to protect to the enclosed optics. The surface of the work piece was located at focus of the optical system and the distance between the gas nozzle and the work piece was 2 mm.

A beam splitter was located between the PDM and the machining head to use a small part of the light for the closed-loop optimisation of the PDM. The laser beam is focussed onto a CCD camera with a 1000 mm focal length lens which is located at a distance of 1 m away from the deformable mirror. This results in an image of the beam profile being around 8.3 times larger than the beam diameter at the focus of the machining head.

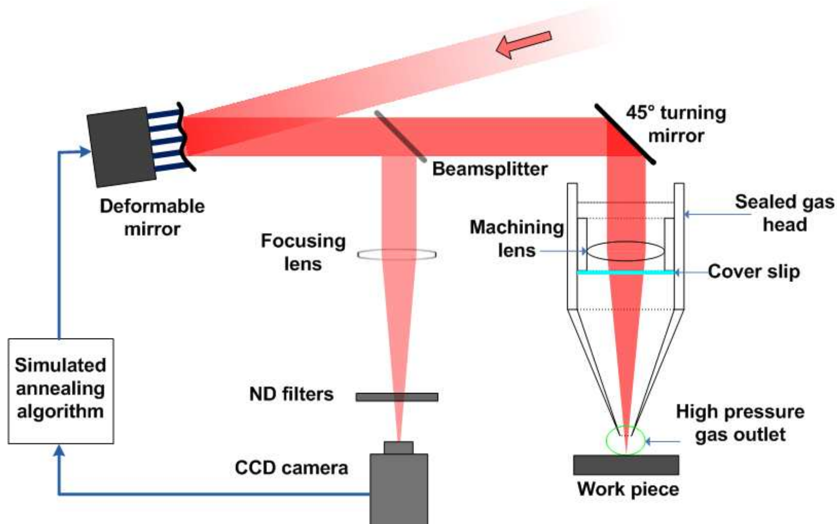

Figure 3.20: Experimental setup of PDM embedded into ms laser machining workstation. Machining lens: f=120 mm, diameter=20 mm, Focusing lens: f=1000 mm, diameter=25.4 mm.

3.6.2 Beam shaping results

Initially, an optically flat reference mirror was used in the setup described above and shown in Figure 3.20 instead of the PDM. The initial and unmodified beam shape of the ms laser system is shown in Figure 3.21. Each pixel of this normalized intensity distribution corresponds to a pixel size of 7.4 µm of the monochrome CCD camera. The initial beam shape exhibits an uneven intensity distribution with an overall diameter of approximately 740 µm (4σ diameter). This corresponds to a beam diameter of around 90 µm at the focus of the machining head due to the different lenses applied for imaging and machining.

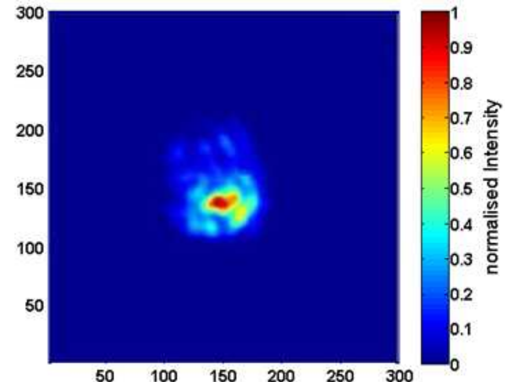

Figure 3.21: Initial beam profile of millisecond (ms) laser using flat reference mirror (1 pixel = 7.4 µm).

After integrating the PDM into the setup, beam shaping was carried out using the SA (see section 3.2). Due to mechanical vibrations and the long optical path length the position of the beam on the CCD camera fluctuates slightly. In order to compensate for this, the "centre of mass" of the beam profile is determined before calculating the root mean square error between the measured intensity distribution and the desired target profile. At the beginning of the optimisation the deformable mirror was set close to optically flat based on a previous measurement with the phase stepping interferometer (see section 3.1.3.1). The optimisation has been carried out towards a circular flat top profile with a target diameter of 100 pixels which corresponds to 740 µm on the CCD camera (see Figure 3.22 a). The normalised beam shaping result after 2500 iterations is shown in Figure 3.22 b. The uniformity of the intensity distribution is significantly improved compared to the unmodified beam shape shown above in Figure 3.21.

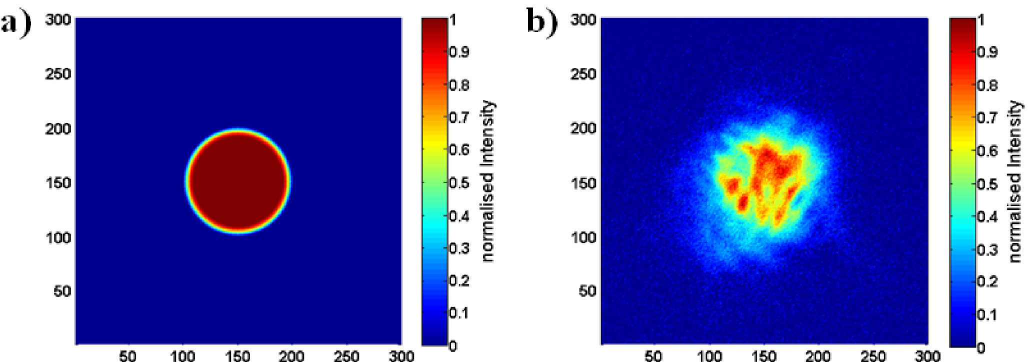

Figure 3.22: Beam shaping towards circular flat top profile: a) target profile with 100 pixels diameter; b) beam shaping result after 2500 iterations (1 pixel = 7.4 µm).

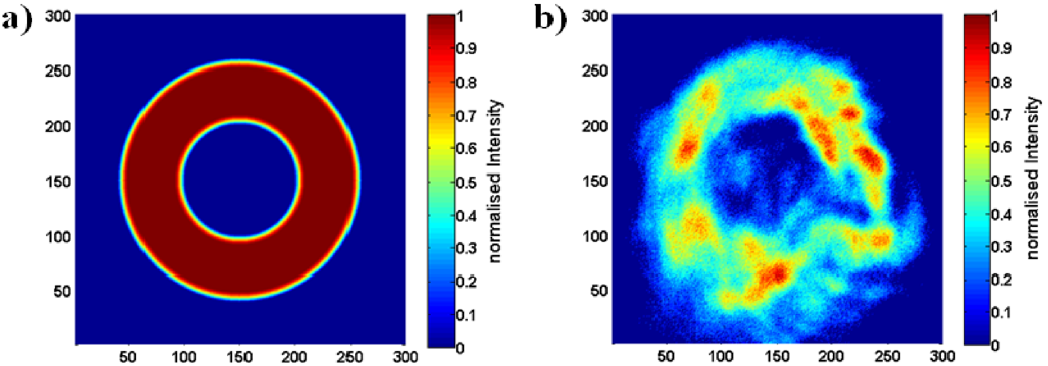

Figure 3.23: Beam shaping towards doughnut profile: a) target profile; b) beam shaping result after 2500 iterations (1 pixel = 7.4 µm).

In the next step, an optimisation towards a doughnut shape or ring focus was carried out. Unlike the previous case with the flat top profile, the deformable mirror was not nominally flat at the start of the optimisations. Based on measurements of the surface profile with the phase stepping interferometer the voltages of the central 7 actuators have been altered corresponding to a phase delay of π rad for the central area as recommended by [94, 154]. Based on the resulting beam shape and the dimensions of the unmodified beam, a ring shape with an outer diameter of 200 pixels and an inner diameter of 100 pixels was chosen as target profile (Figure 3.23 a). The beam shaping result (Figure 3.23 b) gives a slightly uneven intensity distribution although the beam profile is clearly ring shaped, showing a low intensity region at the centre of the beam. The doughnut shape has an outer diameter of approximately 240 pixels (i.e. 1800 µm) and an inner diameter of approximately 100 pixels (i.e. 740 µm). This relates to 210 µm outer and 90 µm inner diameters at the focus of the machining head.

3.6.3 Laser machining results

Using the unmodified beam shape based on the optically flat reference mirror, and both the circular flat top and the doughnut beams generated by the piezoelectric deformable mirror, holes were drilled into 3 mm thick steel at normal incidence. For each beam profile identical laser parameters, i.e. 8 Hz repetition rate, 1 ms pulse length and 8 J pulse energy, were used. The top surface of the work-piece was placed at focus with a standoff from the gas nozzle of 2 mm. The cross sections of the single laser pulse drilled holes are shown in Figure 3.24. Both the unmodified and the circular flat top beam profiles did not consistently penetrate the full thickness of the steel. However, the doughnut profile did penetrate across the full 3 mm thickness in all cases. The hole drilled with the unmodified beam is somewhat uneven and deviates slightly to one side. The deviation may result from the uneven and off-centre intensity distribution as shown in Figure 3.21; however such a shape is not atypical for a multimode beam. The hole arising from the top hat profile has an even shallower depth although it is of a more uniform shape. The slightly bulbous profile of the cross-section towards the bottom of the hole indicates that the melt expulsion from the hole is becoming less efficient. The holes drilled using the doughnut profile, meanwhile, consistently penetrate through the full thickness of the sample. The resulting hole diameter is much narrower compared to the previously used beam shapes. This indicates that the doughnut beam shape is

conducive to a more efficient drilling process which is likely to be caused by a more effective melt eject mechanism.

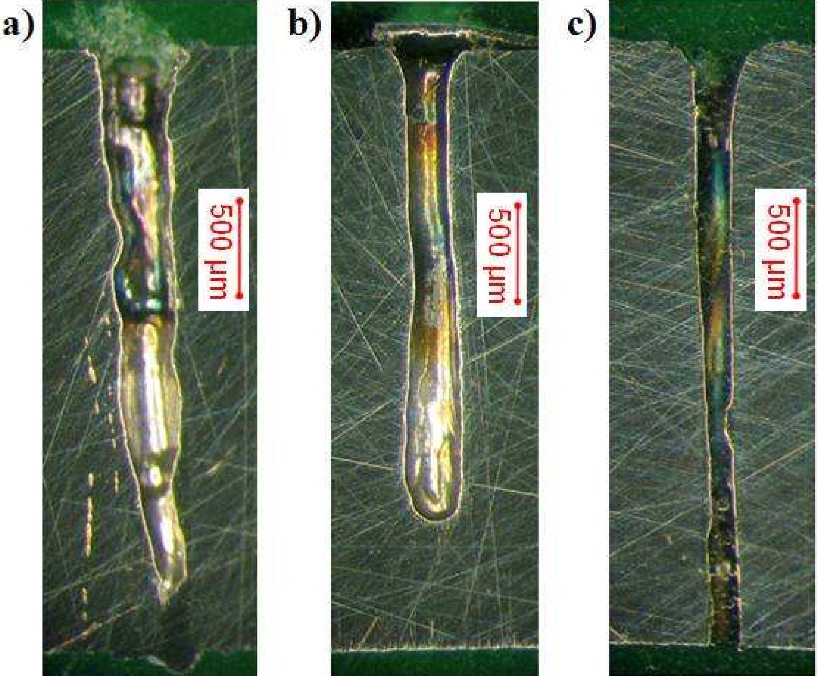

Figure 3.24: Cross section of holes drilled with a single laser pulse into 3 mm thick steel with a) unmodified, b) circular flat top and c) doughnut beam profile.

For drilling with two consecutive pulses the unmodified and the flat top beam profiles penetrated the full thickness of the 3 mm thick sample in some cases, however not consistently. This implies that there is some random element associated with this type of drilling process. In order to achieve consistent through-holes with these beam shapes three pulses were required and example cross sections of the holes are shown in Figure 3.25. The hole diameters were measured at the top and bottom surfaces for 10 holes of each beam profiles the average values are shown in Table 3-2. For the case of the unmodified beam (Figure 3.25 a) the uneven shape of the hole has been smoothed out by the additional pulses compared to the previous result. As result, the hole is roughly constant in diameter for its entire depth. The through-hole drilled using the top hat profile (Figure 3.25 b) exhibits a conical shape and is slightly flared towards the bottom. This is consistent with the slightly bulbous shape of the cross section resulting from a single pulse (Figure 3.24 b). As the expulsion of melt becomes less efficient the drilling rate becomes slower. Hence this gives more time for heat to propagate and melt material at a greater radius. The hole drilled with the doughnut profile (Figure 3.25 c) shows a very similar shape to that drilled with a single pulse (Figure 3.24 c) except for a

slightly wider diameter, particularly at the top. Considering that a consistent through hole already results from a single pulse, this is not surprising.

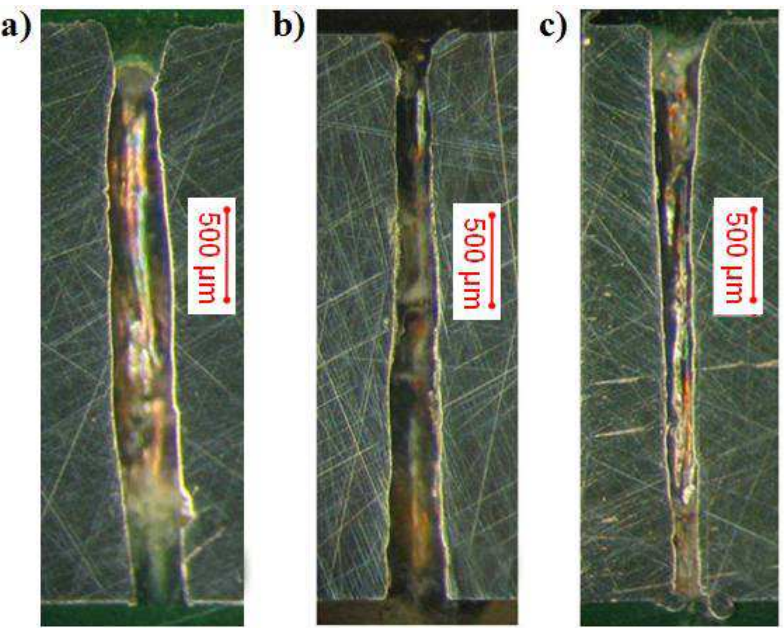

Figure 3.25: Cross section of holes with three pulses into 3 mm thick steel with a) unmodified, b) circular flat top and c) doughnut beam profile.

	Unmodified beam	Circular flat top	Doughnut profile
Beam diameter on CCD:	~740 µm	~740 µm	~1800 & ~740 µm
Corresponding beam diameter at focus of machining head:	~90 µm	~90 µm	~210 & ~90 µm
Hole diameter at top surface of work piece:	~450 µm	~360 µm	~340 µm
Hole diameter at bottom surface of work piece:	~350 µm	~340 µm	~230 µm

Table 3-2: Overview of beam diameters and resulting hole diameters for drilling with three pulses (average of 10 measurements)

3.6.4 Discussion and conclusion

The diameters of the laser drilled holes vary significantly for the different spatial intensity distributions. For an unmodified multimode beam incident on the surface the resultant holes have a diameter which is more than a factor of 7 larger than the actual beam diameter, and similarly for a flat top beam profile this factor is 6. This is normal

for a ms process where the material is removed by a mixture of vaporisation and thermal melt-eject mechanism. The energy from the laser pulse is absorbed as heat and conducted a significant distance into the material over the duration of the pulse (see [14]). In marked contrast, holes produced with the doughnut profile are a factor of only 2.5 larger than the outer diameter of the incident beam. This means that the doughnut beam, which has the largest diameter of the three different beam shapes actually produced the smallest diameter holes. Furthermore, the doughnut beam profile results in the largest penetration depth for single pulse drilling indicating a much more efficient drilling and melt removal process. Further experiments are required in this context to determine whether the benefits of using a doughnut shape are purely caused by the modified intensity distribution or also by a potential change of the focus position and the depth of focus.

The beam shaping result for the optimisation towards a top hat profile exhibits a much more uniform intensity distribution compared to the unmodified beam with approximately the same overall diameter of 90 μm at the work piece. The slightly bulbous or flared nature of the holes produced along with the reduced penetration depth achieved for the single pulse hole indicate a slightly less efficient material removal mechanism compared to the initial and unmodified beam shape. The unmodified and non-uniform beam has a higher local intensity and thus potentially generates a higher local pressure of the molten material at the bottom of the hole. This causes the melt to be ejected at a faster rate. There is a trade-off between uniformity of the hole shape and depth when comparing the unmodified and the top hat beam shape.

Although the beam shaping capabilities of the PDM are limited by the small number of active elements and the stiffness of the reflective surface, beam shapes can be produced that have a significant and beneficial impact on the outcome of the laser machining. Even though flat top or doughnut beam shapes could be generated by other static optical components the dynamic nature of the deformable mirror provides the possibility of modifying the beam shape on-line with changes in the incident beam profile potentially arising from variations in laser parameters. In addition, the rapid response time of the device (~1 kHz), compared to the slow repetition rate of the ms laser enables the beam shape to be changed between pulses. As an example, a doughnut profile could be used to generate a through-hole with the first pulse and the successive pulse could be altered towards a top hat beam profile in order to expand the hole diameter. It should be noted

however, that the inherent hysteresis of the PDM of 10% potentially affects the reproducibility of these shapes and hence a resetting of the actuator voltages to zero is required prior to the addressing of a new set of actuator voltages.

In conclusion, the PDM has enabled adaptive beam shaping of a ms pulsed laser. The multimode intensity distribution can be altered and optimised towards a more homogeneous intensity distribution. It has been shown that by controlling the spatial intensity distribution, the ability to drill deep, high aspect ratio holes can be significantly improved. The doughnut beam profile in particular resulted in a significantly improved drill depth and a smaller hole diameter in comparison with the unmodified beam profile. This device has the capability to compensate for changes in the beam profile caused by changing laser parameters and to respond quickly enough to change the beam shape between pulses.

3.7 Summary

Extracavity laser beam shaping using two different types of deformable mirrors, i.e. a piezoelectric deformable mirror (PDM) and a bimorph mirror (BM), and closed-loop control by means of a stochastic simulated annealing algorithm has been demonstrated. Both devices are capable of supporting sufficient laser powers with regards to laser materials processing using ns and ms lasers. However, the small number of active elements, the crosstalk between adjacent actuators and the stiffness of the reflective surface are the limiting factor for the beam shaping capabilities of the BM and the PDM.

The circular symmetry of the electrode pattern of the BM is particularly suitable for optimisations towards elliptical beam shapes with a potential application to laser dicing.

Benefits when altering the initial Gaussian beam shape towards a square flat top profile using the PDM have been demonstrated for ns surface marking. For laser drilling with a multimode ms laser, creating a doughnut beam profile by means of the PDM has been demonstrated to significantly improve the quality of the drilled holes.

Chapter 4

Experimental results using spatial light modulators (SLM)

This chapter describes the application of several different liquid crystal on silicon spatial light modulators (SLMs) for beam shaping in laser micromachining. SLMs based on liquid crystal microdisplays are powerful devices for beam shaping due to their very high spatial resolution, their direct programmability, and their speed. Consequently, they been applied to a variety of applications such as programmable lenses [112], optical tweezers [122, 123, 155] or adaptive optics [156]. Further applications are described in section 2.3.4. Yet, in comparison to deformable mirrors SLMs have a marked disadvantage as they are only able to handle a significantly lower average power optical density. The power handling capabilities of the SLM LC-R 2500 are stated by the manufacturer Holoeye to be 1-2 W/cm^2 limiting the total average power to about 3 W. However, for the majority of standard nanosecond laser machining processes somewhat higher laser powers are required. As a result, research into the application of this SLM for micromachining of metals, polymers and silicon has been limited to femtosecond (fs) [9, 10, 23] and picosecond (ps) [11] laser pulses. In all these cases the average powers used were relatively low, although they demonstrate that the display can cope with very high peak powers. In industry, nanosecond pulsed laser machining is much more common, a significant driver for the work presented in this chapter particularly if SLMs are to be considered for development of practical laser machining applications.

The major part of the work described in this chapter uses the SLM LC-R 2500 manufactured by Holoeye. This is a conventional liquid crystal device originally developed for visual applications. In order to enable the application of this device to high average power laser machining several modifications are explained and discussed in sections 4.1.2 - 4.1.5. Example laser machining with complex beam shapes is presented in 4.1.6. Potential limitations of the performance due to the electronic addressing of the device are analysed in section 4.1.7 and a process synchronisation technique to overcome this issue is presented in section 4.1.8. The dynamic nature of the SLM can be used to overcome the inherent and adverse impact of speckle and the spread of heat, and to improve the quality of laser marking (section 4.1.9 - 4.1.10). The

work described in sections 4.1.9, 4.1.10 and 4.4.3 was carried out in collaboration with Dr Jonathan Parry, but based on fundamental findings and previous results by the author as described in sections 4.1.2 – 4.1.8. The results were published in a joint paper (see 2) below). Using adaptive feedback in combination with a modified iterative Fourier transform algorithm (MIFTA) results in a further improvement of the quality of the laser machining and results are presented in section 4.1.11.

Besides the conventional liquid crystal display as used in the LC-R 2500, two other SLMs have been investigated which were developed in particular for laser beam shaping:
The X10468-04 SLM from Hamamatsu is analysed in section 4.2 in terms of response and an example of laser machining using this device is demonstrated. The process synchronisation technique is applied to improve the laser marking result for changes in the beam shape during the laser machining process (section 4.2.3).
The device A512-0532 from Boulder Nonlinear Systems was tested in section 4.3. This unit has the fastest response of any commercially available liquid crystal device to date.

The chapter concludes with a summary comparing the three different devices in terms of efficiency and response and finally, the suitability of the different SLM devices for beam control of nanosecond pulsed high power lasers is discussed.

The results described in this chapter were published in the following journal articles:

1) R. J. Beck, J. P. Parry, J. D. Shephard, and D. P. Hand: “Compensation for time fluctuations of phase modulation in a liquid-crystal-on-silicon display by process synchronization in laser materials processing”, Applied Optics 50(18), 2899–2905 (2011).
2) J. P. Parry, R. J. Beck, J. D. Shephard, and D. P. Hand: “Application of a liquid crystal spatial light modulator to laser marking”, Applied Optics 50(12), 1779-1785 (2011).
3) R. J. Beck, J. P. Parry, W. N. MacPherson, A. Waddie, N. J. Weston, J. D. Shephard, and D. P. Hand: "Application of cooled spatial light modulator for high power nanosecond laser micromachining", Optics Express 18, 17059-17065 (2010).

4.1 LC-R2500 from Holoeye

4.1.1 Device

The spatial light modulator LC-R 2500 [157] from Holoeye operates in reflection and has a resolution of 1024 x 768 pixels in a dimension of 19.5 x 14.6 mm (Figure 4.1). The maximum image frame rate is 75 Hz with 256 available grey values for each pixel. According to the manufacturer, the pixel pitch is 19 µm and the fill factor is >93%. The display itself is produced by Philips (model X97c3A0 [100]) and contains 45° twisted nematic liquid crystals (see section 2.3.4). The device is addressed via a DVI interface as an extended screen directly from the graphics card (8-bit driver for the 256 grey levels). Considering a look-up table (LUT) this signal is transformed to a 9-bit signal for controlling the voltage across the liquid crystal layer. The display provides a phase change of at least 2π rad in the visible spectrum between 400 and 700 nm. At the fundamental wavelength of our ns laser system, 1064 nm, the maximum phase change is just ~1.3π rad [158]. Below a wavelength of 400 nm the liquid crystal layer becomes absorbing [159]; thus the third harmonic frequency of the laser at a wavelength of 355 nm is not suitable for modulation with this device. As a result, the second harmonic frequency of the laser system at a wavelength of 532 nm was chosen to be modulated by means of the SLM. According to Holoeye the maximum recommended average laser power is 1-2 W/cm^2. This limits the total average power to around 3 W assuming a circular laser beam with a diameter of 14 mm at normal incidence on the display. However, for the majority of standard nanosecond laser machining processes somewhat higher laser average powers are required.

Figure 4.1: Control unit and display of SLM LC-R 2500 from Holoeye

4.1.2 Curvature of display and copper mount

As mentioned before, the SLM display can cope with the high laser peak powers in the fs and ps regime where the average powers required are relatively low, demonstrating that the much higher peak intensities in the ultrafast regime did not cause damage to the display. However, a fraction of the incident laser power is absorbed in the liquid crystal material and the interface layers and this absorbed energy can, over time, adversely affect the phase response of the display and furthermore potentially damage the liquid crystals, the alignment layer of the liquid crystals or the electronic driving circuitry. The display itself is manufactured by Philips, model X97c3A0, and is stated to have a reflectivity of ~75% at a 12.5° angle of incidence and an ambient temperature of 25 °C [100]. The SLM operates in reflection and has a metal plate at the back of the display. This makes it straight forward to introduce heat sinking to remove the heat due to the absorbed and non-reflected light. A copper mount was designed to act as a heat sink with additional optional additional water cooling (see Figure 4.2). Good thermal conductivity between the metal plate at the back of the SLM display and the copper mount was attained by grinding and polishing the copper surface close to optical flatness. The metal plate at the back of the SLM display is not polished. No further reduction of the surface roughness was possible due to the plastic housing covering the metal plate at the corners of the display. However, this was alleviated by applying a slide of Liquid Metal™ [160] from Coollaboratory (often used in CPU cooling units) between the display and the copper block.

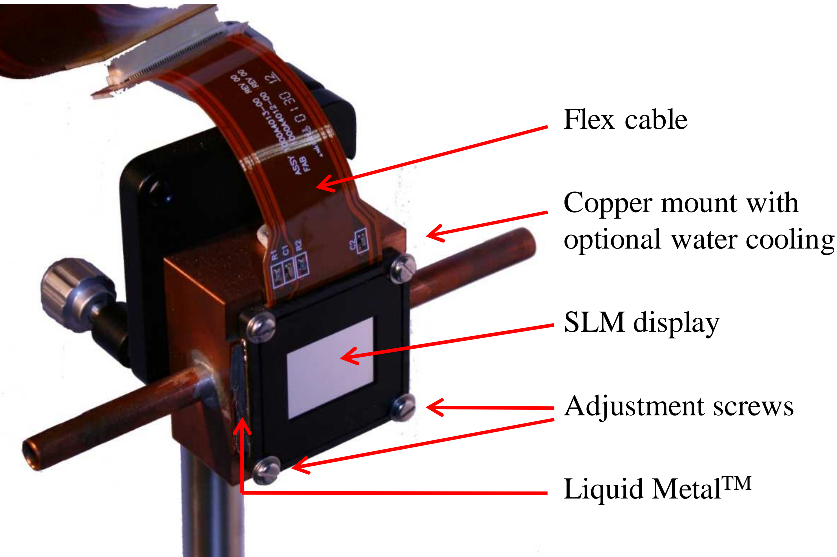

Figure 4.2: SLM display attached to copper mount with optional water cooling.

The display of the SLM exhibits an intrinsic curvature causing optical aberrations of the beam. The manufacturing process of the silicon backplane including the driving circuitry is based on standard CMOS processes (see [123]) which are not optimised for high optical flatness. This is a well known problem for this type of device. In [123] a Fresnel lens phase map is successfully applied to the SLM in order to compensate for the curvature and a similar approach would be beneficial here. The desired phase profile must be superimposed onto this compensation pattern with periodic boundary conditions between the grey values of the SLM corresponding to a phase change of 2π. Figure 4.3 a) shows the initial surface height map of the SLM display obtained using phase-stepping interferometry as described in section 3.1.3.1, but with a frequency-doubled Nd:YAG laser source operating at a wavelength of 532 nm. The display was attached to the mount supplied by the manufacturer and was switched off during the measurement. Since the display is relatively thin and quite flexible, the curvature varied significantly even for small changes in the way it is mounted. Furthermore, significant changes in the display shape using this mount were observed over a timescale of weeks requiring further measurements of the surface shape in order to determine a compensational Fresnel lens. These changes were most probably introduced by temperature variation in the laboratory. In general, the manufacturer supplied mount does not seem appropriate and suitable for the intended application.

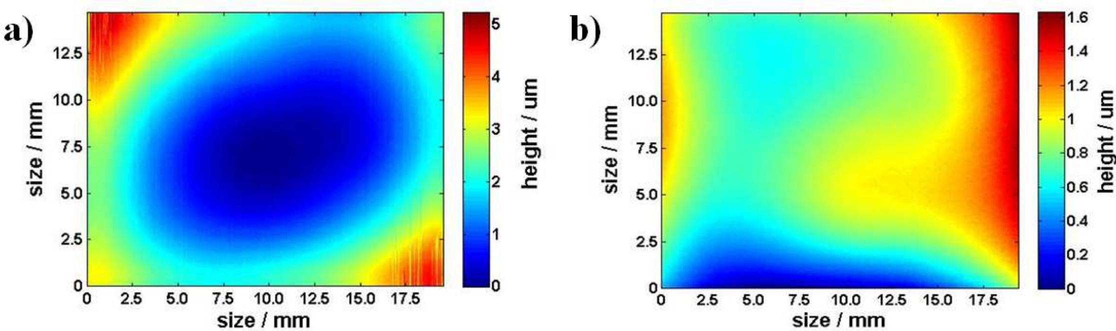

Figure 4.3: Curvature of SLM display: a) initially; b) after mounting onto copper mount; both height profiles determined experimentally using 5-step phase-stepping interferometry (small phase noise can result in vertical lines due to spatial phase unwrapping)

In all further experiments, the display was attached to the custom designed copper mount having a polished and flat surface profile as described earlier. The display is mounted to the copper block using four screws located at the corners of the housing of the display (see Figure 4.2). By adjusting these screws carefully and monitoring the shape of the display by means of the phase-stepping interferometer it was possible to

eliminate most of the unevenness of the device (see Figure 4.3 b). Based on the height data of the remaining surface deformation, a wrapped phase map could be calculated and when sent to the SLM this would compensate for the small remaining residual distortion. However, our application uses a circular beam with a diameter of 14 mm, incident on the central region of the "flattened" display, and the mounting method resulted in an optical flatness sufficient for our needs over this region without compensation. The root mean square deviation of this area was reduced by a factor of 3 using the copper mount compared to the previous case.

4.1.3 Calibration of phase response

Due to the strain introduced by the four adjustment screws, the relationship between the numerical value sent to a pixel and the resulting phase change needs to be recalibrated in order to ensure a linear response for the phase modulation between 0 and 2π. The 8-bit signal from graphics card, defining the grey value of each pixel, is translated into a 9-bit signal by means of a look-up table (LUT) for gamma correction. The LUT of the SLM determines the relationship between addressed grey value and the resulting electric field across the liquid crystal.

The calibration of the response of the SLM display is carried out based on phase shift interferometry as described in [161]. An imaging Michelson interferometer arrangement (see Figure 4.4) is used with a low power frequency doubled Nd:YAG laser source having a wavelength of 532 nm. This corresponds to wavelength of the laser machining workstation. A polarising beam splitter is added to the setup to generate linearly polarised light. The orientation of the polarisation direction is controlled using a half wave plate. The light is incident on the SLM display at an angle of 20° (rotation in mathematically positive direction, see Figure 4.5) to the short axis of the display resulting of a phase-mostly operation of the display. Different configurations regarding the polarisation state and angle of the incident light are suggested in the literature in order to achieve a phase-only or phase-mostly configuration of this device (see sections 2.3.4 and 2.3.4.2). These normally use a polarising element as an analyzer after the SLM. Standard nanosecond laser machining applications require a relatively high average power at the work piece. Consequently the system was configured to have linearly polarised light incident on the SLM but no analyzer after the SLM in order to avoid a further loss of laser intensity on the work

piece. As a consequence, the possibility of small deviations from an ideal phase-only operation of the device has to be accepted.

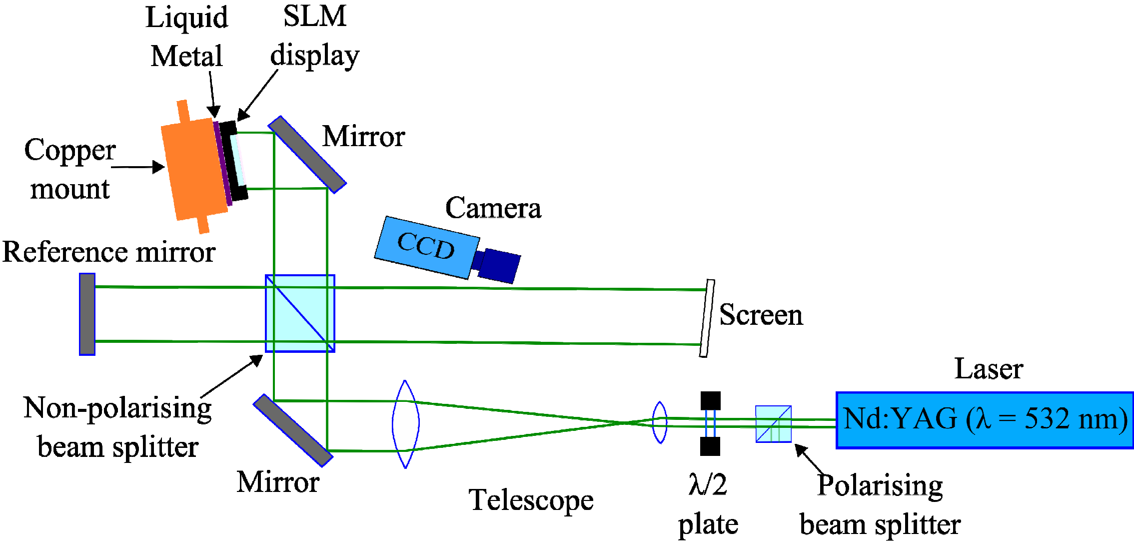

Figure 4.4: Setup for phase calibration of SLM based on Michelson interferometer.

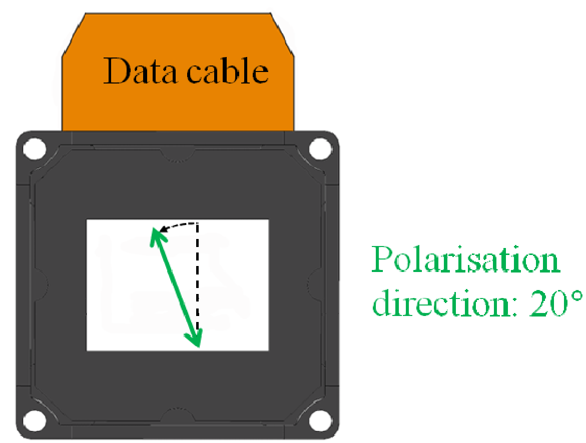

Figure 4.5: Alignment of polarisation direction relative to SLM display (front view).

The laser diameter is expanded by ~37 times using a telescope arrangement, consisting of a 20x magnification microscope objective and an achromatic doublet lens with a focal length of f=300 mm, to illuminate the full size of the SLM display. In contrast to the phase-stepping technique (see section 3.1.3.1), the flat reference mirror in one arm of the interferometer stays fixed for these measurements. Also, the display of the SLM is tilted resulting in a higher number of interference fringes on the screen. The fringe pattern is measured using a monochrome CCD camera in combination with an objective. Initially, the LUT of the SLM is set to a linear trend between the minimum

and the maximum values for the available index values, i.e. 0 to 508. The picture addressed to the SLM is divided into four sections (see Figure 4.6 left column) with two of them remain at a constant grey value (Ref). In the case of these measurements the grey level was set to the maximum index values of 508, i.e. white. The grey value of the second half of the picture is varied between all available grey values (Var). The relative change of the fringe patterns at the interface between the fixed and the alternating grey value is measured (example fringe patterns are shown in Figure 4.6 middle column). The captured intensity image is normalized by a reference image taken with one arm of the Michelson interferometer being blocked to compensate for the impact of the Gaussian intensity distribution of the frequency-doubled Nd:YAG laser source.

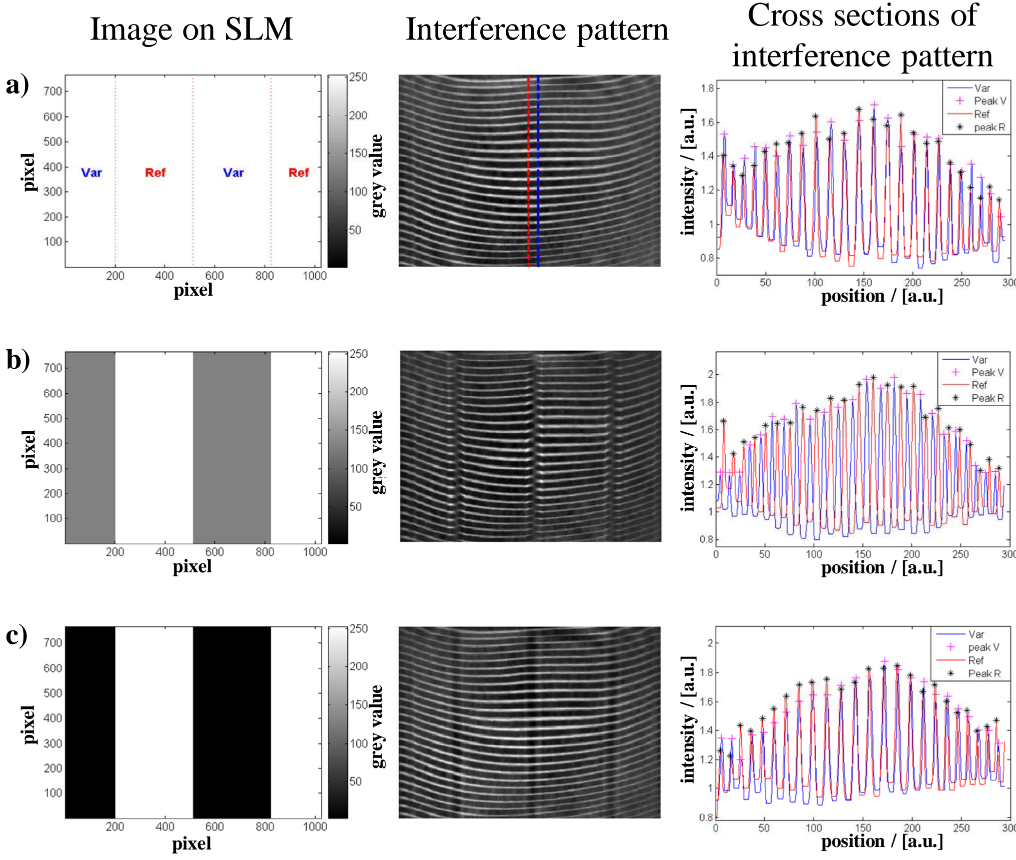

Figure 4.6: Image addressed to SLM divided in sectors with reference grey value (Ref) and varying grey value (Var); resulting interference pattern measured with CCD camera and vertical cross sections (along red and blue line as indicated on interference pattern).

Cross sections close to the interface between the reference and the variable section are obtained in software. To obtain sharply defined peaks of the cross-sections of the interference patterns a two dimensional order-statistic filtering method (ordfilt2) in Matlab is applied with the order of the filter value set to 9, corresponding to a maximum filter, and the domain was 9 by 9 pixels. For the peak detection, an open source Matlab code by Eli Billauer [162] is applied. The resulting response curve for the linear LUT is shown in Figure 4.7. The maximum phase delay is 2.3π rad at a wavelength of 532 nm. The response curve shows two phase jumps of around 0.2π rad for the grey value 60 – 61 and 92 – 93. These grey values correspond to the index values 125 - 127 and 188 - 190 respectively of the LUT. According to the manufacturer these phase jumps are probably due to conversion problem within the electronics when changing the 8-bit signal for the grey value to a 9-bit signal controlling the voltage across the liquid crystal layer [158]. Based on the measured response curve for the linear LUT, a new LUT can be calculated using polynomial fittings for the regions without the jumps in the phase response. A segmented LUT has been calculated which does not include the index values where the phase jump appears (see Figure 4.8). The resulting phase response after the calibration is shown in Figure 4.9. It is close to a linear trend; however, there are deviations especially for grey values between 40 and 60.

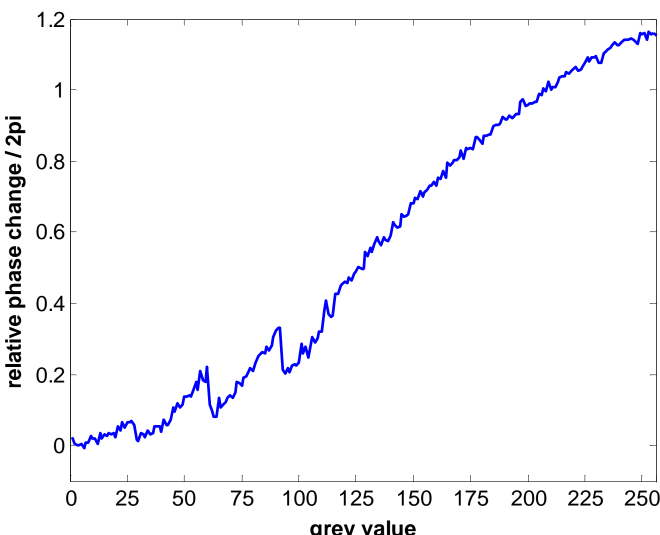

Figure 4.7: Phase response for linear look-up table.

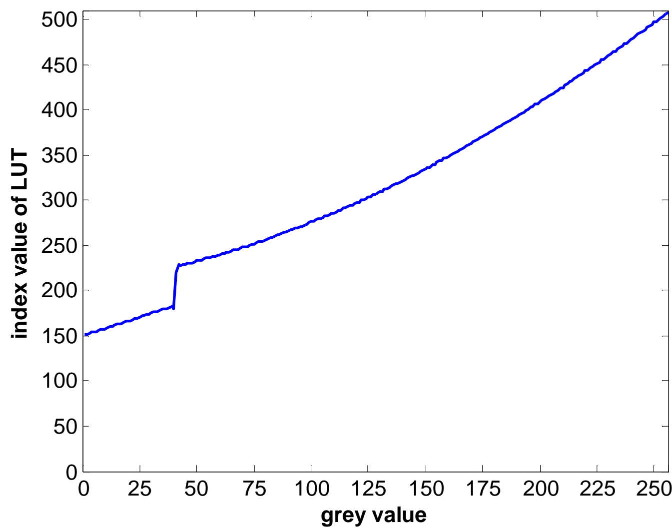

Figure 4.8: Look-up table (LUT) for calibration after mounting display onto copper mount.

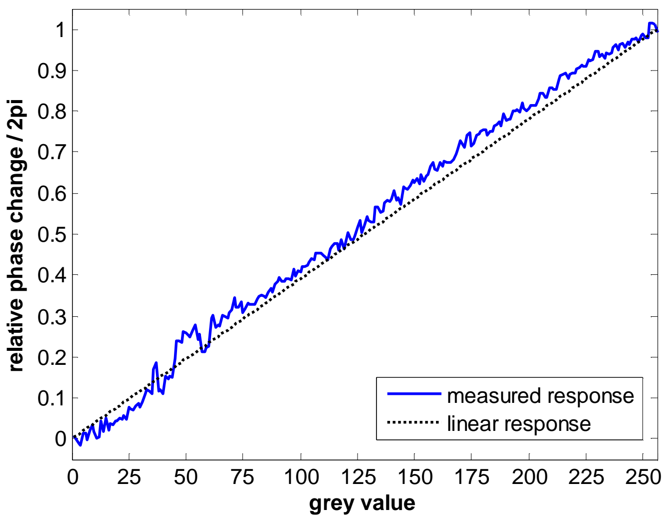

Figure 4.9: Phase response after calibration.

In [161], for a different kind of liquid crystal display, varying responses depending on the position on the display are reported and a local LUT in addition to the global LUT is suggested to overcome this issue. This is the reason that the experiment as described above was repeated for different interfaces on the display (see Figure 4.10 a). However, for the Holoeye LC-R 2500 no significant variations of the response for different locations on the display were observed (Figure 4.10 a), so no additional LUT is required.

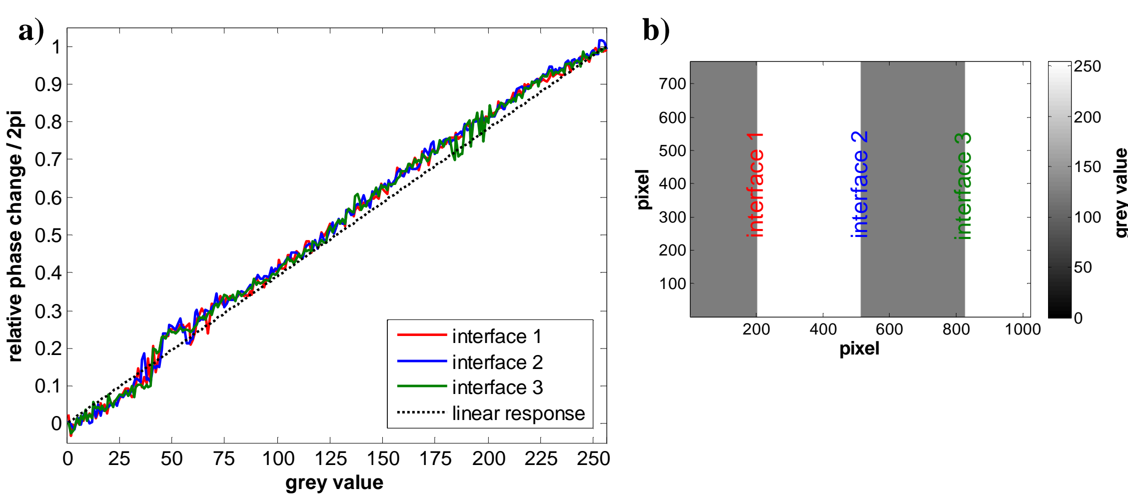

Figure 4.10: a) Phase response after calibration for different interfaces as indicated on b) example phase map addressed to SLM.

4.1.4 Laser machining setup

In order to study the suitability of the SLM for laser based machining techniques, the SLM was embedded into our nanosecond laser machining workstation. The laser is a Nd:YVO_4 system (Spectra-Physics Inazuma) operating at a wavelength of 532 nm with a pulse length of ~65 ns and a repetition rate between 15 and 100 kHz. A half wave plate and a polarising beam splitter are used to attenuate the laser beam intensity and also ensure linear polarised light for the further experiments. The orientation of the linear polarised light incident on the SLM is controlled by an additional half wave plate following the beam splitter. The polarisation state is aligned at an angle of 20° relatively to the short side of the display, as for the calibration in section 4.1.3 (Figure 4.5). The laser beam diameter is increased by means of a telescope arrangement to match the dimensions of the SLM display. The focal lengths of the lenses of the Galilean telescope are f=-9 mm and f=125 mm. The expanded beam diameter ($1/e^2$ value of intensity) is 14 mm. An aperture with a diameter of 14 mm is placed between the telescope and SLM to avoid damage of the display housing by the laser light. This aperture also eliminates potential artefacts arising from beam clipping by the rectangular shape of the display. The incoming laser beam is incident on the SLM at an angle of 10°. After the SLM, a second telescope and the flat field lens (f-theta lens) of the galvanometer (galvo) scanhead are used in a 6-f arrangement to reduce the beam diameter and to focus the laser beam onto the work piece (see Figure 4.11). The telescope was aligned to reduce the beam diameter to 10.5 mm to match the input aperture of the scanhead. The focal lengths of the plano-convex achromatic lenses are

f_1=400 mm and f_2=300 mm for the Keplerian telescope and f_3=115 mm for the f-theta lens (Figure 4.11). All lenses of the setup have a broadband antireflection coating for wavelengths in the visible spectrum.

The SLM is used as a diffractive optical element with computer generated holograms based on the iterative Fourier transform algorithm (IFTA, see section 2.2.3.1). For this approach, the SLM is located at the Fourier plane of a lens and the desired intensity distribution is generated at the focal or image plane of the first lens (2f-plane). At the back focal plane (4-f) of the second lens, the intensity distribution of the beam reverts to its spatial frequency distribution. The final lens in the system is the flat-field lens of the scanhead and at the focus of this lens (6-f) the final image is produced. The scanhead enables the image to be easily positioned or scanned across the work piece.

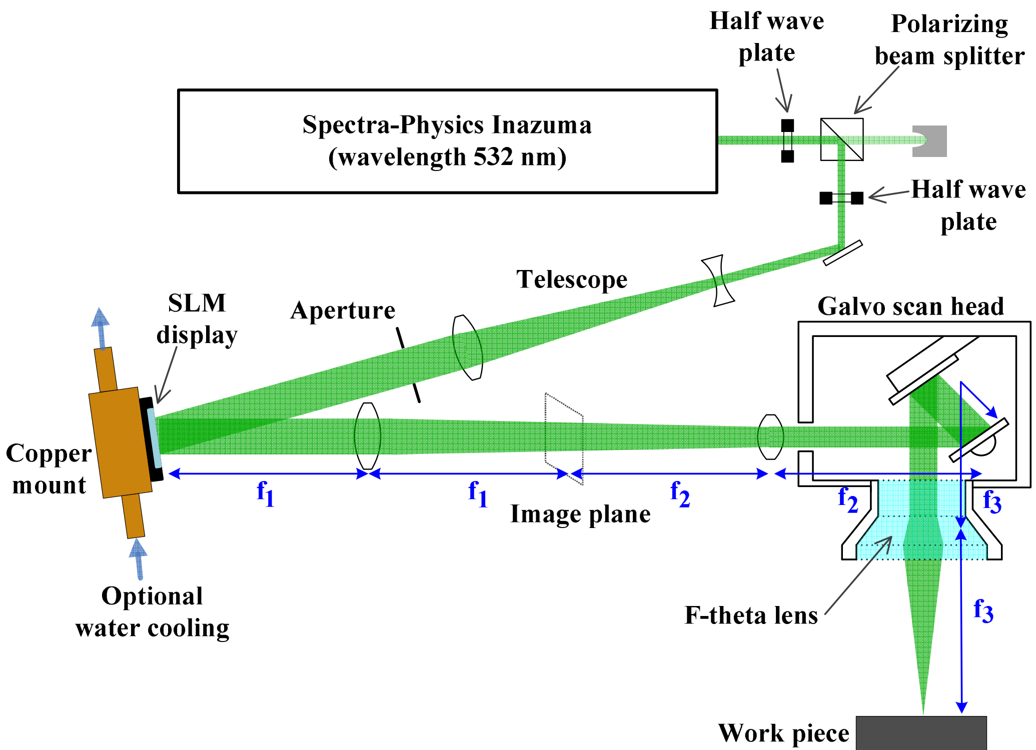

Figure 4.11: Setup for nanosecond (ns) laser machining experiments. Details of the setup are given in the text above.

4.1.5 Damage tests

As stated before, Holoeye recommends a maximum average laser power of 1-2 W/cm^2 for the LC-R 2500. Assuming a circular laser beam with a diameter of 14 mm at normal or close to normal incidence on the display this limits the total average power to

about 3 W. However, the majority of nanosecond laser machining processes require a somewhat higher average power. Successful applications of this device for femtosecond processes as reported by [9, 10] demonstrate that the high peak intensities in the ultrafast regime did not cause damage to the display. However, the absorbed heat over time can adversely affect the response of the display and potentially damage both the liquid crystal layer and the electronic driving circuitry on the silicon layer. The reflectivity of the display in this case is ~75% according to the display manufacturer Philips [100], therefore some incident light is absorbed by the device.

The damage tests have been carried out in consultation with Mr. Stefan Osten from Holoeye Photonics AG. Previous tests according to Holoeye have shown that the diffraction efficiency of the device drops significantly once the laser power is getting too high and the device is getting too hot. In order to avoid permanent damage to the SLM, it is necessary to switch off the laser immediately once a reduction in diffraction efficiency is noticed. After the device has cooled down it can be restarted and provided the deterioration in efficiency has been spotted in time, this is a reversible change and the display does not suffer from permanent damage.

The SLM was incorporated into our nanosecond laser machining workstation as described in section 4.1.4. In the first experiment with the setup shown in Figure 4.11, the laser beam is imaged directly onto a CCD camera. The laser beam is severely attenuated using a beam tap after the focussing lens of the scanhead. In order to monitor the diffraction efficiency of the SLM over time a binary grating with a phase difference of 0.75π rad is addressed constantly to the display resulting in the first diffraction orders and the zero order beam having similar intensities (see illustration in Figure 4.12).

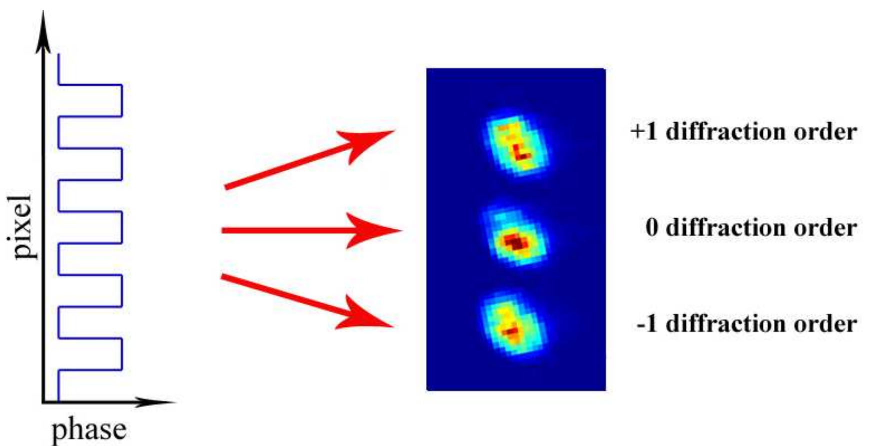

Figure 4.12: Schematic of phase profile of binary grating addressed to SLM and resulting diffraction spots.

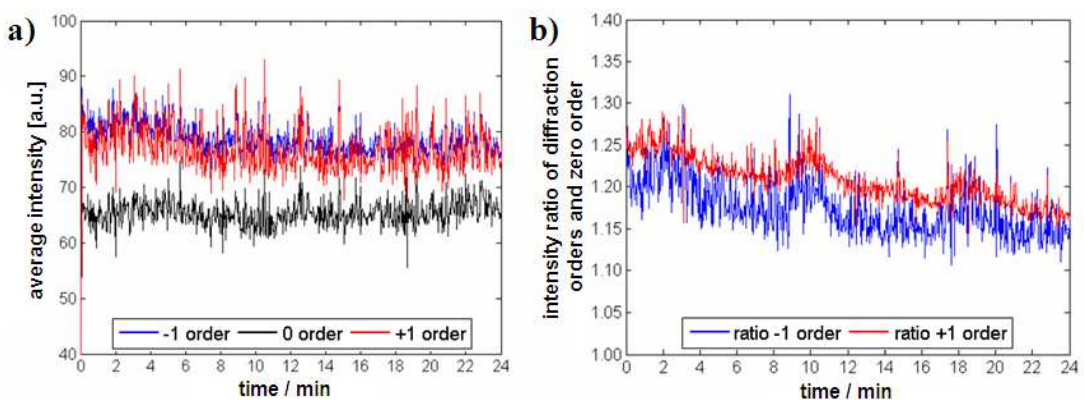

Figure 4.13: a) temporal variation of intensity distribution in zero order (black line) and the first diffraction orders (blue and red line) with 14.7W average power being incident on the SLM display (~65ns pulse length; 30kHz repetition rate); b) intensity in the first diffraction orders divided by intensity of zero order.

For each spot of the zero and the first diffraction orders the average intensity was determined in Matlab and monitored over time for increasing laser powers. For the initial experiments, the copper mount acted as a passive heat sink and no additional water cooling was used. It was demonstrated that the SLM can withstand nanosecond laser pulses of 14.7 W average power at a repetition rate of 30 kHz over a timescale of 24 minutes without significant changes of the zero and first diffraction order intensities (see Figure 4.13 a). The fluctuation of the diffraction efficiency, i.e. intensity ratio between the first diffraction orders and the zero order, over several minutes (as shown in Figure 4.13 b) is associated with variation in ambient air temperature in the lab. This is caused by the air conditioning system switching on and off. The temperature of the front surface of the display, measured using a pyrometer, increased to 48°C during the experiment. The drift of the diffraction efficiency as shown in Figure 4.13 b) from

~1.25 to ~1.15 can be associated to this heating up of the device. The intensity values for the +1 and -1 diffraction orders are slightly different to each other. This is caused by a consistent experimental error due to taking a measurement within a finite size area on the CCD camera. In a further experiment, the display of the SLM was exposed to the maximum average power of our laser, i.e. 14.7 W, over a timescale of 60 minutes without damage to the device and without significant change in the diffraction efficiency. These tests were successfully repeated at a laser repetition rate of 15 kHz and an average power of 11.8 W, i.e. the maximum available pulse energy of the laser system, over a timescale of 24 minutes.

The data shown in Figure 4.13 captured with a standard CCD camera appear fairly noisy despite the binary grating being addressed continuously to the SLM. Indeed, it is the pulse width modulated signal from the control electronics used to drive the pixels of the SLM display which gives rise to these fluctuations as reported by [163] and [164]. These fluctuations and potential disadvantages will be discussed in section 4.1.7.

4.1.6 Example laser machining

The SLM in the optical arrangement described in section 4.1.4 is working as a programmable and dynamic diffractive optical element, and as such can generate a huge range of complex beam shapes. The iterative Fourier transform algorithm (IFTA) [28] or the Gerchberg-Saxton algorithm (GS) [27] are powerful techniques to determine the phase changes required for the beam shaping. IFTA and GS are iterative algorithms to retrieve the phase for two known intensity distributions, i.e. the initial Gaussian beam shape and the desired target beam shape, and the known propagation, i.e. the Fourier transform due to propagation through lens. A more detailed description of both the IFTA and GS can be found in section 2.2.3.1.

For the experiments described here two versions of the IFTA, one supplied by Holoeye with the SLM device and one kindly supplied by Dr. Andrew Waddie from the Diffractive Optics Group at Heriot-Watt University, were used. For the latter software a custom 128 x 128 pixel target profile was used and based on this a 256 x 256 pixel computer generated hologram, also referred to as kinoform, was determined (Figure 4.14 a) and b). This phase distribution was tiled in software on a 3 x 4 pattern resulting in a 768 x 1024 pixel phase map and addressed to the SLM (Figure 4.14 c). A

periodicity of at least 3 for the pattern addressed to the SLM is beneficial for the diffraction efficiency and the uniformity of the resulting intensity distribution [165].

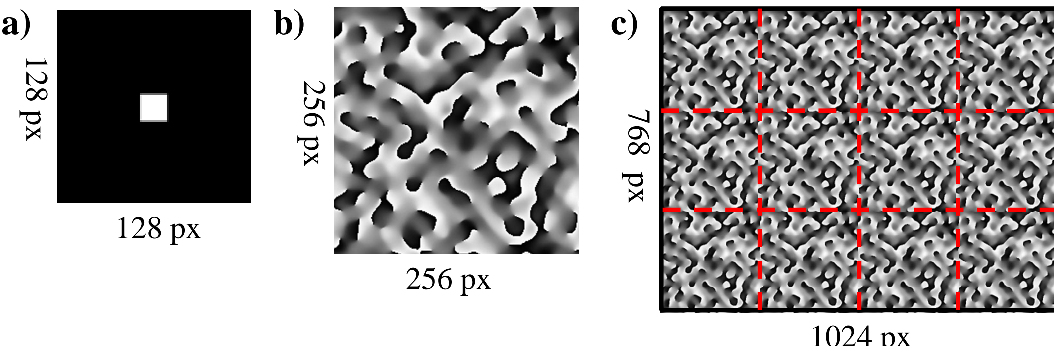

Figure 4.14: a) intensity distribution of target profile for IFTA; b) phase distribution of resulting kinoform; c) phase map with tiled kinoforms in 3x4 pattern for addressing to SLM. Boundaries between kinoforms are indicated with red dashed lines.

These beam shapes can then be used for direct laser machining of arbitrary shapes and patterns without the need for beam scanning equipment. The increased power handling capabilities of this device when mounted onto the copper block enable nanosecond laser machining with complex intensity distributions. As an example a computer generated hologram of a "smiley face" was calculated using an Inverse Fourier Transform Algorithm (IFTA) [28] and addressed to the SLM. Figure 4.15 a) shows the laser machining result (repetition rate 30 kHz, average power 14.7 W, machining time 100 ms) for a laser ablation process of a metal coated glass slide. In terms of industrial relevance, a "smiley face" is arguably not the most relevant beam shape; however, it demonstrated the huge finesse of beam control made possible by the high spatial resolution of the SLM, e.g. compared to the small number of actuators for the deformable mirrors as reported in chapter 3.

The target for the IFTA was set off-axis in order to separate between the intended diffraction pattern and the zero order as seen in the bottom right corner of Figure 4.15 a. The prominence of the zero order is a well known limitation of diffraction holograms [97]. The simplest way to avoid the effects of the zero diffraction order is to produce the diffraction pattern slightly off axis and block off the zero order beam before the target or use spatial filtering. Alternatively, other techniques exist to minimise the impact of the zero order light. One possibility for example is to introduce a divergence such that the zero order gives only background illumination in the image plane, either

by including a physical diverging lens in the system [23], or by calculating a hologram phase map that achieves the same result [155]. Calculating a kinoform to give destructive interference has also been demonstrated as a solution [166].

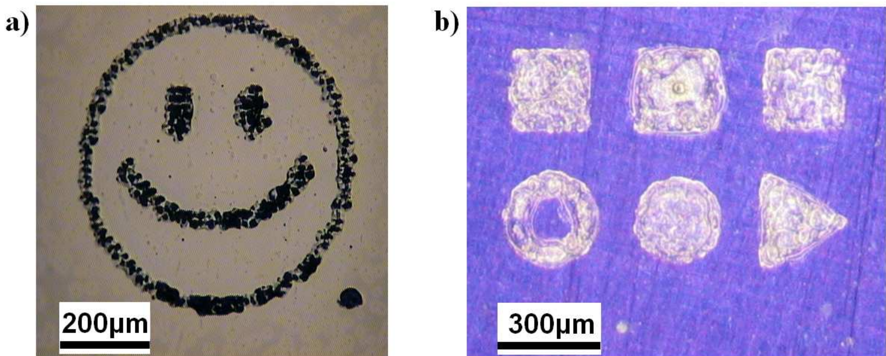

Figure 4.15: Example of laser machining using SLM as DOE: a) laser ablation of metal from a metal coated glass slide using single diffraction pattern addressed to SLM based on Inverse Fourier Transform Algorithm (IFTA); b) laser ablation of polymer (purple) from a polymer coated metal using a sequence of six individual IFTA generated kinoforms. Local positioning is achieved by the kinoform addressed to the SLM rather than a mechanical motion system. The ablated area at the bottom right of a) and the centre of the middle square are due to the inherent zero order beam.

The approach of using the SLM as a diffractive optical element enables both beam shaping and also beam steering as demonstrated in Figure 4.15 b): six individual kinoforms for a circular, a triangular, a doughnut and square target profiles at different locations were generated using the IFTA and laser machined sequentially (repetition rate 30 kHz, average power 14.7 W, machining time 3.2 ms each) as an ablation process on a polymer coated metal. The different positions were achieved by means of the SLM rather than a mechanical beam scanning system according to the optical arrangement shown in Figure 4.16. Based on the IFTA the hologram for the desired target profile was initially generated on axis, as shown in Figure 4.17 a) for the square intensity distribution. This hologram was used to laser ablate the square mark at the top middle of Figure 4.15 b). A strong phase gradient (Figure 4.17 b), wrapped between 0 and 2π, is added to the initial kinoform and then wrapped with periodic boundary conditions between 0 and 2π. The resulting phase profile (Figure 4.17 c) is addressed to the SLM and used to laser machine the square mark at the top left of Figure 4.15 b. Accordingly, the phase profiles for the doughnut, the circular and the triangular intensity distribution were generated on axis and shifted by means of adding phase gradients and wrapping the resulting phase map between 0 and 2π. Time efficient wrapping of the phase map can be achieved for example in Matlab using the ‘floor’-function (see Equation 4-1).

$$phase_{wrapped} = phase_{unwrapped} - 2\pi \cdot floor(\frac{phase_{unwrapped}}{2\pi});$$ **Equation 4-1**

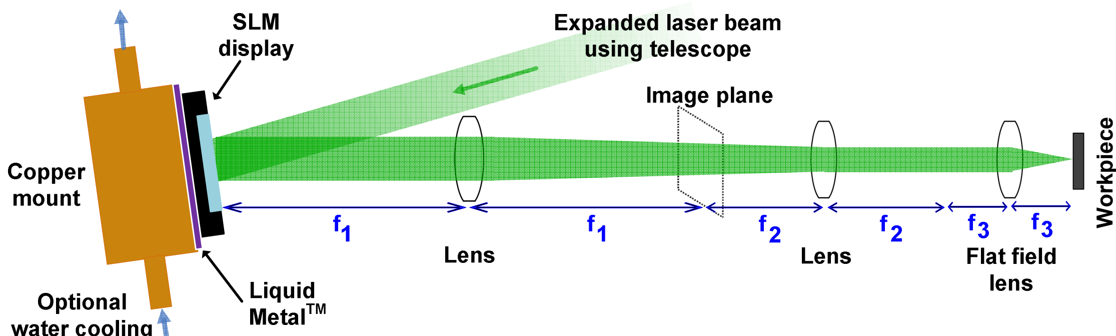

Figure 4.16: Setup for laser machining experiments with SLM used for beam shaping and steering.

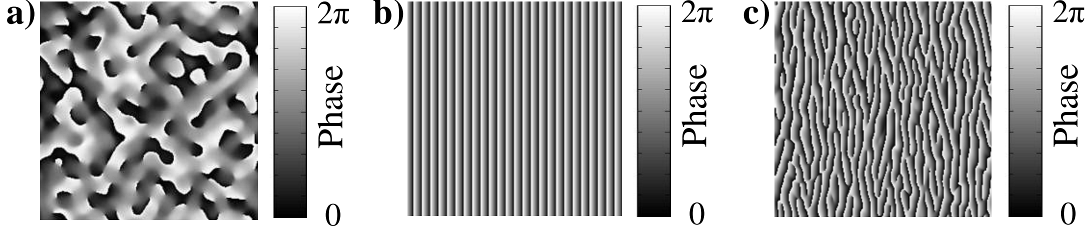

Figure 4.17: Schematic of beam steering: a) initial phase map to generate beam shape for marking sqaure shape in top middle in Figure 4.15 b); b) wrapped phase gradient, c) resulting phase profile when combining a) and b) with periodic boundary conditions to generate beam shape for top left mark in Figure 4.15 b).

The limiting factor regarding the overall process time in this context is not the computational time for adding a phase gradient and wrapping, but the refresh rate of the SLM which is 75Hz in this case. However, for laser machining applications requiring a comparatively small and slow movement of the laser beam or the beam shape relative to the work piece, the beam steering capabilities of the SLM may be sufficient and no additional motion system, e.g. a galvo scanhead, may be required. With prices for SLMs and scanhead systems typically being around £10k this may well be worth considering.

There is a strong mark at the centre of the top middle square of Figure 4.15 b) caused by the zero order beam, which could be removed as mentioned above if required. Both laser machining results suffer from some speckle, e.g. a speckle may be around 1/6 of the size of a square, i.e. around 60 µm, as shown in Figure 4.15 b. This is a known

problem with the IFTA approach due to the discrete and finite pixel grid of the SLM display and hence limits the resolution on the features that can be produced. The dynamic nature of the SLM in combination with the relatively long dwell time required for machining enables the minimisation of the effects of the speckled intensity distribution using a speckle reduction technique and this will be discussed in section 4.1.9.

4.1.7 Temporal fluctuations of phase modulation

The SLM LC-R 2500 from Holoeye has the advantage of being based on a standard SLM display which was initially developed for visual applications. The phase modulation of this device exhibits inherent time fluctuations as analyzed by Lizana et al. [163, 167]. This is due to the electrical addressing of the display. Such standard SLM display devices are typically addressed by a pulse-width modulated signal resulting in a temporal variation of the voltage applied to each pixel of the display [164, 168]. The fluctuations that result are not visible to the human eye and so this is not a problem when used as a display. However, when applying SLMs to laser micromachining with pulse repetition rates a few orders of magnitude higher than the flicker frequency, these fluctuations can adversely affect the machining outcome as demonstrated in this section.

In order to determine the temporal beam shaping response of the SLM, a high speed camera (Kodak 4502m) was placed close to the focus of the optical system to monitor the spatial intensity distribution of the laser pulses. For this purpose the laser beam was highly attenuated by means of a beam splitter with a splitting ratio independent of the orientation of the polarised light, and additional neutral-density filters. The maximum frame rate of the high speed camera is 40.5 kHz with an image resolution of 64 x 64 pixels. The shutter time at this frame rate is ~24 µs. The laser repetition rate was set to 40.5 kHz, i.e. the same frequency as the maximum frame rate of camera. The shutter time is much longer than the pulse length of the laser, i.e. ~65 ns, allowing the spatial intensity distribution of single laser pulses to be investigated. For the measurement a binary grating with a phase difference of 0.8π rad was addressed constantly to the SLM. This phase difference results in similar intensities for the zero order and the first diffraction orders of the laser beam and was chosen to emphasize the impact of the zero order flickering. These spots were positioned slightly off focus at the high speed

camera, giving a diameter of ~15 pixels. The average intensity of a 20 pixel diameter area for each spot was calculated in software in order to determine their relative intensities. As shown in Figure 4.18, the intensities of the zero order and of the first diffraction orders vary significantly with time, despite the binary grating being addressed continuously to the SLM. The temperature of the SLM display was 24° C measured using a pyrometer. The period of the fluctuation is determined to be ~13.3 ms which corresponds to a frequency of 75 Hz. This matches the frequency of the graphics card controlling the SLM. In addition to the 75 Hz main component a higher order sub-fluctuation with a period of ~7.8 ms and ~5.5 ms is visible. These fluctuations are also referred to as flickering, as reported by Lizana et al. [163, 167] and Hermerschmidt et al. [164]. This flickering can be a significant problem for the application of such an SLM for beam shaping in laser machining, in particular with laser repetition rates typically being a few orders of magnitude higher than the frequency of the flickering. The narrow peaks appearing in the intensity plot in Figure 4.18 are probably artefacts due to the laser and the high speed camera using different clocks resulting in slight differences in the operating frequency of 40.5 kHz. The intensity values for the +1 and -1 diffraction order are slightly different since the plotted intensity values are obtained by averaging a finite, but discrete area of the intensity image from the high speed camera.

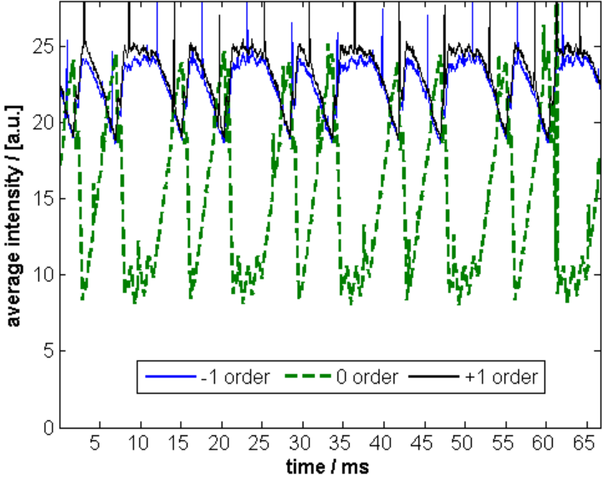

Figure 4.18: Fluctuations of intensities of zero and first diffraction orders due to flickering of the SLM (temperature of display 24°C).

In Lizana et al. [163, 167] it is reported that the temporal fluctuations depend on the addressed grey levels to the SLM and on the polarisation devices before and after the display. For their measurements a different orientation of polarisation of the light

incident on the SLM and polariser behind the SLM were used. Hence, the experiments as described above, with linearly polarised light incident onto the SLM with an angle of 20° to the short axis of the display (see Figure 4.5), and no additional polarising element after the display were repeated for different grey levels. Two sets of binary gratings where addressed constantly to the SLM while the temporal course of the intensities of the zero order and the first diffraction orders are measured using the high speed camera as before. The period of the gratings was 40 pixels. For one set of the binary gratings, one phase level was set to "white" with a grey level of 255, corresponding to the maximum index value of the LUT, i.e. 508. The grey values of the second level were chosen to be 192, 128 and 64, resulting in a phase different of π/2, π and 3π/2 respectively. The results are shown in Figure 4.19. For the second set of binary gratings, one phase level was set to "black" with the grey value 0. As before, the grey values of the second level were 64, 128 and 192, resulting in phase differences of π/2, π and 3π/2 respectively (results shown in Figure 4.20). In all cases the temporal fluctuations have a period of ~13.3 ms corresponding to a frequency of 75 Hz. The individual traces of the flickering behaviour, however, strongly depend on value of the grey levels sent to the SLM, confirming the results by [163, 167].

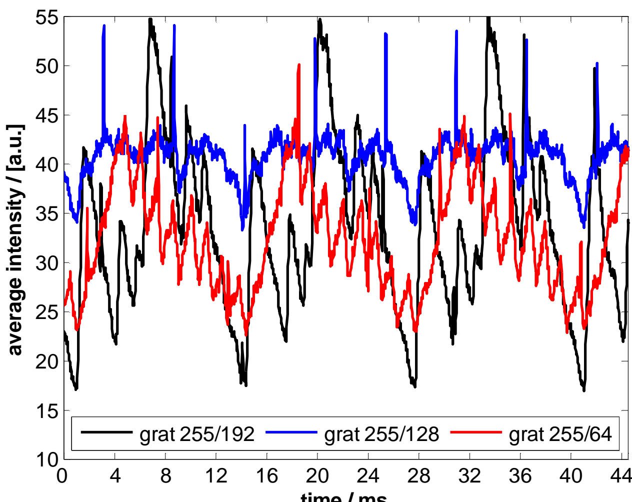

Figure 4.19: Fluctuations of the first diffraction order when addressing binary gratings with grey levels (255/192), (255/128) and (255/192) constantly to the SLM. The period of the flickering is ~13.3 ms in all cases, though the individual course of the flickering severely depends on the grey values.

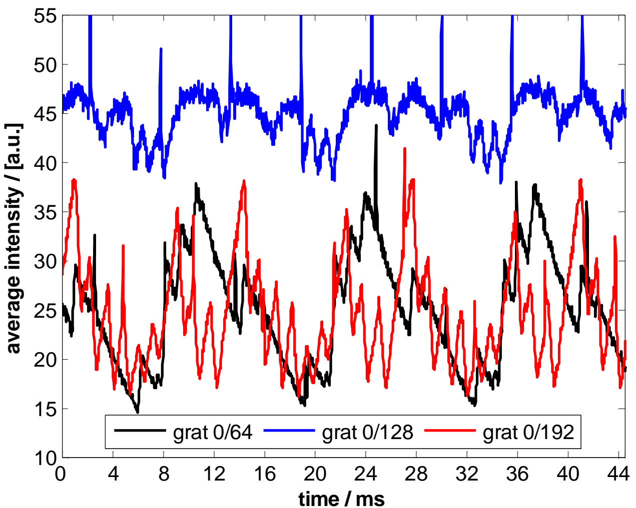

Figure 4.20: Fluctuations of the first diffraction order when addressing binary gratings with grey levels (0/64), (0/128) and (0/192) constantly to the SLM. The period of the flickering is ~13.3 ms in all cases, though the individual course of the fluctuations severely depends on the grey values.

In a further experiment, a hologram to generate a much more complex intensity distribution was addressed constantly to the SLM while the beam shape was monitored by means of the high speed camera as described above. A kinoform to generate a "smiley face" was chosen as an example utilizing all 256 phase levels of display as opposed to the two phase levels for the binary gratings before. The target profile was created on axis and the zero order beam was removed in software for the evaluation. Due to the increased beam shape the settings of the high speed camera had to be altered to an image size of 256 x 256 pixels which is only possible for a reduced frame rate of 4500 fps. The shutter time of the camera changed to 22 ms accordingly. The ns laser was operated as before at a repetition rate of 40.5 kHz. The temperature of the SLM display was 27.1°C measured with a pyrometer. The results are shown in Figure 4.21 b. As before, the period of the fluctuation is determined to be 13.3 ms and accordingly the frequency of the flickering is 75 Hz. This corresponds to the frame rate of the graphics card controlling the SLM. In addition to the flickering at 75 Hz there is again a strong higher frequency fluctuation.

For the results shown in Figure 4.18 and Figure 4.21, the temporal fluctuations of the phase modulation of the SLM display can be clearly divided into two sections, i.e. one with a period time of approximately 7.8 ms and one with approximately 5.5 ms. This can be attributed to an inversion of both the pulse-width-modulated signal and the potential of the ITO ground electrode in order to prevent a physical deterioration of the

LC molecules by a DC electric field (see section 2.3.4.1 and Figure 2.15). The display manufacturer Philips Components states a timescale of typically 5.5 ms for one cycle of the electronic addressing pattern [100] which corresponds very well to the experimental data.

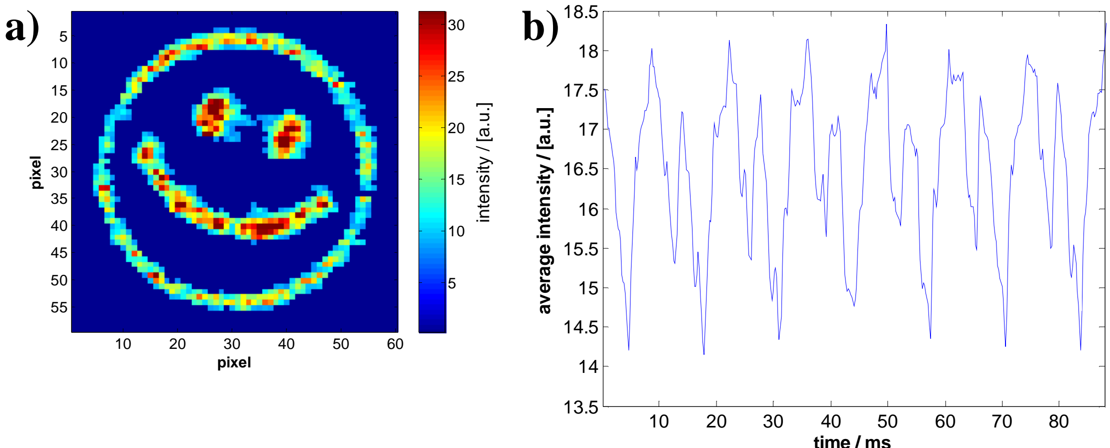

Figure 4.21: a) Example beam shape of "smiley face" with zero order beam blocked off; b) Temporal course of average intensity of smiley face. The period of the flickering is ~13.3 ms.

In order to investigate the impact of the temporal fluctuations of the phase response on the outcome of laser machining processes a binary grating with a phase difference of 0.8π rad (see Figure 4.18 for response) was addressed continuously to the SLM. Using a galvo scan head system (see Figure 4.11) the resulting three spots for zero order and first diffraction orders are scanned perpendicularly at a speed of 12.5 mm/s across the surface of a work piece, in this case a metal coated glass slide. The laser power was adjusted to be just above the ablation threshold of the metal. The machining result (Figure 4.22 a) clearly exhibits periodic variations with a spatial periodicity that can be associated with the flickering of the SLM at 75 Hz. The quality of the laser machining process is hence clearly affected by the flickering of the display. Comparing the machining result in Figure 4.22 a) with the intensity data in Figure 4.16, an ablation threshold of 22 [a.u.] can be estimated. This value is then used, together with the intensity data, to simulate the expected machining (see Figure 4.22 b). The predictions are a close approximation to the experimental result.

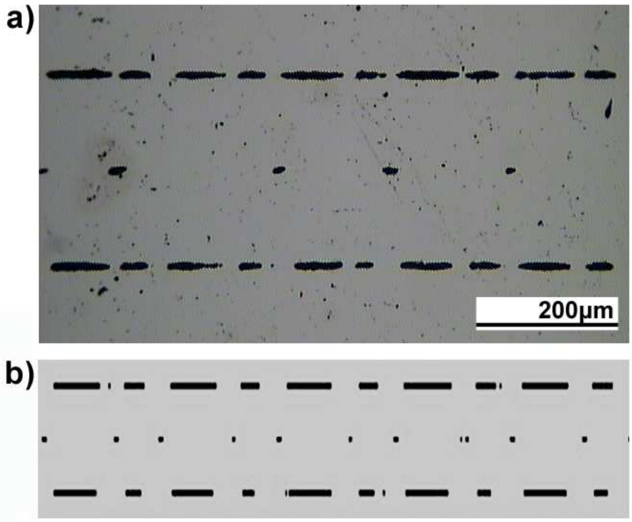

Figure 4.22: a) Laser machining using scan head (scanning direction left to right, speed 12.5mm/s) of metal coated glass slide with binary grating addressed to SLM; b) modelled machining results based on intensity data shown in Figure 4.18.

With the results presented in Figure 4.18, the copper mount to which the SLM is attached was simply acting as a passive heat sink and no additional water cooling was used. However, additional cooling can be useful in order to reduce the amplitude of the inherent flickering of the SLM. In order to explore this aspect, the experiments described above were repeated while varying the temperature of the SLM display. The intensity distribution when using the same binary grating as before, with a phase difference of 0.8π rad, was measured again by means of the high speed camera (frame rate 40.5 kHz) with a laser repetition rate of 40.5 kHz. The display temperature was controlled by a closed-loop water cooling and heating unit and monitored by means of a pyrometer. The top graph plotted in Figure 4.23 shows the dependence of the maximum and the minimum intensity values of the zero and the first diffraction orders on the display temperature. The lower graph shows the amplitude of the flickering, i.e. the difference between the maximum and minimum intensity values for the zero and the first diffraction orders. It can be seen that cooling the device to a temperature of 17 °C significantly reduces the amplitude of the flickering compared to a temperature of 39 °C. The amplitude of the flickering of the zero order for example is reduced by ~50% from ~25 [a.u.] to ~13 [a.u.]. Display temperatures of around 40 °C are typically reached when operating the laser at full power (i.e. 14.7 W) incident on the SLM over a timescale of tens of minutes with the copper mount acting as a passive heat sink without water cooling.

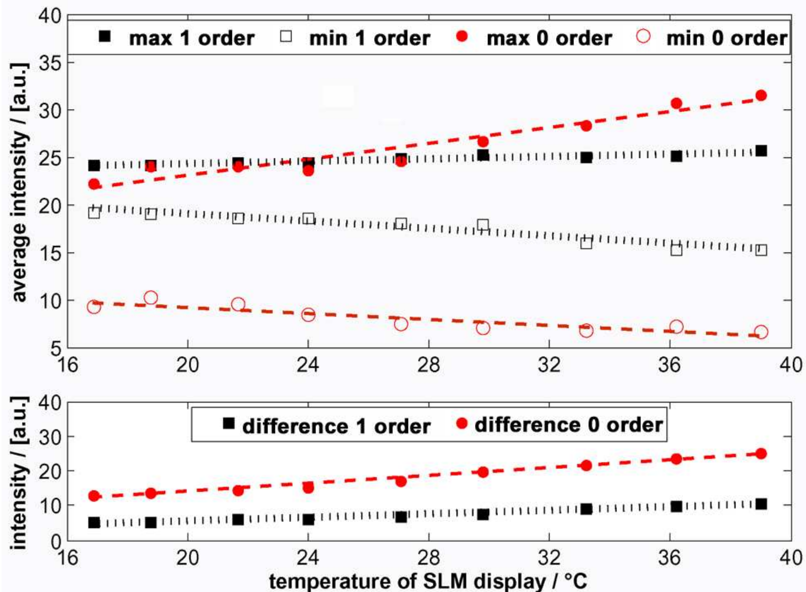

Figure 4.23: Temperature dependence of flickering for zero and first diffraction order intensities: maximum and minimum intensity values for flickering (top section); difference between maximum and minimum values (bottom section).

This temperature dependence of the flickering can be explained by temperature-induced changes in the viscosity of the liquid crystals. The viscosity determines the response of the liquid crystals to changes of the applied electric field, driven by the pulse-width modulated signal. Clearly at lower temperatures, the speed of response of the liquid crystal layer to changes due to the electronic addressing of the display is reduced. The liquid crystal on silicon (LCoS) display used in this SLM is manufactured by Philips (model X97c3A0) and uses 45° twisted nematic liquid crystals. Information regarding the exact type of liquid crystal and also information about the viscosity and especially the rotational viscosity coefficient of this particular liquid crystal were not available from the manufacturer. This prevents a more detailed explanation of the measured linear dependence of the amplitude of the flickering on the temperature as shown in Figure 4.23 aside of some more general comments. In general, the viscosity increases at lower temperatures due to the lower molecular kinetic energy [101]. In [102] an empirical rule is given which states that the rotational viscosity increases by a factor of two for every temperature drop of around 10 – 15 °C. Further cooling of the device has been limited by the dew point of ambient air since these experiments were carried out in the normal lab environment. For lower temperatures water condensation at the cover glass of the display will occur and in combination with a high power laser beam could potentially damage the SLM display.

The big advantage of SLM devices, compared to fixed optics, such as conventional gratings or diffractive optical elements, for beam shaping applications in laser machining is the potential to change between different phase profiles 'on-the-fly', i.e. during the actual machining process. In order to determine the response for varying or alternating phase distributions the experiments as described above were repeated using the high speed camera with a frame rate of 40.5 kHz and operating the laser at a repetition rate of 40.5 kHz. For simplicity, two binary gratings were chosen, having the same periodicity, i.e. 40 pixels, and phase difference of π rad (grey levels 128 and 0) but shifted by half the periodicity relatively to each other. These gratings, although different, generate identical spatial intensity distributions at the focus of the system and thus facilitate an easier analysis and comparison of the data from the high-speed camera. The results are shown in Figure 4.24: When the change of the addressed grating occurs, i.e. after ~26 ms in Figure 4.24, the intensities of the first diffraction order drop almost to zero over a timescale of ~16 ms and the zero order intensity rises accordingly. Over a timescale of ~34 ms the intensity values trace back to the initial levels prior to the change. This behaviour can be attributed to the finite response time of the liquid crystal layer due to its viscosity. As mentioned before, detailed information about the used liquid crystal and the geometry of this display is not available, preventing a further analysis. The fine structure of the transition can be again associated to the pulse width modulated signal used for driving the display. In between the changes, e.g. between 75 and 135 ms in Figure 4.24, the normal flickering behaviour as shown Figure 4.20 (blue curve) can be observed. The binary gratings were addressed to the SLM by means of a slide show using IrfanView software based saved bitmap files of the gratings. Although the delay time for each frame of the slide show was set to 100 ms, the measured response shown in Figure 4.24 exhibits a delay of ~110 ms between the changes, most likely caused by a synchronisation issue between the software and the graphics card.

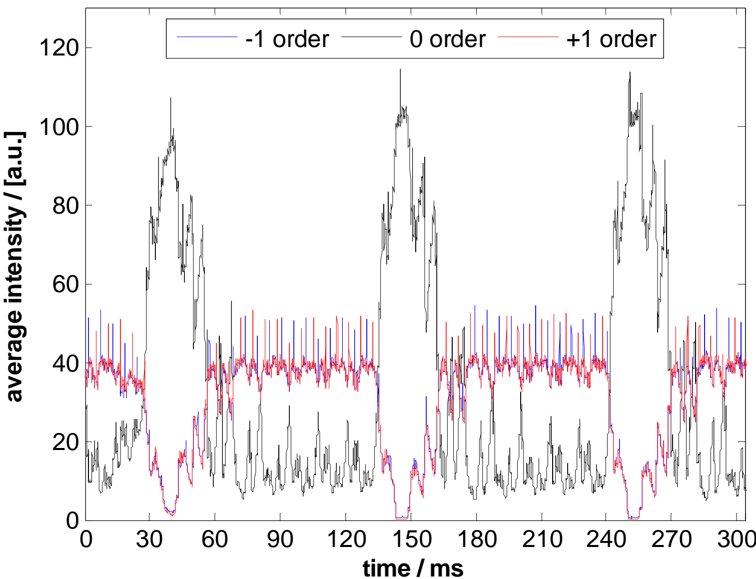

Figure 4.24: Average intensities of zero order and first diffraction orders when addressing two similar but shifted binary gratings with phase difference of π alternating to SLM with a delay of 100 ms.

4.1.8 Process synchronisation technique for flicker compensation

As presented above, cooling can be used to significantly reduce the amplitude of the flickering for a SLM with a pulse width modulated control signal; although it cannot be eliminated fully. Thus, a process synchronization technique was developed between the graphics card controlling the SLM and the nanosecond laser machining workstation in order to block the laser beam and stop the galvo motion during the flicker and thus prevent unwanted machining. The basic idea is to trigger the shutter of the laser and the galvo scanhead system with a delayed signal from the graphics card based on previous measurement and analysis of the flickering process. For this purpose, the vertical sync pulse of the graphics card, defining the start of a new frame, is extracted from the graphics card and used as trigger signal for a pulse generator. The custom output signal from the pulse generator is connected to an optically isolated I/O input of the control unit of the scan head system in order to externally trigger the laser machining workstation. The results when machining stainless steel at a scan speed of 40 mm/s having again a binary grating with a phase difference of 0.8π rad addressed to the SLM are shown in Figure 4.25 a) for the normal and un-synchronized process and b) using the process synchronization technique. For the latter result (Figure 4.25 b), the laser machined lines arising from the first diffraction orders are continuously black implying similar beam intensities when scanning the beam across the work piece. The impact of the zero order can therefore be significantly reduced. The remaining energy in the zero

order is causing some visible melting at the surface of the work piece. It should be noted, however, that for this experiment, the shutter of the laser was open and the scan head system moving for only 40% of every frame of the graphics card and respectively the SLM, so the removal of the flickering in order to improve the quality of the laser machining for this particular case is associated with an increased processing time by a factor of 2.5.

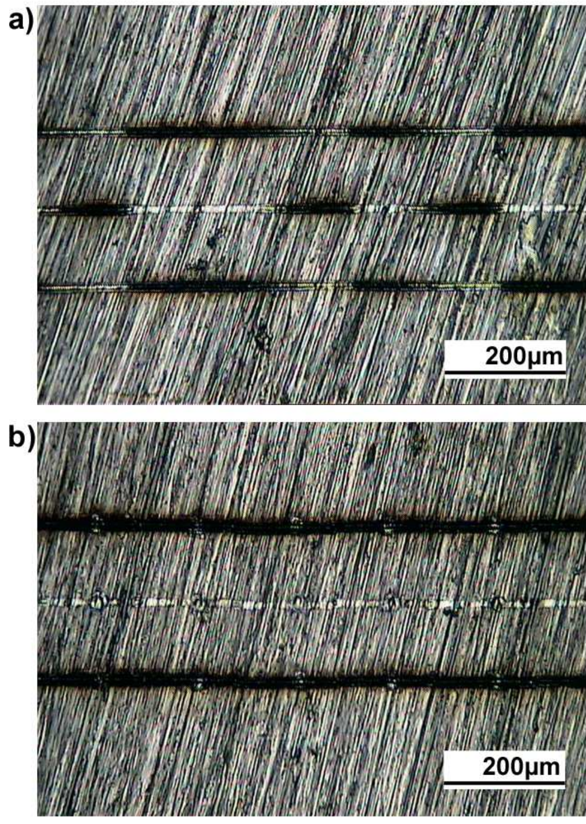

Figure 4.25: Machining result after scanning a laser beam modulated by a constant binary grating at a speed of 40 mm/s across stainless steel: a) without and b) with flickering compensation using process synchronization.

Such a synchronisation technique is not restricted to binary phase gratings. It should also be possible to eliminate the flickering of computer generated holograms utilising the full 256 available phase levels by using synchronisation, e.g. based on the data shown in Figure 4.21, although this has not been experimentally demonstrated to date. For laser machining applications utilising 256 phase level holograms and consequently beam shapes much bigger than the initial Gaussian shape, the dwell times are typically much longer than the flickering period. Consequently, the impact of the flickering of the created intensity distribution on the outcome of the laser machining is less obvious compared to scanning multiple spots created using diffraction gratings.

4.1.9 Speckle reduction technique

This section is based on collaborative work together with Dr. Jonathan Parry. When using the SLM as a diffractive optical element, speckle can affect the quality of the laser machining, as shown in Figure 4.15, and hence limit the resolution on the features that can be produced. The speckled intensity distribution is an inherent problem of phase only holograms determined using the Gerchberg-Saxton algorithm [27] or iterative Fourier transform algorithm [28]. Speckle is high frequency noise that arises from random interference between the overlapping point spread functions of adjacent spots in the image plane (see [169] for more details). The problem can be bypassed by generating sparse and non-overlapping diffraction limited spots [170], with potential application in optical trapping or for parallel processing. However, for laser beam shaping typically requiring continuous intensity distributions more direct solutions are required.

One approach is to introduce a smoothing constraint to the resulting image plane to avoid sudden phase changes between adjacent spots [28]. This approach eliminates most of the speckle, however, it demands significantly higher computational efforts and still cannot eliminate speckle arising from so called optical vortices which are isolated zeros of the phase distribution [169].

The second, much more common approach to the reduction of the speckle problem is to temporally modulate the speckle distribution at a rate which faster than the temporal response of the detector [171]. Such a time-averaging technique is for example used for laser projectors where multiple images having identical amplitude but different phase distributions are displayed faster than the response time of the eye. As result a single time averaged image with reduced speckle contrast is perceived by the observer. A further reduction of the speckle can be achieved by integrating some kind of mechanical modulation such as a moving diffuser to the system [172]. With respect to nanosecond laser machining applications that typically require multiple laser pulses such a time averaging technique can be easily applied.

In order to obtain images of identical amplitude, but different phase, based on phase-only holograms, random and statistically independent phase distributions can be used as a starting condition for calculating the hologram [171]. The combination of a number of N different holograms all creating images with identical amplitude, but different

phase, results in a reduction of the speckle contrast by a factor of $\sqrt{N}$ [173]. Golan and Shoham presented a less computationally intensive approach to generate these phase patterns for application with phase-only SLMs [174]. A single hologram, also referred to as kinoform, is calculated and then a series of copies that are cyclically shifted in horizontal and vertical direction are produced (see illustration in Figure 4.26). Shifting the pixels of the computed hologram changes the reconstructed phase pattern of the image, but does not affect the reconstructed amplitude. Random phase shifts to create, for example, 16 kinoforms result in a time averaged combination with reduced speckle contrast by a factor of 4 according to the theory [173]. Golan and Shoham demonstrated mathematically that a deterministic choice of the shift distance will meet the requirements that summation of the individual speckle patterns cancel exactly [174]. In practice, a series of periodic shifts in orthogonal planes is recommended and in principle this approach can completely eliminate the effect of speckle on the combined image.

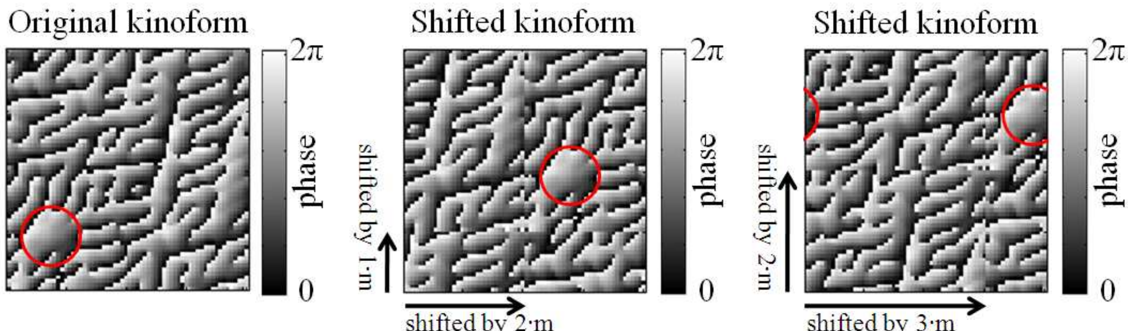

Figure 4.26: Demonstration of periodic shift of hologram respectively kinoform in horizontal and vertical direction with increments m of a quarter of the size of the initial kinoform. The red circle tracks a single feature.

The practical implementation of the shifted kinoforms is simple and effective. Both approaches of random shift distances and of deterministically selected shift distances have been carried out. For the deterministic method according to [174] 16 shifted kinoforms shifted by an increment of a quarter of the size of the original kinoform in horizontal and vertical directions were calculated. The initial kinoform had a dimension of 256 x 256 pixels, so the increment was 64 pixels. The generated kinoforms were tiled in a 3 x 4 pattern resulting in a 768 x 1064 pixels phase pattern to be addressed to the SLM (see Figure 4.14). Repeating the individual kinoform in a tiling style approach is a common approach to improve the diffraction efficiency and the uniformity of the

resulting image [165]. In addition to this periodic shift approach, random shift distances were also tested, again using 16 kinoforms.

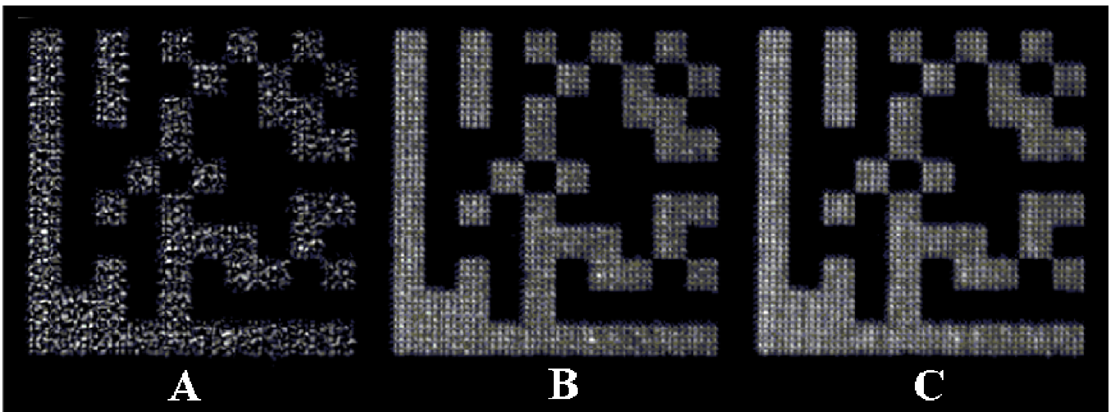

Figure 4.27: Images of holograms formed at the end of a 6-f optical system taken using a CCD camera: A) Result for the original calculated kinoform (without application of speckle reduction technique), B) 16 images taken for randomly shifted kinoforms, combined and normalised in software, C) 16 images taken for periodically shifted kinoforms, combined and normalised in software.

Figure 4.27 shows camera images of the resulting beam profiles at the focus of a 6-f optical system similar to the one described in 4.1.6 to demonstrate the effectiveness of these techniques. There target profile was set off axis and the zero order beam was blocked off. The target profile had a size of 128 x 128 pixels and the total size of the data matrix pattern was 50 x 50 pixels. A small final image size was desired in this context and consequently pixelation is apparent in the resulting images. Figure 4.27 a) shows the resulting image from the initial calculated kinoform which is highly speckled in nature. Figure 4.27 b) and c) are software combined images resulting from 16 randomly and respectively periodically shifted kinoforms. Although the pixelation is still apparent the impact of the speckle is reduced significantly in both cases. To further evaluate the speckle contrast, the intensity distribution within the same section, i.e. the L-shaped bracket, of each image was determined, normalised to a maximum intensity value of 255, and is shown in Figure 4.28. The dotted line shows the case where each pixel element within the hologram image has been adjusted to the same peak intensity representing the best case intensity distribution with zero speckle contrast but with a pixelated image. The dashed line illustrates the ideal case where the speckle contrast is zero and there is no pixelation. Pixelation in the reproduced image corresponds directly to the pixels in the initially defined image used to calculate the phase profile. The randomly shifted phase approach gives a significant improvement in uniformity in the

reproduced image compared to the single image produced from a single phase profile and the periodically shifted phase approach results in a further small improvement.

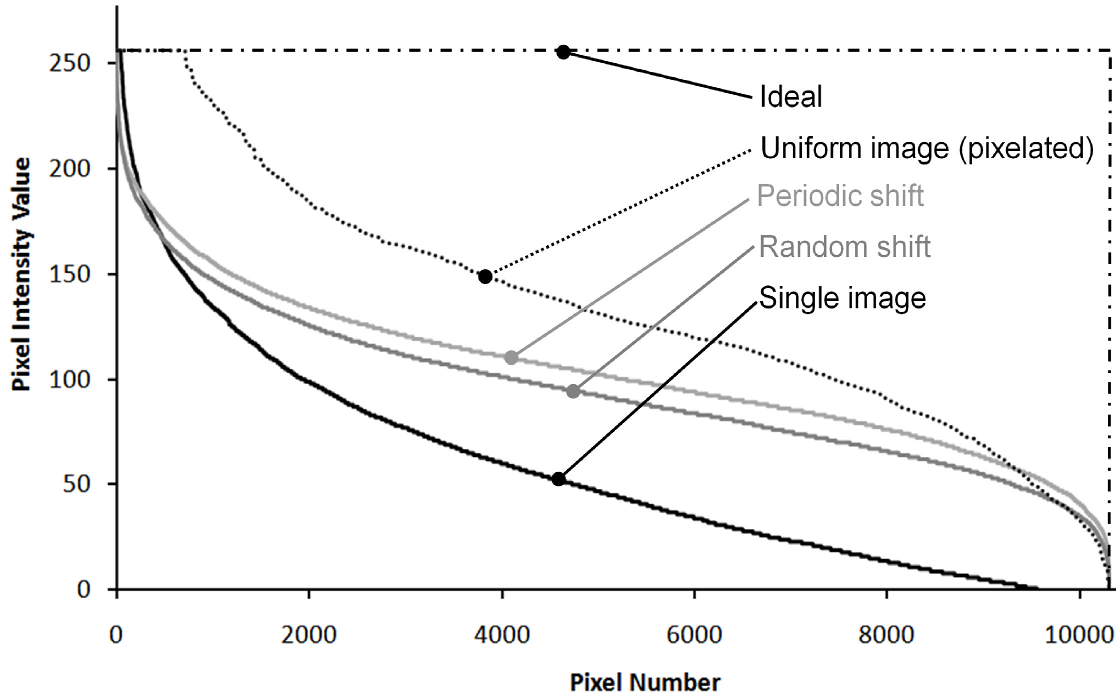

Figure 4.28: Plot of normalised intensity values taken from each image shown in Figure 4.27. Plots are also shown for the ideal case and for the case where the image is still pixelated but each pixel is of uniform intensity.

In the following experiments the above described speckle reduction technique was applied to laser marking with the nanosecond laser machining workstation. The laser was operating at full power at a repetition rate of 15 kHz in order to maximise the pulse intensity available at the work piece. Marks were made using varying dwell times at fixed locations on the surface to achieve the best possible results. The setup is shown in Figure 4.11. There was no relative motion between the laser focus and the work piece during the marking process. The average optical power incident on the SLM was approximately 12 W, however only ~3.5 W was delivered to the image on the work piece. The losses are primarily due to the limited diffraction efficiency of the SLM device for the specific pattern but also due to other losses in the optical system including reflection losses from optical components and the reflectivity of the SLM. Figure 4.29 shows an initial attempt at marking using the SLM. Figure 4.29 a) shows the image used as a starting point to calculate a single kinoform to display on the SLM. Figure 4.29 b) shows the result of marking this pattern on a thin aluminium film coated on glass, using 9 exposures of 100 ms each. The laser marked areas are visible as dark

areas showing where the metallic film has been removed. The mark caused by the zero diffraction order is prominent in the centre of the image.

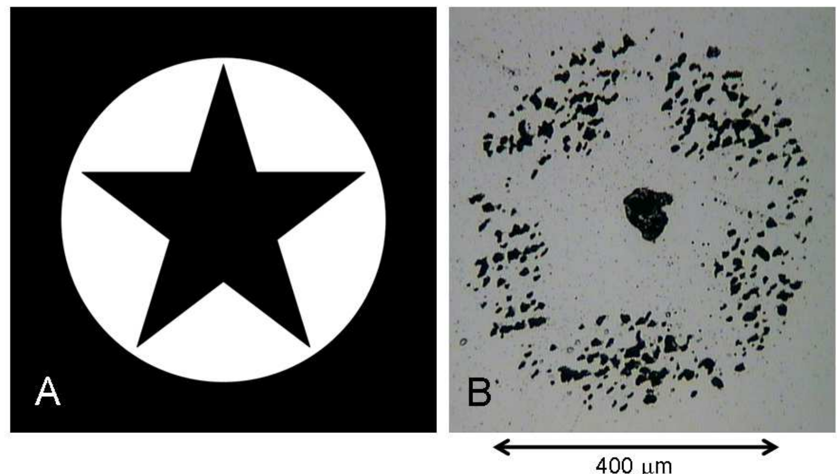

Figure 4.29: A) Star pattern used to derive kinoform for hologram. B) Star pattern marked on thin layer of aluminium coated on glass. A kinoform was marked 9 times with 100 ms exposure.

In Figure 4.30 the same star pattern has been marked, however this time the pattern is off axis to separate the machined region from the zero order beam which in the case of the experiment shown in Figure 4.29 is outside of the image area. Each image in Figure 4.30 was laser marked by 16 exposures of 200 ms each however with varying kinoforms in each case. In Figure 4.30 a) a single kinoform was used and consequently the machined area exhibits a high level of speckle. For the results shown in Figure 4.30 b) the original kinoform was taken and shifted randomly sixteen times to modulate the speckle profile. With each of these patterns laser marking with an exposure of 200 ms each was carried out sequentially and the result shows a significantly reduced speckle contrast and a much clearer image. The same approach was utilised to produce Figure 4.30 c), however in this case periodic shifts of the kinoform were carried out with an increment of a quarter of the kinoform size. This results in some further improvement in the speckle contrast in accordance with the graph shown in Figure 4.28.

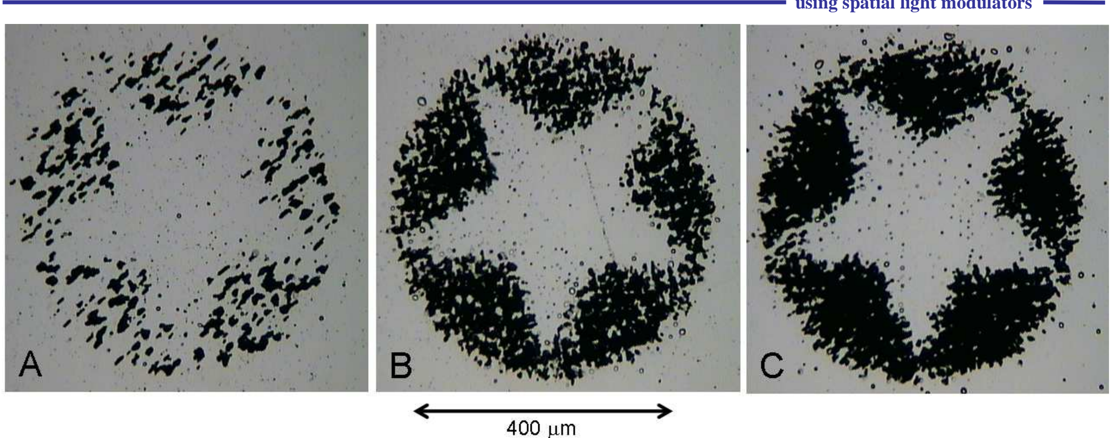

Figure 4.30: Marks on a thin layer of aluminium coated on glass created using an SLM to produce an off-axis image: A) Single kinoform marked 16 times with 200ms exposure; B) 16 randomly shifted kinoforms marked for 200 ms each; C) 16 periodically shifted kinoform marked for 200 ms each.

Laser marking with slightly more complex patterns is demonstrated in Figure 4.31. In Figure 4.31 a) a 10×10 datamatrix pattern representing the letter "A" is shown. This pattern is marked into a layer of aluminium coated on glass. The image was laser marked sequentially using 16 periodically shifted kinoforms with an exposure time of 10 ms each. For each element of the datamatrix pattern, a 5 × 5 pixel square was used for the target profile of the IFTA with a size of 128 x 128 pixels. This turned out to be the minimum number of pixels that can be used while maintaining a reasonable quality reconstruction. Figure 4.31 b) shows a similar pattern marked in photo-resist based on 16 periodically shifted kinoforms for 300 ms exposure each. In the bottom right corner the inherent mark from the zero order is apparent. For the photo-resist, laser marking of a larger area is possible due to the material properties, specifically the increased optical absorption, and the lower melting/vaporisation points and the lower thermal mass. The metal substrate underneath the photo-resist has a much higher machining threshold and consequently is unaffected by the laser marking process.

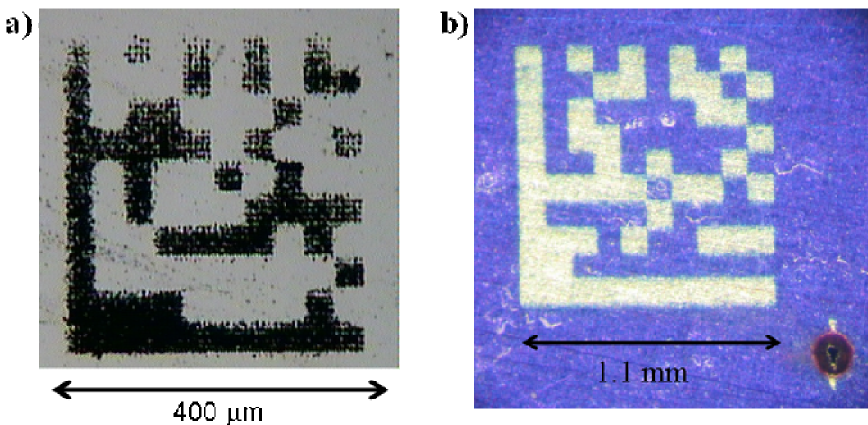

Figure 4.31: a) Data matrix pattern representing character "A" marked on thin layer of aluminium coated on glass. 16 periodically shifted kinoforms were marked for 10 ms each. b) Data matrix marked in photo-resist using 16 periodically shifted kinoforms marked for 300 ms each. The stainless steel substrate is untouched by the machining process.

Both laser marking results shown in Figure 4.31 are clearly well defined with sharp edges. Some pixelation is apparent in Figure 4.31 a) as well as a fading of the mark towards the top of the shape. This is a result of the slightly non-uniform intensity gradient in the diffraction image used for marking. Due to the high optical intensity required to machine a metal combined with a high thermal conductivity it is necessary to strike a balance between over marking the lower portion of the image and under marking the top. In Figure 4.31 b) the larger scale image in photo-resist does not show this gradient; because of the lower machining threshold and larger scale, machining can continue until all of the resist is removed in the desired regions without causing noticeable thermal damage at the edges of the mark.

4.1.10 Laser machining on bulk material

This section is based on joint work together with Dr Jonathan Parry. The ability to laser machine photo-resists and metal films has only a limited number of useful applications, whereas the ability to machine bulk materials would open up a wider range of applications. Thin films typically have a relatively low machining threshold due to their low thermal mass. In the nanosecond regime material is removed by a combination of evaporation and melting. Since the intensity distributions created by means of the SLM as a diffractive optical element are rather large, the laser intensities available for the marking reduce and consequently the machining processes presented tend towards a thermal melting process rather than ablation. When machining bulk materials the greater thermal mass in the component results in heat being conducted away from the

mark during the machining process and thus reduces the overall machining efficiency. Since in most of the processes shown so far the laser is already operating at the maximum available power, the only means of increasing the laser intensity is to reduce the size of the shapes.

To achieve this, the final lens of the system was replaced initially by a 50 mm focal length singlet lens and was subsequently replaced by an even shorter focal lens doublet of 30 mm. For shorter focal lengths in relation to the beam diameter the use of a doublet lens is essential to minimise aberrations in the intensity distributions at focus. A laser marking result with a width of 370 µm on stainless steel using the 50 mm lens is shown in Figure 4.32 A). The surface of the work piece was polished mechanically using silicon carbide polishing papers down to 4000 grit before the mark was generated and some lines are apparent from this polishing. The machining result shows that the individual features of the data matrix start to blur together, but nevertheless the pattern is readable by standard decoding software [175]. This blurring results from the thermal nature of the process in the nanosecond regime and the spread of heat affected zones over the relatively long marking times. Using the 30 mm doublet lens as final lens of the system, smaller scale marks with a width of 200 µm can be achieved as shown in Figure 4.32 B). As before, the work piece was polished stainless steel. In order to minimise the spread of the heat during the process, this mark was created sequentially from four different patterns shown in Figure 4.32 C). With the exception of the bracket the data matrix pattern was split up such that no two squares adjacent to each other where laser machined at the same time. In this instance the shape was separated manually, however this could conceivably be achieved using a computer algorithm. A disadvantage here is the increase in computation time to split the shape and produce three phase profiles instead of one (the phase profile required to generate the bracket being standard for each code). The increment of the speckle reduction process was reduced from a quarter to a third of the hologram size to reduce the number of different phase patterns used from 16 to 9 for each frame. In total 36 different frames were marked with an exposure time of 1.7 ms each. This reduction of the machining time from 100 ms to 1.7 ms arises from the significantly increased laser intensity at the work piece due to the smaller size of the intensity distribution and due to splitting the data matrix into parts. Taking the thermal diffusivity of stainless steel as 4.2×10^{-6} m^2/s an estimate of the thermal diffusion length over the marking time can be made of ~20 µm in Figure 4.32 a) compared to just 3 µm in Figure 4.32 b). These numbers appear

broadly consistent with the extent of the heat affected region in each image. A further reduction of the size of the mark would result in an increased intensity and consequently in a further reduced marking time and heat affected area.

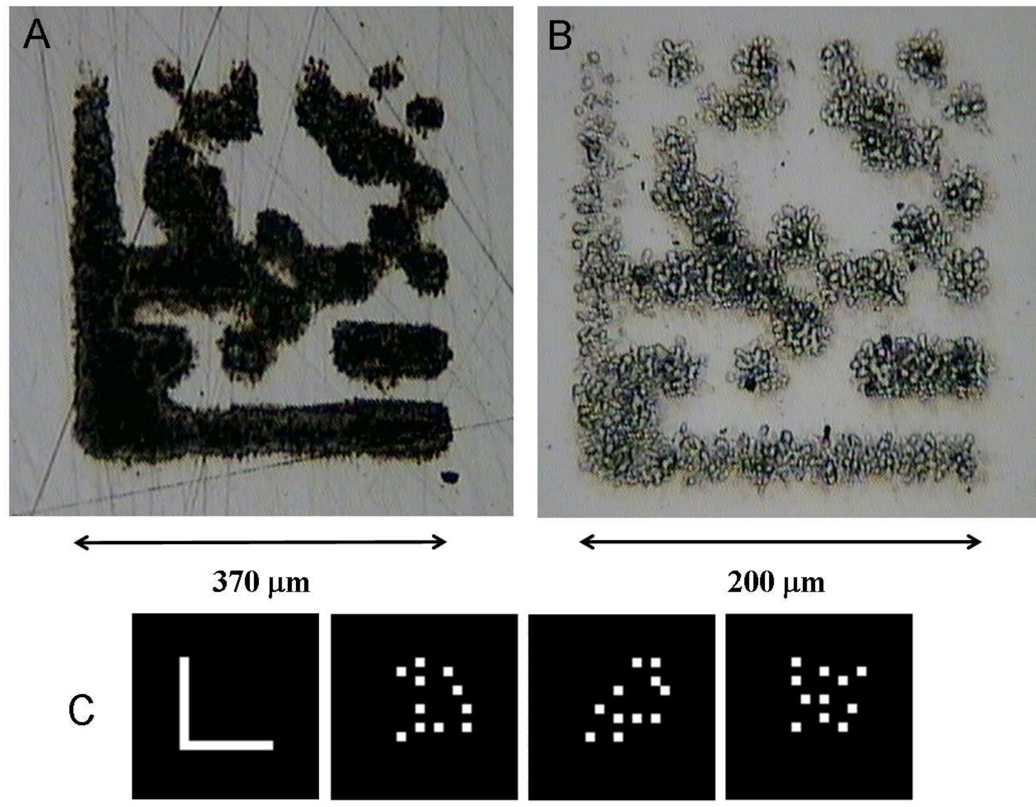

Figure 4.32: Data matrix representing the letters "AOP" marked on stainless steel. A) Using a 50 mm single element lens and 16 periodically shifted kinoforms marked for 100ms each. B) Using a 30 mm doublet lens four overlapping patterns are marked using a total of 36 periodically shifted kinoforms each marked for 1.7 ms. C) The four separate patterns used to build up the mark shown in B.

The shape in Figure 4.32 B) is well defined although the edges are not perfectly sharp. Nevertheless, the pattern can be easily decoded using appropriate software [175] demonstrating that the mark is fit for purpose as a discrete tracking mark that may be applied to a variety of components.

A further reduction of the size of the mark is mainly limited by two factors. Firstly, the ability of the optical system to generate an image of sufficient resolution and uniformity and secondly the requirement for sufficient optical intensity to mark the surface without thermal effects in the material degrading the mark quality. In practice the size of the image is limited by the numerical aperture (NA) of the final lens. The 30 mm focal

length doublet used here had an NA of 0.423 which represents the optimum for commercially available off-the-shelf components in terms of focal length and lens diameter. For a given image size the mark quality may be improved by reducing the machining time in order to reduce the heat affected zone around the mark. This may be achieved by increasing the laser intensity which would require changing to a higher power and/or shorter pulse length laser system, adding significantly to cost, or improving the efficiency of the optical system, the least efficient component being the SLM itself. Clearly reducing the mark area also increases the intensity and can reduce thermal effects.

Due to the limitations in intensity, the machining results that are possible with the SLM are limited to small scale (sub mm) marks in bulk metal surfaces or slightly larger marks in more easily machined materials such as photo-resists. Discrete small scale marks are of value as a means to provide traceability of high value components and this is a possible application area in which the SLM could offer a significant advantage over more conventional scanning techniques enabling the rapid generation of distinct codes. Alternatively, the device could be useful in developing a process which requires a fixed diffractive optic enabling quick realisation of iterations in a design process. In conjunction with a scan head system the SLM could be applied to surface structuring or patterning. One application of such an approach would be the direct writing of etching masks in photo-resist thus avoiding the developing stage.

4.1.11 Application of modified iterative Fourier transform algorithm (MIFTA) and closed loop feedback

As discussed in section 4.1.9 the application of a series of periodically shifted holograms according to [174] significantly reduces the impact of speckle and improves the quality of the laser machining. However, the intensity distributions generated by means of the SLM and the IFTA typically exhibit an intensity gradient with lower intensity further away from the optical axis [176]. As a result, the laser machining result shows a fading of the mark further off axis as seen in Figure 4.31 a) towards the top of the shape.

In order to compensate for this, a modified iterative Fourier transform algorithm (MIFTA), as published by Liu et al. [177, 178] and Thomson et al. [32], in combination

with a feedback loop based on the measurement of the actual intensity distribution is applied in addition to the speckle reduction technique. This results in both an increased diffraction efficiency and improved uniformity of the generated intensity distribution, and further improves the quality of the laser marking as demonstrated in this section.

The modified iterative Fourier transform algorithm (MIFTA) was developed by the Diffractive Optics Group at Heriot-Watt University [32, 177, 178] and Dr. Andrew Waddie kindly provided the algorithm for the experiments. This technique is based on the Gerchberg Saxton algorithm, but with the output constraints modified by analyzing the (theoretical) irradiance patterns generated from the previous iterations of the algorithm. The modified Fourier-domain constraint function is based on the difference between the output results of the Gerchberg Saxton or the output results for each new iteration, and the desired output intensity distribution (see Figure 4.33, source [32, 177]). This method takes the pixelated structure of the diffractive optical element, or in our case the SLM, and also the quantized phase levels of each pixel into account. The 256 phase levels for every pixel of the SLM can be considered as "quasi-continuous", so the consideration of quantized lateral phase profile of the SLM within the algorithm is the main benefit of the MIFTA in this context [31]. The MIFTA results in both improved diffraction efficiency and an improved uniformity of the irradiance.

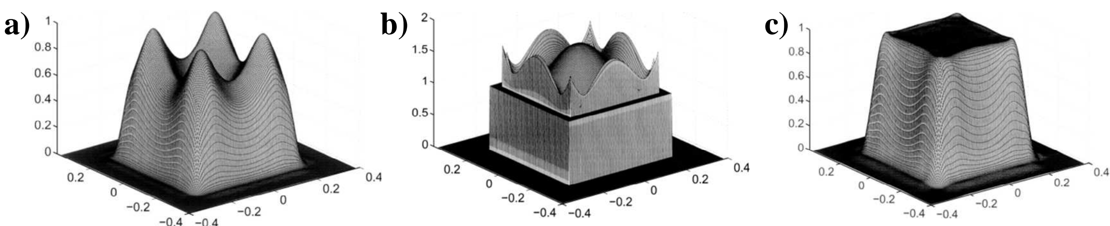

Figure 4.33: Illustration of the MIFTA principle: a) Far-field intensity distribution of previous iteration; b) modified constraint; c) desired output. It can be seen that the modified constraint is a mirror image of the output from the previous iteration about the desired output.

In addition, the resulting beam shape obtained when addressing the kinoform to the SLM including the speckle reduction technique was measured using a monochrome CCD camera. The information obtained about the time averaged intensity distribution was fed back in a closed-loop control for a further modification of the target profile. The measured beam shape is subtracted from the desired output to determine the target profile for the following iterations of the MIFTA. This enables, for example,

compensation for potential adverse effects of nonlinearities of the SLM phase response. This phase response has been calibrated with a low power laser source at room temperature (see section 4.1.3). Using this adaptive feedback loop for the target modification can also enable compensation for changes of the phase response due to heating up of the device during the laser machining process.

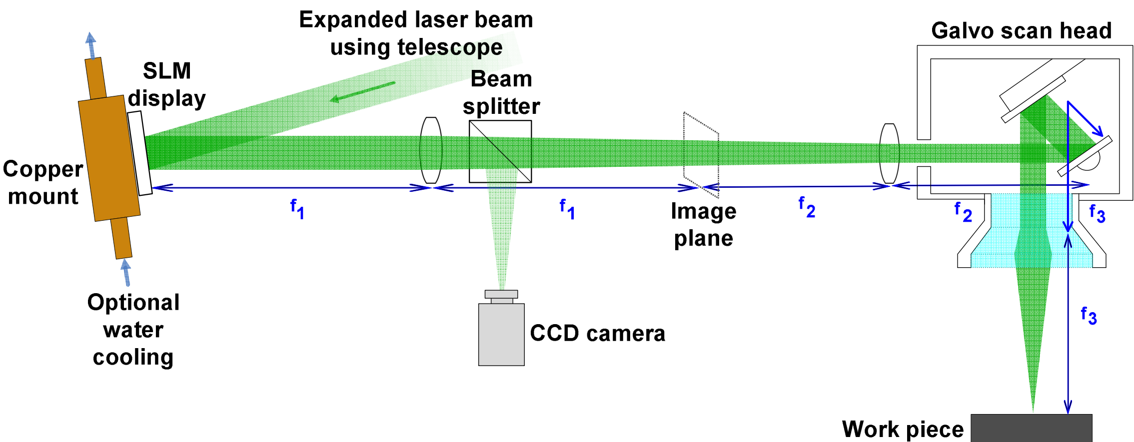

Figure 4.34: Setup of SLM embedded into laser machining workstation including CCD camera for adaptive feedback.

Figure 4.34 shows the setup for the experiment. The 6-f optical system setup is identical to the one described in section 4.1.4. The system consists of two lenses and the flat field lens of the galvo scan head is used to focus the laser beam onto the work piece. When using the SLM as diffractive optical element, e.g. using the IFTA algorithm, the desired intensity distribution is generated at the image plane of the first lens (2-f system) and at the focus of the scan head (6-f system). A polarisation independent beam splitter is added to focus a small percentage of the laser light onto a monochrome CCD camera. The camera is located at the image plane of the optical system consisting of the first lens and the beam splitter (2-f system). This enables the measurement of the generated intensity distribution and the value is fed back closed-loop to the algorithm. The feature size in pixels of the measured beam shape depends on the focal length of the first lens after the SLM and the array size of the CCD sensor. Typically this does not match the feature size of the target profile of the MIFTA. Hence, a careful and reliable scaling technique is essential here to avoid systematic errors.

The system works as an adaptive optics setup consisting of the SLM as the wavefront modulator, the CCD camera as the sensor and the MIFTA including the consideration of the actual beam shape as feedback loop. Figure 4.35 a) shows the beam shape captured with the CCD camera for a single computer generated hologram using the standard IFTA. The target profile for the IFTA was set off-axis to create a separation between the desired intensity distribution and the zero diffraction order (bottom right of Figure 4.35 a). The created pattern is a 10 × 10 data matrix representing the letters "AOP" (acronym of Applied Optics and Photonics research group). The laser machined pattern suffers strongly from speckle. Using the speckle reduction technique described earlier in section 4.1.9, the impact of the speckle can be significantly reduced. Figure 4.35 b) shows the software calculated average intensity when addressing 16 periodically shifted kinoforms to the SLM. The increment of the shift was 64 pixels, i.e. a quarter of the size of the initial kinoform. Using the MIFTA and a modified target based on the feedback from the CCD camera as described above, the beam shape can be further improved in terms of intensity and uniformity (see Figure 4.35 c). The average intensity of the diffraction pattern was increased by ~20% compared with the IFTA result as shown in Figure 4.35 c). Meanwhile, the standard deviation of the intensity distribution (used as a measure of non-uniformity) was reduced by ~10%.

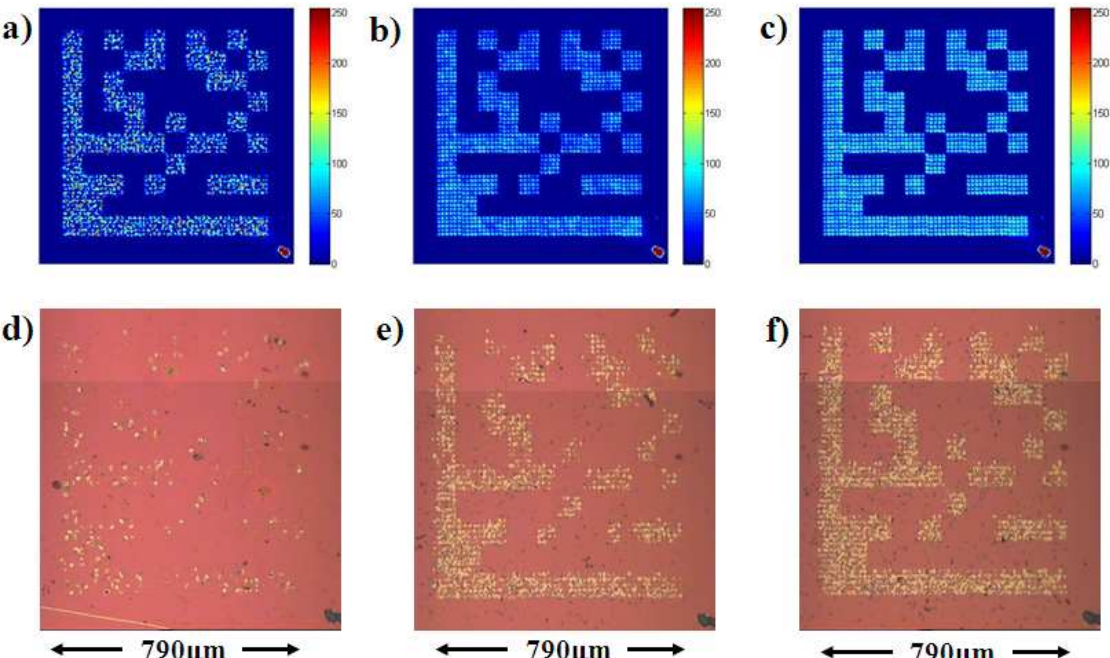

Figure 4.35: Top row: Intensity distribution measured with CCD camera: a) initial kinoform; b) software calculated average of 16 images taken for periodically shifted kinoform; c) calculated average of 16 images taken for periodically shifted kinoform based on MIFTA and feedback loop; Bottom row: Laser marks on thin metal layer coated on glass: d) single kinoform machined 16

times with 13.3 ms exposure time; e) IFTA generated kinoform shifted periodically 16 times and marked for 13.3 ms each; f) kinoform based on MIFTA and feedback loop, shifted periodically 16 times and marked for 13.3 ms each. The slight colour change in the upper one third of the images is due to using two tiled images because of the limited viewing area of the microscope.

The laser machining results for direct marking of a thin metal coating on a glass substrate with these beam shapes are shown in Figure 4.35 d) – f): The laser was operated in all three cases at a repetition rate of 100 kHz and an average power of 2.7 W which is just slightly above the ablation threshold of the metal coating. For Figure 4.35 d), a single kinoform based on the IFTA was used to machine the coated glass 16 times, each with an exposure time of 13.3 ms. The exposure time of 13.3 ms for the laser machining has been chosen according to the SLM frame rate of 75 Hz in order to avoid a potential influence of the temporal fluctuations of the phase response of the SLM on the laser beam shape (see section 4.1.7). The results when using the speckle reduction technique are shown in Figure 4.35 e) with an exposure time of 13.3 ms for each of the 16 positions of the periodically shifted kinoforms. Figure 4.35 f) shows the result based on the MIFTA and the feedback from the CCD camera machined in the same way as for the previous figure. The data matrix pattern appears much clearer in this case and the intensity gradient from the bottom left to the top right is significantly reduced. As a qualitative measure, the laser machined data matrixes were tested with standard decoding software [175] and only the data matrix shown in Figure 4.35 f) is readable as "AOP" whereas the results shown in Figure 4.35 d) and e) are not sufficiently well defined to be decoded correctly.

4.1.12 Conclusion

Despite being a conventional SLM display, initially developed for visual applications, the SLM LC-R 2500 from Holoeye can be used as a powerful tool for beam shaping in laser materials processing. It was demonstrated that the limited power handling capabilities of the device can be overcome by conductive cooling of the display. This enables the display to cope with nanosecond laser pulses with 14.7 W optical average power which is sufficient for ns laser based machining. Using the manufacturer supplied mounting, the display is insufficiently flat to facilitate the use of the SLM device in its as-is state but the custom designed mount allows for compensation of the inherent curvature of the display. Utilizing the full resolution of the display, e.g. using an IFTA approach, complex intensity distributions can be generated having sufficient

intensity for direct laser ablation. Besides the beam shaping, the SLM also enables beam steering.

The display exhibits temporal fluctuations of the phase response due to the electronic addressing which are of no concern when used as a projection device for visual applications. Consequently, the flickering created by the electronic addressing can have a significant adverse effect on the outcome of laser machining. It was demonstrated that active cooling of the display reduces the amplitude of the flickering, however, it cannot fully prevent it. A process synchronisation technique between the graphics card controlling the SLM and the laser machining workstation was developed and implemented to compensate for the flickering.

The speckled intensity distribution generated by the SLM when used as a diffractive optical element is an inherent problem and limits the quality of the laser machining result that may be achieved. The dynamic properties of the device enable the generation of beam shapes with identical amplitude but different phase distributions which results in a temporal averaging of the speckle and provides a dramatic improvement of the quality of a laser generated mark. Further improvements in the marking quality on bulk metals have been demonstrated for data matrix marks at small scales by using the dynamic nature of the device to mark groups of non-adjacent elements sequentially. This process minimises the spread of heat between adjacent elements, i.e. reduces the heat affected zone, which would otherwise reduce the resolution of the mark.

In addition to the speckle reduction technique, the application of a modified iterative Fourier transform algorithm (MIFTA) in combination with closed loop feedback by measuring the generated intensity distribution was demonstrated. This adaptive optics arrangement results in a significant increase in both the diffraction efficiency of the SLM and the uniformity of the generated intensity distribution. This further improves the quality of the marking result for laser ablation with complex beam shapes.

4.2 X10468-04 from Hamamatsu

The SLM X10468-04 manufactured by Hamamatsu is a liquid crystal on silicon device particularly optimised for modulating a wavelength of 532 nm and also optimised for increased optical power handling, e.g. by using a high reflectivity dielectric mirror. Special thanks goes to Hamamatsu Photonics, via Dr. Raymond Livingstone, for the loan of a demonstration unit for testing and evaluation purposes.

Figure 4.36: LCoS SLM X10468-04 from Hamamatsu: Controller unit and display head.

4.2.1 Device and setup

The LCoS SLM X10468-04 microdisplay works in reflection and has a SVGA resolution of 800 x 600 pixels on a display size of 16 x 12 mm (see Figure 4.36). The display is controlled via a standard DVI interface as extended display and the frame rate is 60 Hz. The SLM display uses parallel-aligned linear nematic liquid crystals (see section 2.3.4). This results in a pure phase modulation without changes of the intensity or a rotation of the polarisation state. The display has an anti-reflection coating at the front surface of the display and a high reflectivity dielectric coating at the backplane, both designed for a wavelength of 532 nm. The driving circuitry at the backplane of the display uses CMOS design with a fill factor of 95% to control the orientation of the liquid crystal layer. According the Hamamatsu, the advanced CMOS technology reduces the diffraction losses due to the pixel structure to less than 5% [110]. The X-10468-04 comes pre-calibrated for a linear phase response for a wavelength of 532 nm. The 8-bit signal from the graphics card for the available 256 grey values is transformed to a 12-bit signal after the compensation for the non-linearity [179]. The display

exhibits an inherent curvature, however, a Fresnel lens for the compensation is already available as part of the control software.

The setup for the laser machining experiments is essentially the same as described in section 4.1.4 and is shown in Figure 4.11, however, the diameter of the aperture before the SLM display was reduced to 12 mm because of the smaller display size compared to the LC-R 2500 display from Holoeye. This reduced the maximum optical average power for the tests to around 12 W. A reduction of the laser beam diameter by altering the telescope would have been ideal, but due to time constraints on the availability of the device it was not possible to carry this out. Also, the second half wave plate of the setup is rotated to align the linear polarisation of the laser relative to the display resulting in a phase only modulation for this device. The display and the controller unit of the Hamamatsu SLM are connected by two rather short and stiff data cables with is not ideal for the alignment of the display. Due to the high reflectivity dielectric coating at the backplane of the LCoS display, it is better able to cope with higher optical average powers as required for ns laser machining and no additional cooling of the display is required. The rather bulky display head including the plastic housing would not facilitate additional heat sinking. Future SLM models from Hamamatsu will have ceramic packaging allowing efficient temperature control and the connection to heat sinks and Peltier coolers [180].

4.2.2 Analysis of temporal response

The measurement and analysis of the temporal response of the SLM is carried out according to section 4.1.7. First a binary grating with a phase difference of π rad (grey values 0 and 128) was addressed constantly to the SLM while the resulting beam shape close to the focus of the setup was monitored using the high speed camera Kodak 4502m. As before, the laser repetition rate and the frame rate of the high speed camera were both set to 40.5 kHz. The laser beam had to be severely attenuated by means of a beam tap and neutral density filters. No significant and periodical temporal fluctuations of intensities of the first diffraction orders could be measured in this case (see Figure 4.37), although high frequency noise is apparent. In marked contrast to the SLM LC-R 2500 from Holoeye described in the previous paragraphs, this SLM display does not exhibit flickering (see section 4.1.7.). Additionally, no adverse effects were found in the outcome of laser machining when moving the diffracted laser beam across the work

piece by means of the scanhead with a laser power close to the ablation threshold of the metal coating on glass.

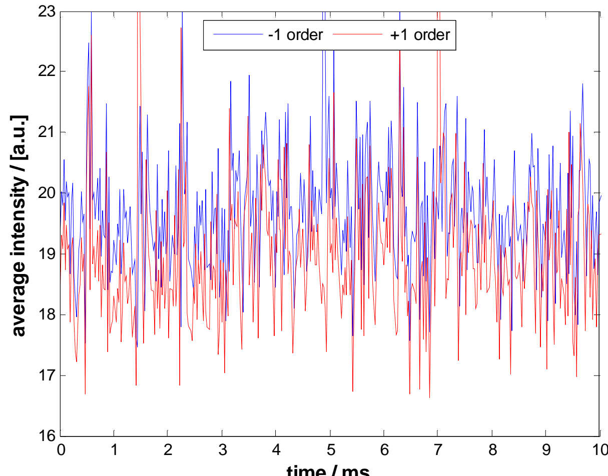

Figure 4.37: Temporal course of intensities of first diffraction orders for binary grating being addressed constantly to SLM.

According to Hamamatsu, this device is driven at a DVI frame rate of 60 Hz. To prevent flickering, a refresh rate of the liquid crystal layer with a frequency of 480 Hz and an alternate refresh rate of 240 Hz are used (see Figure 4.38, source [179]). Also, analogue driving is employed rather than the standard pulse width modulation. Theoretically, this should result in fluctuations of the phase response with a frequency of 480 Hz and a corresponding period of 2.08 ms. Such behaviour could not be confirmed with the experimental results shown in Figure 4.37.

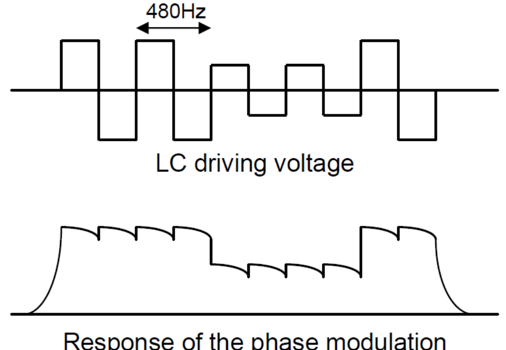

Figure 4.38: Top: driving voltage for liquid crystal layer using analogue driving at refresh rate of 480 Hz and alternating refresh rate of 240 Hz; bottom: Resulting response of phase modulation.

The temporal response for a more complex intensity distribution, in this case a "smiley face", based on a phase hologram utilising the full 256 phase levels of the SLM display is shown in Figure 4.39. The intensity distribution was generated on axis. The laser was operated at a repetition rate of 40.5 kHz, but the frame rate of the high speed camera was altered to 13.5 kHz, resulting in a larger active area of the camera to capture the increased beam shape. The zero order beam was removed in software for the evaluation. The measured average intensity of the "smiley face" exhibits non-periodic variations with a relative change of ~4% (see Figure 4.39 b). As before, the expected intensity fluctuations with a frequency of 480 Hz and a period of 2.08 ms due to the analogue driving of the Hamamatsu display cannot be detected experimentally.

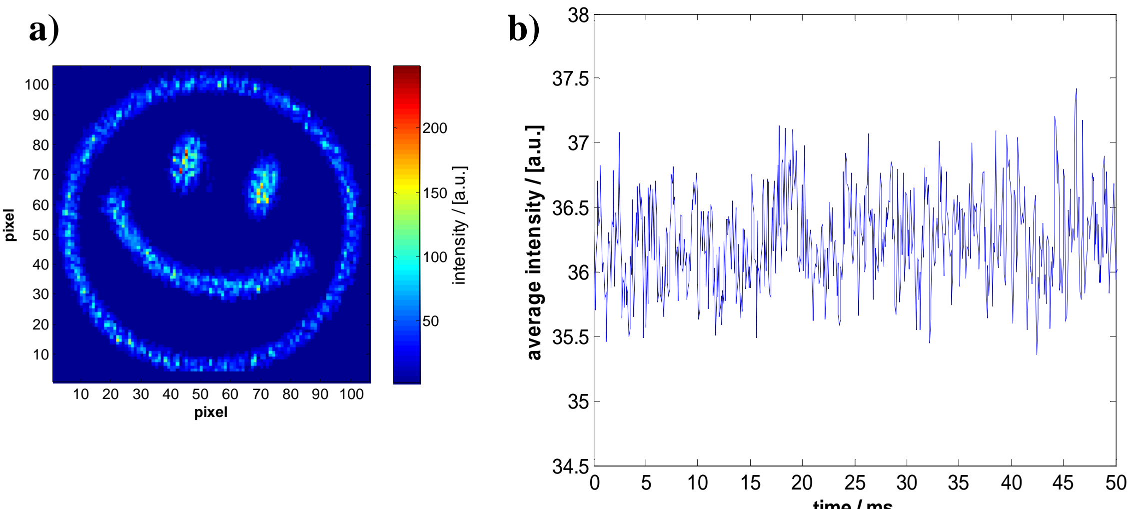

Figure 4.39: a) example intensity distribution as measured with high speed camera; b) temporal course of average intensity of "smiley face" as shown in part a).

The distinct advantage of SLM devices compared to conventional gratings or diffractive optical elements is the potential to change between different phase profiles during the actual machining process. In order to determine the response for varying or alternating phase distributions the experiments as described above were repeated using the high speed camera with a frame rate of 40.5 kHz and operating the laser at a repetition rate of 40.5 kHz. For simplicity, two binary gratings were chosen, having the same periodicity, i.e. 40 pixels, and phase difference of π rad (grey values 128 and 0) but shifted by half the periodicity relatively to each other (see section 4.1.7). These gratings, although different, generate identical spatial intensity distributions at the focus of the system and thus facilitate an easier analysis and comparison of the data from the high-speed camera. Each spot for the first diffraction orders and the zero order on the sensor had a diameter

of ~8 pixels. As a measure of the intensities of each spot, the average intensity of a 12 pixel diameter area centred on the spot is used. Figure 4.40 shows the temporal variations of the intensities of the first diffraction order when alternating or toggling between the two binary gratings with a delay time of 50 ms. During the delay time the intensities of the first diffraction are stable, though they appear fairly noisy. Once the new binary grating is addressed to the device the intensities decrease rapidly for ~6 ms and then recover exponentially to the previous level over a timescale of ~20 ms. Figure 4.40 a) shows an intensity drop of ~ 5 [a.u.] between 110 and 120 ms before the actual feature of the changing phase profile occurs. This is most likely due to a bug of the IrfanView software that was used to address the binary gratings as a slideshow on the SLM. In a further experiment, the delay time of the slideshow was reduced to zero, resulting in alternating binary gratings addressed on a single-frame basis. The behaviour of the intensities of the first diffraction order was again measured using the high-speed camera and the results are shown in Figure 4.41. The intensities do not reach a plateau in this case, unlike for the previous case with a longer delay time. The finite response time of the SLM display mainly due to the viscosity of the liquid crystal layer is the cause for this behaviour and the limiting factor for potential applications of this SLM at higher frame rates.

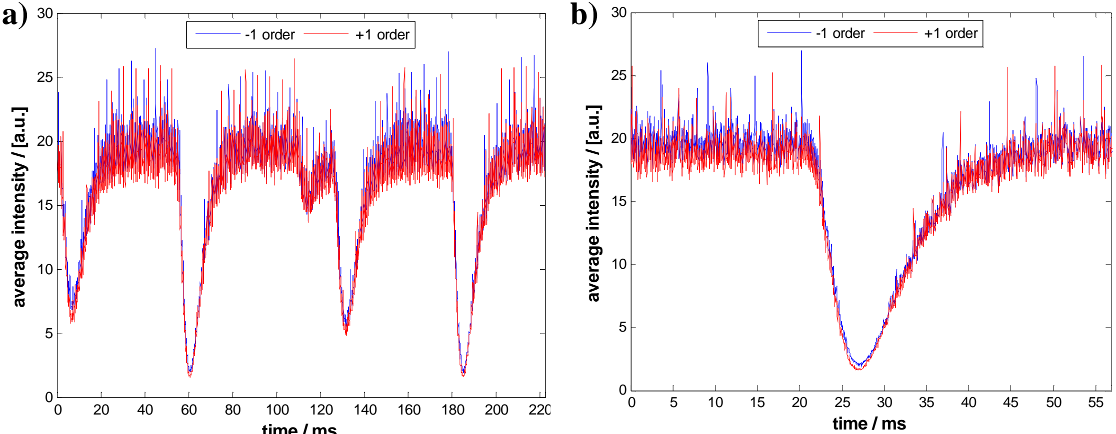

Figure 4.40: a) Average intensities of first diffraction order when addressing two similar but shifted binary gratings with phase difference of π rad alternating to SLM with a delay of 50 ms; b) zoom of response during the change.

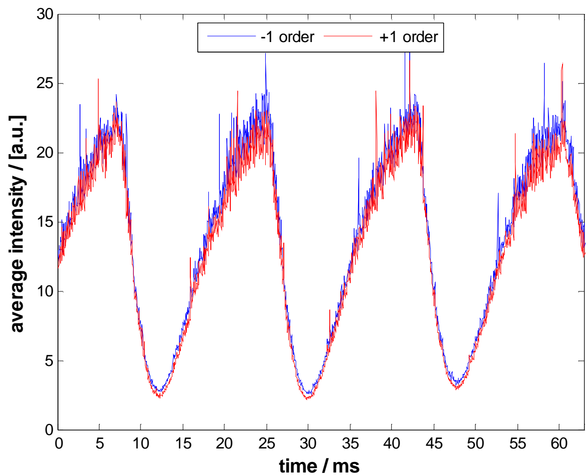

Figure 4.41: Average intensities of first diffraction order when alternating two shifted binary gratings with a phase difference of π rad on a single-frame basis.

4.2.3 Process synchronisation for 'on-the-fly' changes of beam profiles

The response time of the display when changing the phase profile addressed to the SLM strongly affects the intensity of the diffraction orders as discussed in the previous section and shown in Figure 4.41. Consequently, the intensity of the zero order beam is quite high during the actual change. This potentially has an impact on the laser machining and limits the capabilities of SLMs when dynamically changing the beam shape 'on-the-fly'. In order to determine this response time for an actual machining process, two binary gratings having a phase difference of 0.8π rad (grey values 100 and 0) but different periodicities (20 and 10 pixels) were alternately sent to the SLM (frame by frame). The angle of diffraction was thus switched on a frame by frame basis. The phase difference of 0.8π rad was chosen to emphasize the impact of the zero order beam on the laser machining process. The resulting temporal behaviour of the average intensities of the zero and first diffraction orders are shown in Figure 4.42. For simplicity, two binary gratings were used, having the same periodicity, i.e. 20 pixels, and phase difference of 0.8π rad (grey values 100 and 0) but shifted by half the periodicity relative to each other. During the change of the addressed binary gratings, the intensities of the diffraction orders drop while the zero order beam increases in intensity.

To assess the impact of these intensity variations on the laser machining, the laser beam is scanned perpendicular to the orientation of the diffraction spots at a speed of 25 mm/s across a stainless steel sample by means of the galvo scanhead while addressing the two

binary gratings with different periodicities on the SLM on a single frame basis. The laser machining outcome (laser repetition rate: 40.5 kHz, average power ~11 W) is shown in Figure 4.43 a). The outermost pairs of parallel marks correspond to the 10 pixel period grating, whilst the more closely spaced pairs of marks correspond to the 20 pixel period grating. However, there are a series of marks in the centre, in addition to the desired marks, associated with a strong zero order beam appearing periodically whenever the grating pattern being addressed to the SLM changes.

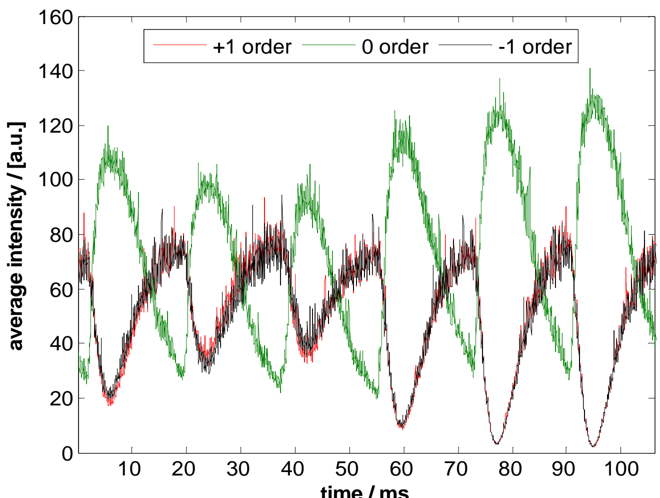

Figure 4.42: Periodic variations of intensities of zero and first diffraction orders when alternating on a single-frame basis between two similar binary gratings addressed to the SLM. The intensities of the first diffraction orders are almost identical.

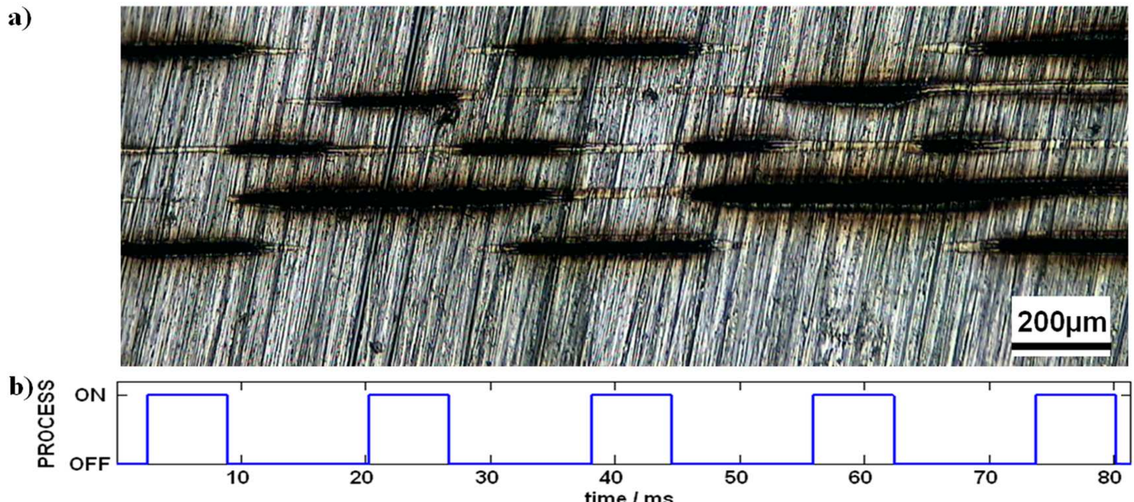

Figure 4.43: a) Machining result when alternating two binary gratings with different periodicities on the SLM on a single-frame basis while scanning the laser beam at a speed of 25 mm/s across stainless steel (scanning direction from left to right); b) schematic for process synchronization technique indicating when process is 'on' and 'off'.

As presented in section 4.1.9, the process synchronization technique can be applied in order to block the laser beam whenever its spatial intensity distribution is inappropriate for a particular laser machining application. The vertical sync signal from the graphics card is extracted and a pulse based on analysis of the intensity data shown in Figure 4.42 is generated in order to control the laser machining workstation. In this case machining is stopped whenever the intensity of the zero order exceeds that of the first diffraction orders as indicated in Figure 4.43 b). The laser machining result when using this process synchronization technique and the same laser parameters as before is shown in Figure 4.44. The deep and blackened laser marks resulting from the zero order laser beam are no longer present. Also, all the marks resulting from the first diffraction orders are of roughly the same length.

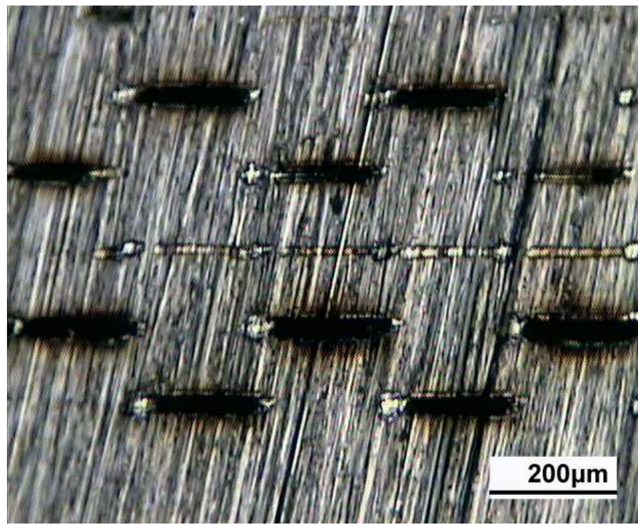

Figure 4.44: Machining results with settings as described in Figure 4.43 but utilising the process synchronization technique to remove deep and blackened marks from zero order.

4.2.4 Conclusion

Overall, the SLM X10468-04 from Hamamatsu worked very well for the application to laser beam shaping. The absence of flickering in the displayed image, the good overall efficiency (see section 4.4.3) and the device specific calibration for a wavelength of 532 nm made it well suited for application to ns micromachining. The only notable area for improvement though would be to reduce the rather bulky packaging of the display which in combination with the stiff connection cables impedes the alignment of the SLM.

4.3 A512-0532 from Boulder Nonlinear Systems

Boulder Nonlinear Systems (BNS) designs and manufactures custom liquid crystal on silicon devices tailored for specific applications and wavelengths. Their key features include high speed modulation, high optical efficiency and optical flatness. Special thanks goes to Boulder Nonlinear Systems, via Kelly Gregoriak and Anna Linnenberger, for their visit and the demonstration of the SLM A512-0532.

Figure 4.45: Display of SLM A512-0532 from Boulder Nonlinear Systems.

4.3.1 Device and setup

The SLM A512-0532 is part of the XY Nematic Series from Boulder Nonlinear Systems (see Figure 4.45), has a resolution of 512 x 512 pixels and a display size of 7.68 x 7.68 mm. The display contains linear nematic liquid crystals (see section 2.3.4). Linearly polarised light in the vertical axis relative to the display is modulated phase-only with a maximum phase stroke of 2π rad at a wavelength of 532 nm. The device comes pre-calibrated with a linear phase response for this wavelength. The cover glass of the display is coated with a broadband anti-reflection coating for wavelengths between 450 and 865 nm. A high-reflectivity dielectric coating for a wavelength of 532 nm is used at the backplane of the display. The device is controlled using a PCI-e card to ensure a faster operation of the device. Alternatively, it could be also controlled as extended display using a DVI signal from the graphics card similar to the earlier described SLM device. The refresh rate of the device is 6092 Hz to eliminate temporal fluctuations of the phase response. The maximum toggle rate when using the PCI-e interface amounts to 1015 Hz being to date the highest refresh rate for a liquid crystal on silicon spatial light modulators. Another advantage of the XY Nematic Series from

BNS is the fill factor of 100%. Typically, the reflective pixel structure of the driving electronics at the LCoS backplane acts as a grating and gives rise to unwanted diffraction. To prevent this, the gaps between the aluminium pixel electrodes are filled with dielectric layers. A planar dielectric coating is then deposited on top to eliminate optical path differences due to the underlying driving electronics (see Figure 4.46, source [181]. The dielectric coating is still sufficiently thin to minimise an attenuation of the electric field. As a result, all the reflected light by the SLM is modulated. The zero-order diffraction efficiency is stated by the manufacturer to be 61.5% [111].

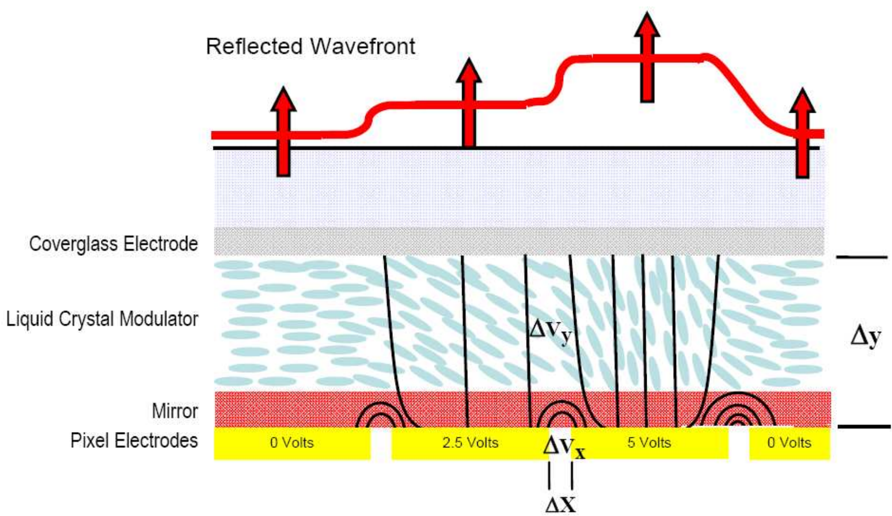

Figure 4.46: Schematic of cross section of XY Nematic Series of BNS: Planar high efficiency mirror and smoothing of the electric field eliminate most of the grating effects associated with pixelated SLMs.

The setup for the experiments with the nanosecond laser machining workstation is essentially the same as described in section 4.1.4 and shown in Figure 4.11. The display of the A512-0532 SLM comes attached to a kinematic mount facilitating easy alignment. Due to the time restriction of the availability of the demonstration unit of the SLM, the diameter of the aperture shown in Figure 4.11 was just reduced to 7 mm to avoid damage to the housing of the LCoS display. A reduction of the laser beam diameter by altering the telescope would have been ideal but it was not possible to carry out this alteration due to time constraints on the availability of the SLM device. The half wave plate was rotated to have vertically polarised light incident on the display resulting in a phase-only modulation of the linear nematic liquid crystal layer. Boulder Nonlinear Systems does not have reference values for the power handling capabilities of the SLM A512-0532 so far and suggested the average power of the light incident on the display to be limited to 3 W at a repetition rate of 40.5 kHz. At these power levels, no

actual ns laser machining experiments could be conducted and the use of higher powers was not permitted with the device on loan due to the potential risk of damage to the device.

4.3.2 Analysis of temporal response

For the measurement of the temporal response of the SLM, a binary grating with a phase difference of π rad (grey values 0 and 128, periodicity 20 pixel) was addressed constantly to the SLM while the resulting beam shape close to the focus of the setup was monitored using the high speed camera Kodak 4502m. As before the laser repetition rate and the frame rate of the high speed camera were both set to 40.5 kHz. The laser beam had to be severely attenuated by means of a polarising beam splitter controlled using a half wave plate. In addition, a beam tap and neutral density filters were used. The evaluation of the captured intensity images when addressing the binary grating constantly to the SLM is shown in Figure 4.47. Only small fluctuations of the average intensities for the first diffraction orders with a relative change of ~9% can be observed. The period of these fluctuations is 0.99 ms which can be attributed to the toggle rate of 1015 Hz as stated by the manufacturer [111]. In the context of ns laser machining with pulse repetition rates typically in the order of 10 – 100 kHz and machining times of several ms these fluctuations of the resulting intensity distribution are negligible making this device ideal for the application. The average intensity of the zero order is not shown in Figure 4.47 to emphasize the small variations of the first diffraction orders.

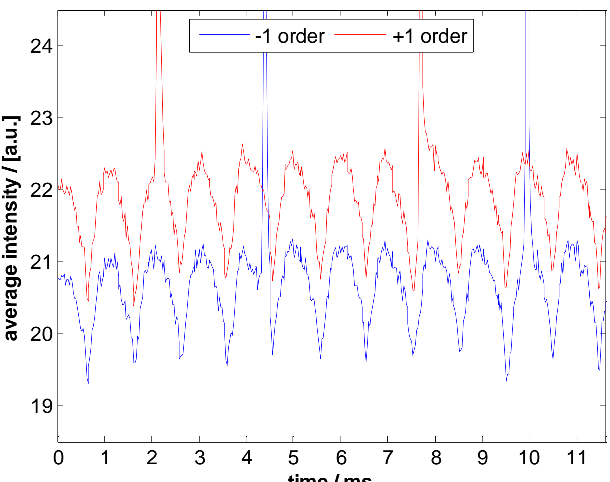

Figure 4.47: Average intensities of first diffraction orders for binary grating with phase difference of π addressed constantly to BNS SLM. The average intensity of the zero order is not shown to increase the visibility of the fluctuations of the first diffraction orders.

The experiment as described above was repeated whilst alternating between two different binary gratings with a delay time of 20 ms on the display. For simplicity, two binary gratings were chosen with the same periodicity of 20 pixels and the same phase difference of π (grey values 0 and 128) but shifted by half the periodicity relative to each other. These gratings, although different, generate identical beam shapes at the focus of the optical system and thus make it easier to analyse the data from the high-speed camera. The results (see Figure 4.48) show that, when the binary grating is addressed constantly, the average intensities of the first diffraction orders are almost constant, apart from a small high frequency flicker with a period of ~1 ms. Once the new phase profile is addressed a sudden drop of the intensities over ~1.3 ms can be observed followed by an increase of the intensities for ~5 ms until the initial level. Thus changing the phase profile by half of the available phase stroke can be achieved at a maximum frequency of 160 Hz.

The delay time of 20 ms was removed to alternate between the shifted binary gratings on a single frame basis (see Figure 4.49). In this case, the periodicity of the change amounts to 3.6 ms corresponding to a frequency of 275 Hz. Despite being the same experimental configuration and evaluation, the maximum intensity values are lower than the result shown in Figure 4.48. This indicates that display specific properties, especially the viscosity of the liquid crystal layer, are the limiting factor for the maximum frame rate of the SLM rather than the driving electronics including the PCIe controller card.

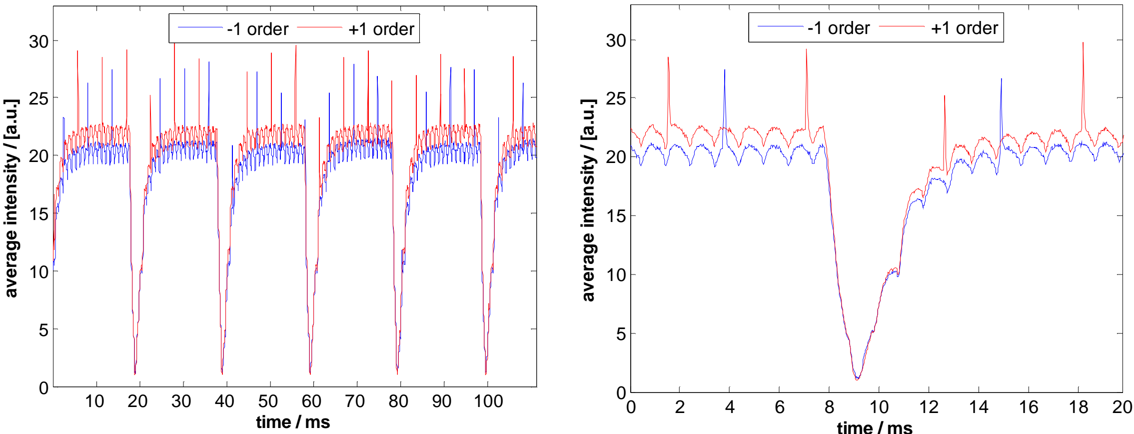

Figure 4.48: Average intensities of first diffraction orders when addressing the SLM with two alternating, similar but phase shifted (by π rad) binary gratings with a delay time of 20 ms.

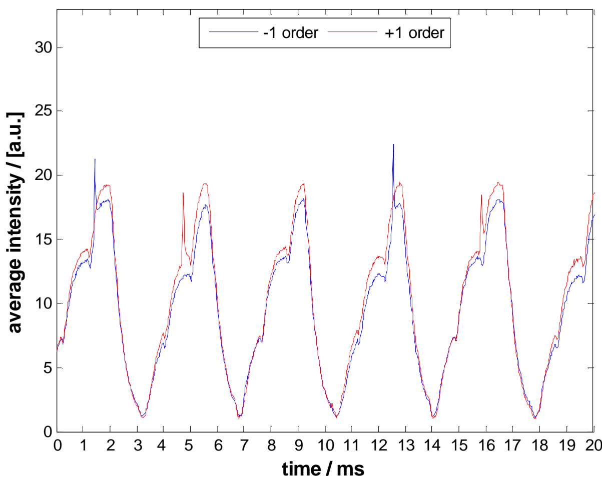

Figure 4.49: Average intensities of first diffraction orders when addressing two similar but shifted binary gratings with phase difference of π alternating to SLM on single frame basis.

4.3.3 Discussion

The SLM A512-0532 is pre-calibrated and optimised for applications with a wavelength of 532 nm. The display is attached to a kinematic mount for easy alignment. The compact display size of 7.68 x 7.68 mm facilitates an easy incorporation into laser machining workstations. In our setup the galvo scanhead has a maximum input aperture of 10 mm and therefore no additional telescope to reduce to beam diameter would be required, in contrast to the larger displays from Holoeye and Hamamatsu which were presented in sections 4.1 and 4.2. On the other hand, the resolution of the display (number of pixels) from BNS is lower than that of the other two SLMs. Furthermore, a smaller display size of the device is resulting in higher optical power densities, which potentially limits the application of the device with ns laser machining. The high electronic refresh rate suppresses any significant flickering of the display with only small variations in the order of ~9% visible in the recorded traces (see Figure 4.47). The biggest advantage of the device is the high frame rate and short response time making this device particularly competitive for laser machining process requiring 'on-the-fly" changes of the beam shape or for using the SLM in combination with adaptive feedback.

4.4 Summary and comparison of used SLM devices

4.4.1 Overview of specifications

	Holoeye LC-R 2500	Hamamatsu X10468-04	Boulder Nonlinear Systems A512-0532
Resolution:	1064 x 768 pixels	792 x 600 pixels	512 x 512 pixels
Effective display size:	19.5 x 14.6 mm	16 x 12 mm	7.68 x 7.68 mm
Pixel pitch:	19 µm	20 µm	15 µm
Liquid crystal type:	45° twisted nematic	Parallel aligned linear nematic	Parallel aligned linear nematic
Max. frame rate:	75 Hz	60 Hz	142 Hz (using PCIe card)
Refresh rate:	75 Hz	480 Hz	1015 Hz
Anti-reflection coating of cover glass:	No	Yes, for 532 nm	Yes, for 532 nm
Coating of reflective mirror:	Al (broadband)	Dielectric for 532 nm	Dielectric for 450 - 865 nm
Wavelengths:	400 – 700 nm	532 nm	532 nm
Prize (excl. VAT):	£6,882[1]	£9,500[2]	£19,137[3] (£14,885 incl. white paper)

Table 4-1: Comparison of SLM devices used in this work.

4.4.2 Temporal response

The comparison of the response of the different spatial modulators shown here is based on the experimental results described in sections 4.1.7, 4.2.2 and 4.3.2. In all cases the

[2] Quote September 2008

[3] Quote June 2008

[4] Quote October 2009

laser was operated at a frequency of 40.5 kHz while a high speed camera with the same frame rate of 40.5 kHz was located close to the focus of the optical system to measure the intensity distribution of each laser pulse modulated by means of the SLM. Two binary gratings with a phase difference of π rad but shifted by half the periodicity were addressed alternating with a certain delay time to each SLM. Although these patterns represent different phase profiles, the resulting beam shape is the same facilitating an easier evaluation of the intensity data. The results for the average intensity of the diffraction order are shown in Figure 4.50 and the change of the profiles occurs after 15 ms.

For the LC-R 2500 from Holoeye (blue line) strong periodic fluctuations of the intensity, also referred to as flickering, can be observed. The period of the flickering amounts to ~13.3 ms corresponding to the pulse width modulated signal to drive the display at a frequency of 75 Hz. Once the new phase profile is addressed to the SLM, i.e. after 15 ms, the intensity decreases over a timescale of ~16 ms and recovers to the initial value after an additional ~34 ms. This response time is caused by the viscosity of the liquid crystal layer which limits the speed of reorientation of the molecular structure.

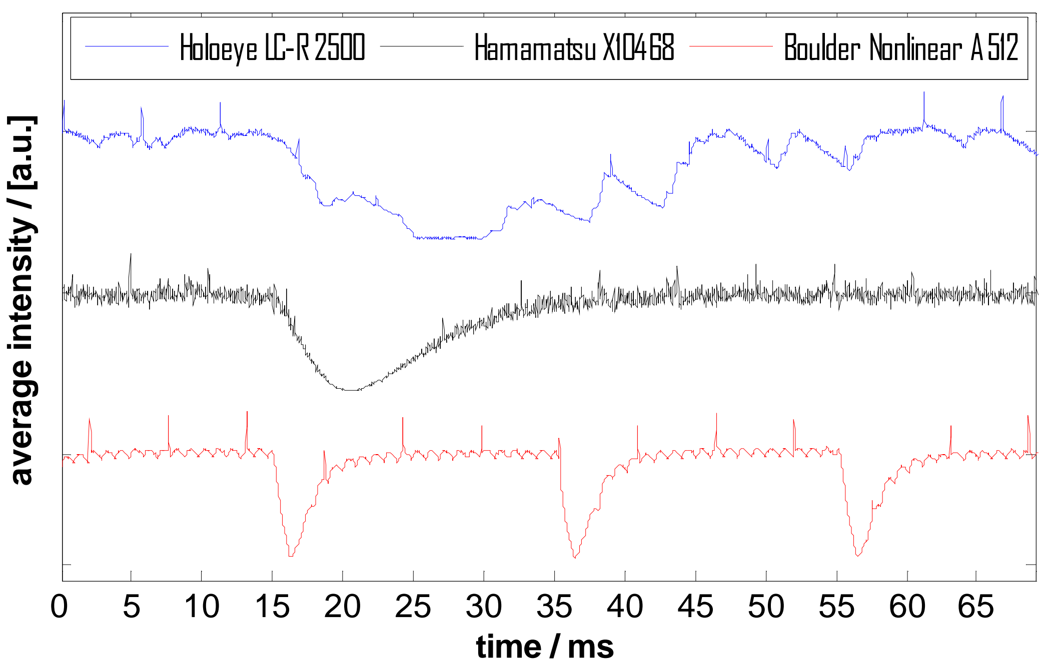

Figure 4.50: Comparison of response when alternating between similar, but shifted binary gratings with a phase difference of π rad on the SLMs. The average intensities of the first diffraction orders are displayed normalised, but with additional offset.

For the SLM X10468-4 from Hamamatsu no significant periodic flickering can be observed (see black line in Figure 4.50). Analogue driving with a frequency of 480 Hz is applied for this device to prevent the flickering. During the change of the binary gratings, the average intensity of the first diffraction order decreases for ~6 ms and increases after that for ~20 ms.

The SLM A512-0532 from Boulder Nonlinear Systems (BNS) exhibits very little flicker with a relative amplitude of ~9% and a period of ~1 ms as shown with the red line in Figure 4.50. This corresponds to the toggling frequency of 1015 Hz used for the electronic addressing of the display. The change of the phase profile occurs over ~6.3 ms, consisting of an intensity drop for ~1.3 ms and a subsequent increase for ~5 ms. This fast response with a frequency of ~160 Hz is achieved by using liquid crystals with a higher refractive index compared to conventional microdisplays [182]. Consequently the required thickness of the LC layer for the 2π phase modulation in reflection can be reduced. This results in an increased electric field across the LC layer for the same driving voltage. Hence, an increased force causes the reorientation of the LC molecules. For the BNS SLM, the delay time between the changes of the phase profiles was set to just 20 ms resulting in three changes during the observation time as shown in Figure 4.50.

4.4.3 Efficiency

The results presented in section are based on collaborative work with Dr. Jonathan Parry. In order to determine the efficiency of the three SLM displays, three measurements using a digital power meter were carried out in the setup shown in Figure 4.11:

i) after the aperture to measure the power incident on the SLM: $I_{incident}$;

ii) to measure the full laser power coming out of the galvo scanhead: I_{galvo};

iii) to measure the power in the desired diffraction image: I_{diff} (using a sheet of metal with a square aperture slightly larger than the off-axis image and aligned to allow the image through while blocking the rest of the light).

The beam shape was chosen to be a two dimensional data matrix pattern representing the letters “AOP” as before based on a kinoform with 256 phase levels. The intensity

distribution was generated off-axis to separate it from the zero order beam. The diffraction efficiency η_{diff} was defined as:

$$\eta_{diff} = \frac{I_{diff}}{I_{galvo}}; \qquad \text{Equation 4-2}$$

The overall efficiency $\eta_{overall}$ was defined as:

$$\eta_{overall} = \frac{I_{diff}}{I_{incident}}; \qquad \text{Equation 4-3}$$

The overall efficiency considers intensity losses due to the display, such as reflection losses from the cover glass or absorption of light within the display, and due to additional optics like the required telescope to reduce the beam diameter. The results are shown in Table 4-2. For the Holoeye display a phase profile with a resolution of 256 x 256 pixels has been calculated using the IFTA and tiled in a 3 x 4 pattern for addressing it to the SLM as recommended for good uniformity and diffraction efficiency [165]. The resulting diffraction efficiency is 54.7% and the overall efficiency 29.3%.

In the next step, the diameter of the aperture was reduced to 11.4 mm and a phase profile with 200 x 200 pixels was determined and tiled in a 3 x 4 pattern and addressed to the Holoeye SLM. These settings mimic the reduced resolution of the Hamamatsu SLM. As a consequence, the diffraction efficiency reduces to 50.6% and the overall efficiency stays almost the same at 28.7%. After that, the Hamamatsu display was integrated into the setup according to section 4.2.1. In this case, the diffraction efficiency increases to 55% and the overall efficiency increases to 36.7%. The diffraction efficiency is very similar to the case for the Holoeye display operated at full resolution. The overall efficiency, however, is much higher for the Hamamatsu display. This can be attributed to the anti-reflection coating of the cover glass and the increased reflectivity due to the dielectric coating for the back reflector of the display.

For the SLM from Boulder Nonlinear Systems the diffraction efficiency amounts to 60% and the overall efficiency is 39.3%. This further increase can most likely be associated with the increased fill factor of the display (see section 4.3.1).

	Holoeye LC-R 2500	Holoeye SLM with "Hamamatsu resolution"	Hamamatsu X10468-04	Boulder Nonlinear A512-0532
Resolution of phase profile:	**1024 x 768 px**	**792 x 600 px**	**792 x 600 px**	**512 x 512 px**
Tiling on display:	**3 x 4**	**3 x 4**	**3 x 4**	**4 x 4**
Intensity distribution incl. speckle reduction:				
Diffraction efficiency:	**54.7%**	**50.6%**	**55.0%**	**60.0%**
Overall efficiency:	**29.3%**	**28.7%**	**36.7%**	**39.3%**

Table 4-2: Efficiency of used spatial light modulators.

4.4.4 Suitability for laser machining

The use of an SLM for beam shaping is a powerful technique in laser machining. However, the limited power handling capabilities can prevent the application to processes requiring short pulses and high optical average powers. Cooling of the LC-R 2500 from Holoeye enables the device to be applied for beam shaping for nanosecond laser machining with a much higher average power than recommended by the manufacturer (5 W/cm^2 were demonstrated rather than the recommended 1-2 W/cm^2). Also, the inherent curvature of the display can be compensated for by means of the cooling mount. This enables direct laser marking or ablation with complex intensity distributions.

Conventional SLM displays, such as the LC-R 2500, exhibit temporal fluctuations of its phase modulation due to their electronic addressing. This flickering can have a significant adverse effect on the outcome of laser machining. A novel synchronisation

technique was introduced to compensate for this behaviour. SLM devices, designed specifically for laser wavefront modulators, such as the X10468 from Hamamatsu or the A512 from Boulder Nonlinear Systems, do not exhibit the same flickering problems as standard display devices. Nevertheless, if changes are required during the actual machining process, transition effects due to the finite response time of the liquid crystals can occur resulting in unwanted machining. Again the synchronisation technique can be utilised to prevent this.

When using an SLM for laser beam shaping, the speckled intensity distribution of the generated image is an inherent problem that limits the quality of the marking that can be achieved. However, this limitation can be overcome by utilising the dynamic nature of the SLM. Multiple beam shapes with the same amplitude but different phase can be generated with very short switching times, resulting in a significant reduction of the speckle contrast after time averaging. Sequential laser marking with these different phase distributions dramatically improves the quality of the laser marking.

The resulting intensity distribution including the speckle reduction technique can still exhibit non-uniformities which adversely affect the quality of the laser marking. A modified and improved version of the iterative Fourier transform algorithm (MIFTA), in combination with closed-loop feedback, by measuring the beam shape, results in significantly increased diffraction efficiency and an improved uniformity of the generated intensity distribution. This results in a further improvement of the quality of the laser marking in addition to the speckle reduction technique.

For laser machining processes requiring frequent changes of the beam shape, the comparatively long response time for the LC-R 2500 from Holoeye is not ideal. The X10468 from Hamamatsu and especially the A512 from Boulder Nonlinear System allow for significantly faster changes. Whilst the SLM from Hamamatsu is well suited to optical average powers required for nanosecond laser machining, no information about the power handling of the BNS device are available to date. The SLM from BNS provides the highest diffraction efficiency of the tested devices followed by the Hamamatsu and the Holoeye SLM.

In final conclusion, it was demonstrated that using an SLM in combination with an appropriate control and feedback system for beam shaping is a powerful technique which offers increased flexibility and improved process control when used in a laser machining workstation and has significant potential to be applied in an industrial process.

Chapter 5

Conclusions and future work

5.1 Conclusions

Adaptive Optics techniques were successfully applied to laser processing providing significant advantages. Beam shaping by means of Adaptive Optics gives increased flexibility and improved process control, key benefits in laser materials processing.

A piezoelectric deformable mirror was applied for beam shaping of a nanosecond (ns) and millisecond (ms) laser: For ns surface marking, shaping the Gaussian laser beam towards a square flat top profile was demonstrated to be beneficial. For ms drilling, creating a ring shape intensity distribution was shown to result in consistent through holes with better quality and significantly higher aspect ratio compared to the unmodified multimode beam.

A liquid crystal spatial light modulator (SLM) was applied, to my knowledge for the first time, to beam shaping with a high average power nanosecond laser. A heat sinking method enabled the average power handling capabilities of the device to be significantly increased, and hence complex spatial intensity distributions can be generated with sufficient intensity for direct laser marking. A process synchronisation technique was developed to overcome limitations due to fluctuations of the phase modulation and the finite response time during changes of the device. The dynamic nature of the SLM was exploited to improve the quality of laser marking by reducing the impact of the inherent speckled intensity distribution across the generated beam shape. Further improvements in the quality of laser marking with complex intensity distributions were achieved by applying a modified control algorithm and a closed loop feedback.

5.1.1 *Deformable mirrors*

Extracavity laser beam shaping has been demonstrated using a deformable mirror and closed-loop control by means of an iterative simulated annealing algorithm and an intensity measurement of the resulting intensity distribution at focus. Two different types of deformable mirrors, i.e. a piezoelectric deformable mirror and a bimorph mirror, each with 37-active elements each were tested.

The devices are robust and able to withstand laser powers suitable for laser machining. However, in both cases, the small number of active elements, the crosstalk between adjacent actuators and the stiffness of the reflective surface are the limiting factors regarding the beam shaping capabilities.

For the bimorph mirror from BAE Systems, the circular symmetry of the electrodes and the zonal response are beneficial for altering a Gaussian beam profile towards elliptically shaped laser beams with arbitrary orientation of the principal axis. There are a range of possible application areas, for example for cutting silicon wavers, where elliptical beams have been shown to be more efficient and enable higher cutting speeds compared to Gaussian beams [2, 3]. In order to achieve the highest cutting efficiency, the bimorph mirror would enable the user to align the long principal axis of the ellipse with the direction of the cut. The dynamic nature of the device would allow the dynamic adaption of the axis orientation for cutting of a circular arc. This would be impossible to achieve with conventional static optics. A further application would be to tailor the ellipticity of the beam to compensate for varying scanning speeds when using a galvo scanhead system.

The piezoelectric deformable mirror from OKO Technologies can be used as a variable homogenizer to alter a Gaussian beam towards close-to-uniform intensity distributions, i.e. circular flat top beam profiles, although the beam profile will still exhibit a fairly steep but finite slope at the circumference of the beam. Benefits when modifying an incident Gaussian intensity distribution towards a square flat top profile were demonstrated for nanosecond surface marking of stainless steel. The laser machining result with the modified flat top beam shows a more uniform surface finish and significantly reduced spatter compared to results generated with an unmodified Gaussian beam with otherwise identical laser parameters. For laser drilling, using a multimode millisecond laser machining workstation, creating a doughnut beam profile

by means of the piezoelectric deformable mirror was demonstrated to have a significant beneficial impact. Drilling holes using a doughnut shaped laser beam shape resulted in smaller diameter holes which were deeper and more uniform than those generated by the unmodified multimode beam. The resultant smaller hole diameter is remarkable, since the doughnut beam shape had a larger outer diameter than the comparable Gaussian beam; also the beam shaping result for the doughnut beam had a somewhat uneven intensity distribution due to the limitations of the device as described above. The apparently more efficient drilling process when using the doughnut beam shape indicates an improved melt ejection mechanism compared to the multimode beam. Besides the altered spatial intensity distribution of the laser by means of the deformable mirror, changes in the focal position and the lengths of the caustic are likely and their impact on the drilling result requires further investigation.

For the nanosecond laser based surface marking and millisecond laser drilling, modifying the initial laser beam towards a square flat top and a doughnut profile respectively has a significant and beneficial impact on the outcome of the laser machining process. While similar or potentially even more uniform and more complex spatial intensity distributions might be generated by other static optical components, such as refractive beam shapers [6], a deformable mirror in a closed-loop control enables dynamic modification of the beam shape and also compensation for changes in the incident laser beam profile that may result from variations of the laser parameters. The PDM can be addressed at a maximum frequency of up to 1 kHz and this enables changes in beam profile between single pulses for a millisecond laser machining workstation which is typically operating at repetition rates in the order of a few or tens of Hertz. For nanosecond laser systems the repetition rates are typically higher than the maximum frequency of the deformable mirror and thus only pulse trains with a distinct beam shape can be generated.

5.1.2 *Spatial light modulators*

In contrast to the only partially successful outcomes of adaptive beam shaping with deformable mirrors, the experiments with a spatial light modulator (SLM) demonstrated significant benefits in free form beam shaping.

It was demonstrated that cooling of the display of the spatial light modulator LC-R 2500 from Holoeye enables the device to be applied for beam shaping for nanosecond laser machining with much higher average laser powers than recommended by the manufacturer. The display was exposed to ns laser pulses with an optical power density of approximately 5 W/cm^2 over a timescale of 1 h without any damage to the SLM display and also without any significant degradation of its beam shaping characteristics. This is to my knowledge the first time that the use of an SLM has been reported in conjunction with a high average power laser operating in the ns regime. Utilizing the full resolution of the display enables the generation of complex beam shapes, such as two-dimensional data matrix patterns, with sufficient intensity for direct laser ablation. The beam shape is modified by addressing a defined phase pattern to the SLM based on the iterative Fourier transform algorithm (IFTA, [28]) for phase retrieval.

Using an SLM for beam shaping is a powerful technique in laser processing. However, a conventional SLM display with a standard pulse-width-modulated signal, such as the LC-R 2500 from Holoeye, exhibits significant temporal fluctuation of its phase modulation. This flickering was demonstrated to have an adverse effect on the outcome of short-pulsed and high-repetition rate laser machining. During the flicker period, the SLM device has a wrong or undefined phase profile and this leads to an undefined beam shape which creates unwanted machining. Two techniques were shown to reduce the impact of this inherent flickering: First, the amplitude of the flickering can be reduced by active cooling of the display; yet, it cannot be fully prevented. Secondly and more usefully, a process synchronisation technique between the laser machining workstation and the graphics card which controls the SLM was developed to inhibit the laser during periods in which the display exhibits flicker und thus prevent unwanted machining. Although SLM devices designed specifically as laser wavefront modulators, e.g. the X-10468 from Hamamatsu, do not exhibit the same flickering problems as standard display devices, if changes of the phase patterns are required during the laser processing, a transition effect can occur due to the finite response of the device, resulting in unintended machining. Again, the process synchronisation technique can be

successfully utilised to inhibit the laser beam and prevent unwanted machining while a new phase profile is addressed to the SLM display.

The speckled intensity distribution generated by means of an SLM as diffractive optical element is an inherent problem [169] associated with any diffractive optical element and the use of a coherent light source and this limits the quality of the laser marking result that can be achieved with a static phase pattern. However, the dynamic nature of the SLM can be utilized to reduce the speckle problem for laser machining tasks with longer dwell times than the response time of the device. A series of periodically shifted holograms can be generated which result in an image with identical amplitude but different phase. Since the speckle is determined by the relative phase of different sections of the modified wavefront by means of the SLM, these periodically shifted images will result in different speckle distributions. Consequently, the time-averaged image exhibits a close to uniform intensity distribution with a very low speckle contrast. For the laser processing this can be realized by sequentially marking with the shifted holograms addressed to the SLM and results in a significant improvement of the quality of the laser marks. Furthermore, when laser machining small features, such as a data-matrix pattern, on a small scale, sequential laser marking of non-adjacent elements by means of the SLM enables the spread of heat to be minimised and hence results in an improvement of the resolution of the resulting mark.

In addition to the speckle reduction technique, the application of a modified iterative Fourier transform algorithm [177, 178] in combination with a closed-loop measurement of the generated intensity was demonstrated to significantly improve the quality of the laser marking using complex beam shapes generated by an SLM and a nanosecond pulsed laser. Using a more advanced algorithm to calculate the holograms and incorporating closed-loop feedback from the actual beam shape results in an increase of the diffraction efficiency and an improvement of the uniformity of the generated intensity distribution. For laser processing applications with intensities close to the ablation threshold of the material this approach is particularly important. Such an adaptive optics technique also enables to compensate for misalignment of the optical system and for variations in the incident laser beam during the machining process.

5.2 Future work

Adaptive Optics can be beneficial for various laser-based manufacturing processes as discussed in chapters 3 and 4. However with respect to the applications of such AO techniques in industrial processes, there are still obstacles and limitations. In particular the small number of active elements and the surface constraints for the deformable mirrors pose a limit to the achievable intensity distributions.

In the case of liquid crystal spatial light modulators, the power handling capabilities and wavelengths restrictions are the most restrictive parameters.

A few approaches and suggestions for future research and development activities to address those limitations are discussed in the following sections and some of them are already under investigation.

5.2.1 Affordable deformable mirrors with more actuators

Deformable mirrors can be provided with dielectric coatings making them a robust beam shaping technique suitable for high laser powers and many different wavelengths. Deformable mirrors are able to handle much more laser power compared to liquid crystal SLMs. However, the comparatively small number of active elements and the constraints on the surface shape due to the stiffness of the deformable surface and crosstalk can clearly affect the beam shaping capabilities (see sections 3.3 and 3.4). A reduction of the thickness of the mirror substrate which would remove some of the constraints on cross-talk and surface shape can result in degraded dielectric mirror coatings. Applying a dielectric mirror coating on a thin flexible substrate can impose a surface strain to the substrate that results in a deformation.

Alpao S.A.S. offer a deformable mirror with 241 magnetic actuators [38] being significantly more than for the devices used in chapter 3. The reflective surface has a metallic coating supporting an optical energy of 400 mJ/cm² [183]. The cost of this device including driving electronics is 85,000 €[5] which makes this deformable mirror unattractive for applications for laser processing in industrial processes.

[5] Quoted: July 2010

Commercially available deformable mirror device typically have a stroke in the order of µm or even ten's of µm (see [79]). When using the wavefront modulator in a diffractive optics approach similar to the SLM, a maximum actuator stroke of half the wavelength when operating the device in reflection and assuming an initially flat device would be sufficient for the operation. For example at a wavelength of 1064 nm an actuator stroke of just 532 nm would be required. Such actuation strokes can be achieved with modern multilayer piezoelectric stacks [184] at significantly lower voltages then for example employed in the OKO device. Hence the requirements on the driving electronics could be reduced and a standard 50 V CMOS-type electronics architecture rather than multi-channel high voltage power amplifying units as for the piezoelectric deformable mirror from OKO Technologies could be used. This would dramatically reduce the cost for the device. A collaboration between the Microscale Sensors Group at the University of the West of Scotland (UWS) and the UK Astronomy Technology Centre in Edinburgh (UK ATC) is currently developing such a deformable mirror with low voltage requirements due to a multi-layer PZT technology and CMOS driving electronics.

For the application of a beam shaping technique based on a deformable mirror in combination with a galvo scanhead, a compact design of the deformable mirror with an active area ideally of the same diameter than the input aperture of the scanhead, e.g. in our case 10 mm diameter, would be desirable. This avoids the need for an additional telescope arrangement. Ultimately, in addition to an increased number of active elements a high actuator density would be also useful; however, the price of the system should be in the order of standard galvo scanhead system, i.e. approximately £10k, for it to be competitive for integration into an industrial laser machining workstation.

The fact that Adaptive Optics technology, though in a very basic approach, is already integrated in consumer electronics, such as a DVD player [37], and can nowadays be cheaply mass-produced, can be regarded as positive sign that 'affordable' deformable mirrors with a high actuator count might get available in the near future for application in laser-based manufacturing processes.

5.2.1.1 Extension sensing

When using a deformable mirror for changing the beam shape 'on-the-fly' based on previously determined and optimised actuator voltages for the desired intensity distribution, the inherent hysteresis of the piezoelectric actuators and as a consequence

the limited positioning repeatability can be a severe obstacle when operating the device open-loop. Although some of the hysteresis can be eliminated by driving the piezo actuators to a low voltage first before approaching a set voltage from always one direction. This approach may result in unwanted machining due to the finite response time of the device or leads to a significant extension in the processing time. The two deformable mirrors used in this project for example exhibit a hysteresis of 10% for the piezoelectric deformable mirror from OKO Technologies (see section 3.1.1) and smaller 5% for the bimorph mirror from BAE Systems (see section 3.1.2). This characteristic clearly affected the repeatability of a beam shape based on a particular set of actuator voltages when operating the device without closed-loop feedback.

Hence the integration of some sort of extension sensing to each actuator would be a key advantage for open-loop changes of the mirror shape and consequently the beam shape during the actual laser machining. Different approach in the time and frequency could be used to measure the extension of an actuator: The ultrasonic pulse echo response for acoustic pulses could be measured and evaluated to retrieve the changes in the actuator length [185]. Also, the frequency shift response spectrum when adding an ultrasonic transducer could be analysed [186]. Furthermore, the frequency shift in the impedance spectrum of each actuator could be measured to deduce the actual actuator length and this approach was found to be the most effective in this context [187]. This technique will be further optimised and is intended to be integrated into a high density deformable mirror for application to laser processing as part of the collaboration between UWS, UK ATC and HWU.

5.2.2 Spatial light modulators

5.2.2.1 Power handling capabilities

The SLM LC-R 2500 from Holoeye with the display attached to a copper mount for cooling has been successfully demonstrated to withstand ns laser pulses at a wavelength of 532 nm and an average power of 14.7 W over a timescale of 1 h. This corresponds to a power density of ~5 W/cm^2. Since the maximum available output power of the laser was used, a more powerful laser source and significantly more financial resources would be required to determine the actual damage threshold of the display. For the damage tests with 14.7 W average power, the copper mount was not actively cooled. As a result of the laser irradiation, the display temperature increased up to 48 °C. When

using additional water cooling improved heat removal from the display is of course achieved. Hence it is expected that the display can be maintained at similar or potentially even lower temperatures despite an increase of the average laser power. The actual damage threshold of this display including active cooling still needs to be experimentally determined. The same is true for the other two devices tested, from Hamamatsu and especially Boulder Nonlinear Systems, where the optical damage threshold has not yet been determined. With regards to an industrial application of a beam shaping technique using a liquid crystal SLM with a nanosecond or picosecond laser source, an increased available average laser power typically results in a higher throughput and a more cost-effective production. Hence increasing the power handling of the devices is certainly essential if SLMs are to be considered for the development of practical laser machining applications.

5.2.2.2 Temporal response

The response time of liquid crystal SLMs for changing the beam shape is quite slow, especially when controlled via a conventional computer graphics card, e.g. compared to piezoelectric deformable mirrors with frequencies up to 1 kHz (see section 3.1.1). For short-pulse and high-repetition rate laser processing requiring frequent changes of the beam shape, such as laser writing of complex waveguide structures [125], photo-polymerisation [9] or laser based manufacturing processes, this can be a severe limitation. However, devices from Boulder Nonlinear Systems have a refresh rate of up to 500 Hz [188] and thus are competitive in terms of speed with other types of wavefront modulators. A further increase of the refresh rate, e.g. by using liquid crystal molecules with a higher refractive index which would lead to a thinner layer would be nevertheless desirable. This would especially be of benefit for high repetition rate laser systems.

5.2.2.3 Devices for ultra-violet light

Liquid crystal SLMs typically operate at wavelengths between the near infrared and around 400 nm. For shorter wavelengths the liquid crystal layer is highly absorbing [159]. As a consequence, liquid crystal SLMs are not appropriate to modulate UV laser beams, especially at power levels required for laser processing. However, UV laser light is commonly used for laser precision machining, in particularly the 3rd harmonic frequency of an Nd:YAG at a wavelength of 355 nm. For shorter wavelengths the diffraction limited spot size decreases and the absorption typically increases, e.g. for

metals [15, 189]. Hence the ability to modify the laser wavefront in the UV spectrum and to alter the beam shape for a particular process with a high spatial resolution might be desirable. Boulder Nonlinear Systems offer a liquid crystal SLM in the near UV spectrum, optimised for a wavelength of 355 nm [190]. However, this device is currently still in a “prototype” state and damage to the display was observed for a power density of 4.5 W/cm^2 [191]. Further research and developments on different types of liquid crystals, a different alignment layer and also electrode layer with a higher transmission in the UV compared to the typically used Indium-Thin-Oxide (ITO) are required to fill the need for an SLM operating in the UV.

Digital micromirror devices (DMD) are an alternative type of wavefront modulator which were initially developed for display applications similar to liquid crystal SLMs. DMD consist of an array of microscopic tilt mirrors, typically several hundred thousands. They can be tilted in two states: One state to reflect the incident light towards the optical system and one towards a beam dump. DMDs have been used in laser based manufacturing processes for laser marking [73] and laser lithography [74]. A dielectric coating for UV laser light could be applied to each micromirror enabling the DMD to modulate high average laser powers in the UV for e.g. ns or ps laser machining workstation. Currently a project is realised within the Applied Optics and Photonics Group at Heriot-Watt University to generate complex intensity distributions by means of a DMD for laser based marking on high value components.

References

[1] D. W. Coutts, "Double-pass copper vapor laser master-oscillator power-amplifier systems: Generation of flat-top focused beams for fiber coupling and percussion drilling", Ieee Journal of Quantum Electronics **38**, 1217-1224 (2002).

[2] J. H. Morris, M. Powers, and H. Rieger, "Method and apparatus for laser ablation of a target material," US Patent 6,472,295 (2002).

[3] J. M. Bovatsek and R. S. Patel, "Highest-speed dicing of thin silicon wafers with nanosecond-pulse 355nm q-switched laser source using line-focus fluence optimization technique", in *Laser-based Micro- and Nanopackaging and Assembly IV* Proc. SPIE 7585, (2010).

[4] M. R. Taghizadeh, P. Blair, K. Balluder, A. J. Waddie, P. Rudman, and N. Ross, "Design and fabrication of diffractive elements for laser material processing applications", Optics and Lasers in Engineering **34**, 289-307 (2000).

[5] J. A. Hoffnagle and C. M. Jefferson, "Design and performance of a refractive optical system that converts a Gaussian to a flattop beam", Applied Optics **39**, 5488-5499 (2000).

[6] U. Umhofer, E. Jäger, and C. Bischoff, "Refractive and diffractive laser beam shaping optics", Laser Technik Journal **8**, 24-27 (2011).

[7] V. V. Agafonov and A. G. Safronov, "Controllable objective with deformable mirrors", Quantum Electronics **34**, 272-276 (2004).

[8] A. G. Safronov, B. Tobke, and R. Helms, "Controlling the parameters of laser technologies by means of deformable mirrors", Journal of Optical Technology **72**, 434-442 (2005).

[9] L. Kelemen, S. Valkai, and P. Ormos, "Parallel photopolymerisation with complex light patterns generated by diffractive optical elements", Opt. Express **15**, 14488-14497 (2007).

[10] Z. Kuang, W. Perrie, J. Leach, M. Sharp, S. P. Edwardson, M. Padgett, G. Dearden, and K. G. Watkins, "High throughput diffractive multi-beam femtosecond laser processing using a spatial light modulator", Appl. Surf. Sci. **255**, 2284-2289 (2008).

[11] D. Liu, Z. Kuang, S. Shang, W. Perrie, D. Karnakis, A. Kearsley, M. Knowles, S. Edwardson, G. Dearden, and K. Watkins, "Ultrafast parallel laser processing of materials for high throughput manufacturing", in *Proc. LAMP2009,* (2009).

[12] W. M. Steen and J. Mazumder, *Laser Material Processing,* 4 ed. (Springer, London, 2010).

[13] P. Schaaf, *Laser processing of materials : fundamentals, applications and developments* (Springer series in materials science, Berlin, 2010), Vol. 139.

[14] D. Bäuerle, *Laser Processing and Chemistry,* 3 ed. (Springer, Berlin, 2000).

[15] A. M. Prokhorov, V. I. Konov, I. Ursu, and I. N. Mihailescu, *Laser heating of metals* (IOP Publishing Ltd, Bristol, 1990).

[16] W. Plass, R. Maestle, K. Wittig, A. Voss, and A. Giesen, "High-resolution knife-edge laser beam profiling", Optics Communications **134**, 21-24 (1997).

[17] Ophir, "http://www.ophiropt.com/laser/spiricon-laser-beam-profiles", (2011).

[18] J. Ihlemann and K. Rubahn, "Excimer laser micro machining: fabrication and applications of dielectric masks", Applied Surface Science **154**, 587-592 (2000).

[19] M. G. Tarallo, J. Miller, J. Agresti, E. D'Ambrosio, R. DeSalvo, D. Forest, B. Lagrange, J. M. Mackowsky, C. Michel, J. L. Montorio, N. Morgado, L. Pinard, A. Remilleux, B. Simoni, and P. Willems, "Generation of a flat-top laser beam for gravitational wave detectors by means of a nonspherical Fabry-Perot resonator", Appl. Optics **46**, 6648-6654 (2007).

[20] A. Bich, J. Rieck, C. Dumouchel, S. Roth, K. J. Weible, M. Eisner, R. Voelkel, M. Zimmermann, M. Rank, M. Schmidt, R. Bitterli, N. Ramanan, P. Ruffieux, T. Scharf, W. Noell, H. P. Herzig, and N. de Rooij, "Multifunctional micro-optical elements for laser beam homogenizing and beam shaping - art. no. 68790Q", Photon Processing in Microelectronics and Photonics Vii **6879**, Q8790-Q8790 (2008).

[21] A. Laskin, "Beam Shaping? Easy!" Industrial Laser Solutions **21**, 17-19 (2006).

[22] E. Neiss, M. Flury, and J. Fontaine, "Diffractive optical elements for laser marking applications - art. no. 70032L", Optical Sensors 2008 **7003**, L32-L32 (2008).

[23] Z. Kuang, D. Liu, W. Perrie, S. Edwardson, M. Sharp, E. Fearon, G. Dearden, and K. Watkins, "Fast parallel diffractive multi-beam femtosecond laser surface micro-structuring", Appl. Surf. Sci. **255**, 6582-6588 (2009).

[24] E. R. Dufresne, G. C. Spalding, M. T. Dearing, S. A. Sheets, and D. G. Grier, "Computer-generated holographic optical tweezer arrays", Review of Scientific Instruments **72**, 1810-1816 (2001).

[25] P. H. Malyak, "2-Mirror Unobscured Optical-System for Reshaping the Irradiance Distribution of a Laser-Beam", Applied Optics **31**, 4377-4383 (1992).

[26] B. R. Frieden, "Lossless Conversion of a Plane Laser Wave to a Plane Wave of Uniform Irradiance", Applied Optics **4**, 1400-1403 (1965).

[27] R. W. Gerchberg and W. O. Saxton, "Practical Algorithm for Determination of Phase from Image and Diffraction Plane Pictures", Optik **35**, 237-246 (1972).

[28] F. Wyrowski and O. Bryngdahl, "Iterative Fourier-Transform Algorithm Applied to Computer Holography", J. Opt. Soc. Am. A: **5**, 1058-1065 (1988).

[29] V. A. Soifer, *Methods for computer design of diffractive optical elements* (Wiley, New York, US, 2002).

[30] O. Ripoll, V. Kettunen, and H. P. Herzig, "Review of iterative Fourier-transform algorithms for beam shaping applications", Opt. Eng. **43**, 2549-2556 (2004).

[31] A. J. Waddie, Heriot-Watt University (personal communication, 2011).

[32] M. J. Thomson, J. S. Liu, and M. R. Taghizadeh, "Iterative algorithm for the design of free-space diffractive optical elements for fiber coupling", Applied Optics **43**, 1996-1999 (2004).

[33] F. Wyrowski, "Iterative Quantization of Digital Amplitude Holograms", Applied Optics **28**, 3864-3870 (1989).

[34] F. Wyrowski, "Diffractive Optical-Elements - Iterative Calculation of Quantized, Blazed Phase Structures", J. Opt. Soc. Am. A-Opt. Image Sci. Vis. **7**, 961-969 (1990).

[35] H. W. Babcock, "The possibility of compensating astronomical seeing", Publ. Astro. Soc. Pac **65**, 229-236 (1953).

[36] A. Greenaway and J. Burnett, "Industrial and Medical Applications of Adaptive Optics," (Technology tracking, 2004).

[37] M. Ogasawara and M. Sato, "The Applications of a Liquid Crystal Aberration Compensator for the Optical Disc Systems", in *6th International Workshop on Adaptive Optics for Industry and Medicine,* Imperial Press, 369-375, (2007).

[38] Alpao, "http://www.alpao.fr/products_DM241.html" (2011), retrieved.

[39] P. Wnuk, C. Radzewicz, and J. S. Krasinski, "Bimorph piezo deformable mirror for femtosecond pulse shaping", Optics Express **13**, 4154-4159 (2005).

[40] D. Dayton, S. Restaino, J. Gonglewski, J. Gallegos, S. McDermott, S. Browne, S. Rogers, M. Vaidyanathan, and M. Shilko, "Laboratory and field demonstration of a low cost membrane mirror adaptive optics system", Optics Communications **176**, 339-345 (2000).

[41] T. Y. Cherezova, S. S. Chesnokov, L. N. Kaptsov, and A. V. Kudryashov, "Super-Gaussian laser intensity output formation by means of adaptive optics", Optics Communications **155**, 99-106 (1998).

[42] R. K. Tyson, *Principles of Adaptive Optics,* 3rd ed. (CRC Press, 2010).

[43] J. W. Hardy, *Adaptive Optics for Astronomical Telescopes* (Oxford University Press, 1998).

[44] S. Campbell, S. M. F. Triphan, R. El-Agmy, A. H. Greenaway, and D. T. Reid, "Direct optimization of femtosecond laser ablation using adaptive wavefront shaping", J. Opt. A: Pure Appl. Opt **9**, 1100-1104 (2007).

[45] A. Kudryashov, V. Zavalova, A. Rukosuev, A. Alexandrov, J. Sheldakova, and V. Samarkin, "Shack-Hartmann wavefront sensor and its problems", in *Photonics West,* Proc. of SPIE 7913-8, (2010).

[46] R. Ragazzoni and J. Farinato, "Sensitivity of a pyramidic wave front sensor in closed loop adaptive optics", Astron. Astrophys. **350**, L23-L26 (1999).

[47] S. Esposito, O. Feeney, and A. Riccardi, "Laboratory test of a pyramid wavefront sensor", in *Adaptive Optical Systems Technology, Pts 1 and 2,* Proc. SPIE 4007, 416-422, (2000).

[48] S. R. Chamot, C. Dainty, and S. Esposito, "Adaptive optics for ophthalmic applications using a pyramid wavefront sensor", Optics Express **14**, 518-526 (2006).

[49] R. El-Agmy, H. Bulte, A. H. Greenaway, and D. T. Reid, "Adaptive beam profile control using a simulated annealing algorithm", Optics Express **13**, 6085-6091 (2005).

[50] E. Zeek, R. Bartels, M. M. Murnane, H. C. Kapteyn, S. Backus, and G. Vdovin, "Adaptive pulse compression for transform-limited 15-fs high-energy pulse generation", Optics Letters **25**, 587-589 (2000).

[51] W. Lubeigt, G. J. Valentine, and D. Burns, "Brightness Enhancement of a Solid-State Laser Using an Intra-Cavity Deformable Mirror", in *5th International Workshop on Apaptive Optics for Industry and Medicine,* Proc of SPIE 6018, I180-I180, (2005).

[52] M. L. Plett, P. R. Barbier, and D. W. Rush, "Compact adaptive optical system based on blind optimization and a micromachined membrane deformable mirror", Applied Optics **40**, 327-330 (2001).

[53] M. A. Vorontsov, G. W. Carhart, D. V. Pruidze, J. C. Ricklin, and D. G. Voelz, "Adaptive imaging system for phase-distorted extended source and multiple-distance objects", Applied Optics **36**, 3319-3328 (1997).

[54] N. A. Vorontsov, "Decoupled stochastic parallel gradient descent optimization for adaptive optics: Integrated approach for wave-front sensor information fusion", J. Opt. Soc. Am. A-Opt. Image Sci. Vis. **19**, 356-368 (2002).

[55] A. Alexandrov, A. Kudryashov, A. Rukosuev, V. Samarkin, and V. Zavalova, "Beam corrections in high intense lasers", in *8th International Conference on Laser and Fiber-Optical Networks Modeling,* IEEE, 344-347, (2006).

[56] J. A. Nelder and R. Mead, "A simplex method for function minimisation", Computer Journal **7**, 308-313 (1965).

[57] M. Booth, "Wave front sensor-less adaptive optics: a model-based approach using sphere packings", Opt. Express **14**, 1339-1352 (2006).

[58] M. J. Booth, "Wavefront sensorless adaptive optics for large aberrations", Opt. Lett. **32**, 5-7 (2007).

[59] D. Bertsimas and J. Tsitsiklis, "Simulated Annealing", Statistical Science **8**, 10-15 (1993).

[60] S. Zommer, E. N. Ribak, S. G. Lipson, and J. Adler, "Simulated annealing in ocular adaptive optics", Optics Letters **31**, 939-941 (2006).

[61] O. Albert, L. Sherman, G. Mourou, T. B. Norris, and G. Vdovin, "Smart microscope: an adaptive optics learning system for aberration correction in multiphoton confocal microscopy", Optics Letters **25**, 52-54 (2000).

[62] P. Yang, Y. Liu, W. Yang, M. W. Ao, B. Xu, and W. H. Jiang, "Adaptive laser beam shaping using a genetic algorithm", in *International Conference on Mechatronics and Automation, Vols I-V, Conference Proceedings,* IEEE, 2906-2910, (2007).

[63] D. S. Weile and E. Michielssen, "Genetic algorithm optimization applied to electromagnetics: A review", IEEE, Transactions on Antennas and Propagation **45**, 343-353 (1997).

[64] K. Nemoto, T. Nayuki, T. Fujii, N. Goto, and Y. Kanai, "Optimum control of the laser beam intensity profile with a deformable mirror", Applied Optics **36**, 7689-7695 (1997).

[65] C. Cheng, Y. W. Ma, and S. L. He, "Optimization of a sealed-off CO2 laser resonator by utilizing a genetic algorithm", Optics and Laser Technology **33**, 601-604 (2001).

[66] OKO Technologies, *Adaptive Optics - Product Guide* (2006), Vol. 2nd edition.

[67] A. G. Safronov, "Bimorph adaptive optics: elements, technology and design principles", in *Proc. of Conference on Design and Engineering of Optical Systems,* SPIE 2774, 494-504, (1994).

[68] O. B. Vyskubenko, P. I. Kapustin, I. S. Kolokolov, V. I. Masychev, and A. G. Safronov, "Application of deformable mirrors in industrial CO2 lasers. I. A mirror with a controllable curvature of the reflecting surface", Quantum Electronics **33**, 547-552 (2003).

[69] B. S. Vinevich, V. M. Zharikov, and A. G. Safronov, "Cooled and uncooled single-channel deformable mirrors for industrial laser systems", Quantum Electronics **28**, 366-369 (1998).

[70] E. Dalimier and C. Dainty, "Comparative analysis of deformable mirrors for ocular adaptive optics", Optics Express **13**, 4275-4285 (2005).

[71] B. S. Vinevich, L. N. Evdokimovich, A. G. Safronov, and S. N. Smirnov, "Application of deformable mirrors in industrial CO2 lasers. II. Intracavity power control and repetitively pulsed modulation of output radiation", Quantum Electronics **34**, 333-340 (2004).

[72] M. S. Griffith, L. C. Laycock, N. Archer, R. Myers, P. Doel, and R. Birch, "Progress on the Development of a Zonal Bimorph Deformable Mirror", in *Adaptive Optics Systems, Pts 1-3,* Proceedings of the Society of Photo-Optical Instrumentation Engineers (Spie) Spie-Int Soc Optical Engineering 7015, (2008).

[73] I. Murokh, A. Kerner, and S. Filatov, "Laser marking using a digital micro-mirror device", US patent 6,836,284 (2004).

[74] E. T. Ritschdorff and J. B. Shear, "Multiphoton lithography using a high-repetition rate microchip laser", Anal. Chem **82**, 8733-8737 (2010).

[75] M. J. Booth, "Adaptive optics in microscopy", Philos. Trans. R. Soc. A-Math. Phys. Eng. Sci. **365**, 2829-2843 (2007).

[76] M. Glanc, E. Gendron, F. Lacombe, D. Lafaille, J. F. Le Gargasson, and P. Lena, "Towards wide-field retinal imaging with adaptive optics", Optics Communications **230**, 225-238 (2004).

[77] P. A. Piers, S. Manzanera, P. M. Prieto, N. Gorceix, and P. Artal, "Use of adaptive optics to determine the optimal ocular spherical aberration", Journal of Cataract and Refractive Surgery **33**, 1721-1726 (2007).

[78] E. J. Fernandez, L. Vabre, B. Hermann, A. Unterhuber, B. Povazay, and W. Drexler, "Adaptive optics with a magnetic deformable mirror: applications in the human eye", Optics Express **14**, 8900-8917 (2006).

[79] N. Devaney, E. Dalimier, T. Farrell, D. Coburn, R. Mackey, D. Mackey, F. Laurent, E. Daly, and C. Dainty, "Correction of ocular and atmospheric wavefronts: a comparison of the performance of various deformable mirrors", Applied Optics **47**, 6550-6562 (2008).

[80] A. G. Safronov, "RF Patent on Application No. 2000125503," (2000).

[81] I. S. Beluga, B. S. Vinevich, and L. A. Kolosovskaya, "Distortion of a Gaussian-Beam by the Thermal Lens Arising in Optical-Elements", Optika I Spektroskopiya **50**, 541-545 (1981).

[82] V. G. Taranenko and O. I. Shanin, *Adaptive Optics (Adaptivnaya optika),* (Izdatel'stvo Radio i Sviaz', Moscow, 1990).

[83] W. Lubeigt, G. Valentine, J. Girkin, E. Bente, and D. Burns, "Active transverse mode control and optimisation of an all-solid-state laser using an intracavity adaptive-optic mirror", Optics Express **10**, 550-555 (2002).

[84] J. Beedell, I. Elder, and D. P. Hand, "Performance of a deformable mirror in a high-energy Nd:YAG laser ", in *Acquisition, Tracking, Pointing, and Laser Systems Technologies XXIII,* Proc. SPIE 7338, 733805-733809, (2009).

[85] W. Lubeigt, G. Valentine, and D. Burns, "Enhancement of laser performance using an intracavity deformable membrane mirror", Optics Express **16**, 10943-10955 (2008).

[86] W. Lubeigt, M. Griffith, L. Laycock, and D. Burns, "Reduction of the time-to-full-brightness in solid-state lasers using intra-cavity adaptive optics", Optics Express **17**, 12057-12069 (2009).

[87] N. K. Metzger, W. Lubeigt, D. Burns, M. Griffith, L. Laycock, A. A. Lagatsky, C. T. A. Brown, and W. Sibbett, "Ultrashort-pulse laser with an intracavity phase shaping element", Optics Express **18**, 8123-8134 (2010).

[88] H. Haferkamp and D. Seebaum, "Beam Delivery by Adaptive optics for Material Processing Applications Applications using High Power CO2 Lasers", SPIE **2207**, 156-164 (1994).

[89] Z. G. Cheng, Z. P. Zhang, and J. Q. Zhu, "Self-adaptive optical systems for long-distance flying optics", Applied Optics **45**, 4428-4432 (2006).

[90] Q. Zhao, Z. G. Cheng, H. Gao, X. Chai, and H. Luo, "Controlling the Focal Length and the Spot Size in Flying Optics by Dual/deformable-mirror-systems", Chinese Journal of Lasers **11**, 183-188 (2002).

[91] K. Bar, B. Freisleben, C. Kozlik, and R. Schmiedl, "Adaptive Optics for Industrial Co2-Laser Systems", Lasers in Engineering **4**, 233-242 (1995).

[92] P. Hoffmann, M. Schuberth, M. Geiger, and C. Kozlik, "Process optimizing adaptive optics for beam delivery of high power CO2 lasers", Proc. SPIE **1834**, 195 (1993).

[93] M. Geiger, M. Schuberth, and J. Hutfless, "Process optimizing CO2 laser beam using adaptive optics", Schweissen und Schneiden '94, DVS Berichte (1994).

[94] O. Boyko, T. A. Planchon, P. Mercere, C. Valentin, and P. Balcou, "Adaptive shaping of a focused intense laser beam into a doughnut mode", Optics Communications **246**, 131-140 (2005).

[95] J. Beeckman, K. Neyts, and P. Vanbrabant, J. M., "Liquid-crystal photonic applications", Opt. Eng. **50**, 081202 (2011).

[96] E. Hecht, *Optics,* 4 ed. (Addison Wesley, San Francisco, US, 2002).

[97] J. W. Goodman, *Introduction to Fourier Optics,* 3 ed. (Roberts & Company, Colorado, US, 2005).

[98] E. Lueder, *Liquid Crystal Display,* 2nd ed. (John Wiley and Sons, Ltd., West Sussex, 2010).

[99] E. G. van Putten, I. M. Vellekoop, and A. P. Mosk, "Spatial amplitude and phase modulation using commercial twisted nematic LCDs", Applied Optics **47**, 2076-2081 (2008).

[100] Philips Components, "0.97" XGA Monochrome Reflective Liquid Crystal Display", (2001).

[101] P. Yeh and G. Claire, *Optics of liquid crystal displays,* 10th ed. (John Wiley & Sons, Inc., New York, 1999).

[102] J. H. Lee, D. N. Liu, and S. T. Wu, *Introduction to flat panel displays,* 1 ed. (John Wiley & Sons Ltd., 2008), Vol. 1.

[103] J. Andilla, E. Martin-Badosa, and S. Vallmitjana, "Prediction of phase-mostly modulation for holographic optical tweezers", Optics Communications **281**, 3786-3791 (2008).

[104] M. Reicherter, S. Zwick, T. Haist, C. Kohler, H. Tiziani, and W. Osten, "Fast digital hologram generation and adaptive force measurement in liquid-crystal-display-based holographic tweezers", Applied Optics **45**, 888-896 (2006).

[105] C. Kohler, X. Schwab, and W. Osten, "Optimally tuned spatial light modulators for digital holography", Applied Optics **45**, 960-967 (2006).

[106] I. Moreno, P. Velasquez, C. R. Fernandez-Pousa, and M. M. Sanchez-Lopez, "Jones matrix method for predicting and optimizing the optical modulation properties of a liquid-crystal display", Journal of Applied Physics **94**, 3697-3702 (2003).

[107] D. R. Burnham and D. McGloin, "Holographic optical trapping of aerosol droplets", Optics Express **14**, 4175-4181 (2006).

[108] D. Cojoc, S. Cabrini, E. Ferrari, R. Malureanu, M. B. Danailov, and E. Di Fabrizio, "Dynamic multiple optical trapping by means of diffractive optical elements", Microelectron. Eng. **73-4**, 927-932 (2004).

[109] S. C. Chapin, V. Germain, and E. R. Dufresne, "Automated trapping, assembly, and sorting with holographic optical tweezers", Optics Express **14**, 13095-13100 (2006).

[110] Hamamatsu, "LCOS-SLM X10468 series," (Hamamatsu Photonics UK Limited, 2009).

[111] BNS, "Spatial Light Modulators XY Series - Complete, all-in-one system," (Boulder Nonlinear Systems, Inc, 2009).

[112] V. Laude, "Twisted-nematic liquid-crystal pixelated active lens", Opt. Commun. **153**, 134-152 (1998).

[113] P. Valley, D. L. Mathine, M. R. Dodge, J. Schwiegerling, G. Peyman, and N. Peyghambarian, "Tunable-focus flat liquid-crystal diffractive lens", Optics Letters **35**, 336-338 (2010).

[114] H. W. Ren and S. T. Wu, "Tunable electronic lens using a gradient polymer network liquid crystal", Applied Physics Letters **82**, 22-24 (2003).

[115] N. Fraval and J. L. d. B. de la Tocnaye, "Low aberrations symmetrical adaptive modal liquid crystal lens with short focal lengths", Applied Optics **49**, 2778-2783 (2010).

[116] A. R. Nabeel, S. Mumtaz, W.-W. Grady, and G. K. Pieter, "Demonstration of three-dimensional optical imaging using a confocal microscope based on a liquid-crystal electronic lens", Opt. Eng. **47**, 063201 (2008).

[117] P. F. McManamon, E. A. Watson, T. A. Dorschner, and L. J. Barnes, "Applications Look at the Use of Liquid-Crystal Writable Gratings for Steering Passive Radiation", Opt. Eng. **32**, 2657-2664 (1993).

[118] D. P. Resler, D. S. Hobbs, R. C. Sharp, L. J. Friedman, and T. A. Dorschner, "High-efficiency liquid-crystal optical phased-array beam steering", Optics Letters **21**, 689-691 (1996).

[119] R. M. Matic, "Blazed Phase Liquid-Crystal Beam-Steering", in *Conference on Laser Beam Propagation and Control,* Proc. SPIE 2120, 194-205, (1994).

[120] P. J. M. Vanbrabant, J. Beeckman, K. Neyts, E. Willman, and F. A. Fernandez, "Diffraction and fringing field effects in small pixel liquid crystal devices with homeotropic alignment", Journal of Applied Physics **108**(2010).

[121] P. F. McManamon, P. J. Bos, M. J. Escuti, J. Heikenfeld, S. Serati, H. Xie, and E. A. Watson, "A Review of Phased Array Steering for Narrow-Band Electrooptical Systems", Proc. IEEE, **97**, 1078-1096 (2009).

[122] K. D. Wulff, D. G. Cole, R. L. Clark, R. DiLeonardo, J. Leach, J. Cooper, G. Gibson, and M. J. Padgett, "Aberration correction in holographic optical tweezers", Opt. Express **14**, 4169-4174 (2006).

[123] E. Martin-Badosa, M. Montes-Usategui, A. Carnicer, J. Andilla, E. Pleguezuelos, and I. Juvells, "Design strategies for optimizing holographic optical tweezers set-ups", J. Opt. A: Pure Appl. Opt **9**, S267-S277 (2007).

[124] A. Ashkin, J. M. Dziedzic, J. E. Bjorkholm, and S. Chu, "Observation of a Single-Beam Gradient Force Optical Trap for Dielectric Particles", Optics Letters **11**, 288-290 (1986).

[125] M. Pospiech, M. Emons, A. Steinmann, G. Palmer, R. Osellame, N. Bellini, G. Cerullo, and U. Morgner, "Double waveguide couplers produced by simultaneous femtosecond writing", Optics Express **17**, 3555-3563 (2009).

[126] A. Jesacher, G. D. Marshall, T. Wilson, and M. J. Booth, "Adaptive optics for direct laser writing with plasma emission aberration sensing", Optics Express **18**, 656-661 (2010).

[127] S.-W. Bahk, E. Fess, B. E. Kruschwitz, and J. D. Zuegel, "A high-resolution, adaptive beam-shaping system for high-power lasers", Opt. Express **18**, 9151-9163 (2010).

[128] A. Bertsch, S. Zissi, J. Y. Jezequel, S. Corbel, and J. C. Andre, "Microstereophotolithography using a liquid crystal display as dynamic mask-generator", Microsyst. Technol. **3**, 42-47 (1997).

[129] C. Bay, N. Huebner, J. Freeman, and T. Wilkinson, "Maskless photolithography via holographic optical projection", Optics Letters **35**, 2230-2232 (2010).

[130] K. Obata, J. Koch, U. Hinze, and B. N. Chichkov, "Multi-focus two-photon polymerization technique based on individually controlled phase modulation", Optics Express **18**, 17193-17200 (2010).

[131] N. Sanner, N. Huot, E. Audouard, C. Larat, J. P. Huignard, and B. Loiseaux, "Programmable focal spot shaping of amplified femtosecond laser pulses", Optics Letters **30**, 1479-1481 (2005).

[132] N. Sanner, N. Huot, E. Audouard, C. Larat, P. Laporte, and J. P. Huignard, "100-kHz diffraction-limited femtosecond laser micromachining", Applied Physics B-Lasers and Optics **80**, 27-30 (2005).

[133] N. Sanner, N. Huot, E. Audouard, C. Larat, and J. P. Huignard, "Direct ultrafast laser micro-structuring of materials using programmable beam shaping", Optics and Lasers in Engineering **45**, 737-741 (2007).

[134] C. Mauclair, A. Mermillod-Blondin, N. Huot, E. Audouard, and R. Stoian, "Ultrafast laser writing of homogeneous longitudinal waveguides in glasses using dynamic wavefront correction", Optics Express **16**, 5481-5492 (2008).

[135] G. Raciukaitis, E. Stankevicius, P. Gecys, M. Gedvilas, C. Bischoff, E. Jager, U. Umhofer, and F. Volklein, "Laser Processing by Using Diffractive Optical Laser Beam Shaping Technique", J. Laser Micro Nanoeng. **6**, 37-43 (2011).

[136] J. P. Parry, R. J. Beck, N. J. Weston, J. D. Shephard, and D. P. Hand, "Application of adaptive optics to laser micromachining", in Proc. ICALEO (2010).

[137] http://www.okotech.com/catalogue.

[138] Oko Technologies, "37 (19) - channel piezoelectric deformable mirror system technical passport," in *Technical passport,* (2007).

[139] BAE Systems, "INCAO Final Mirror Edition 01 - Technical Passport," (2008).

[140] I. Elder, D. Legge, and J. Beedell, "End-pumped Q-switched Nd : YVO4 laser - art. no. 639705", Technologies for Optical Countermeasures III **6397**, 39705-39705 (2006).

[141] G. Stoilov and T. Dragostinov, "Phase-stepping interferometry: Five-frame algorithm with an arbitrary step", Opt. Lasers Eng. **28**, 61-69 (1997).

[142] X. E. Xu, L. Z. Cai, Y. R. Wang, X. E. Meng, W. J. Sun, H. Zhang, X. C. Cheng, G. Y. Dong, and X. X. Shen, "Simple direct extraction of unknown phase shift and wavefront reconstruction in generalized phase-shifting interferometry: algorithm and experiments", Optics Letters **33**, 776-778 (2008).

[143] J. Novak, *Methods for 2-D phase unwrapping in MATLAB* (Matlab, Prag, 2001).

[144] H. A. Zebker and Y. P. Lu, "Phase unwrapping algorithms for radar interferometry: Residue-cut, least-squares, and synthesis algorithms", J. Opt. Soc. Am. A-Opt. Image Sci. Vis. **15**, 586-598 (1998).

[145] J. H. Bruning, D. R. Herriott, J. E. Gallaghe, D. P. Rosenfel, A. D. White, and D. J. Brangacc, "Digital Wavefront Measuring Interferometer for Testing Optical Surfaces and Lenses", Applied Optics **13**, 2693-2703 (1974).

[146] R. Schodel, A. Nicolaus, and G. Bonsch, "Phase-stepping interferometry: methods for reducing errors caused by camera nonlinearities", Applied Optics **41**, 55-63 (2002).

[147] G. Lai and T. Yatagai, "Generalized Phase-Shifting Interferometry", J. Opt. Soc. Am. A-Opt. Image Sci. Vis. **8**, 822-827 (1991).

[148] G. D. Lassahn, J. K. Lassahn, P. L. Taylor, and V. A. Deason, "Multiphase Fringe Analysis with Unknown Phase-Shifts", Opt. Eng. **33**, 2039-2044 (1994).

[149] J. M. Huntley and H. Saldner, "Temporal Phase-Unwrapping Algorithm for Automated Interferogram Analysis", Applied Optics **32**, 3047-3052 (1993).

[150] K. H. Kudielka, Y. Hayano, W. Klaus, K. Araki, Y. Arimoto, and J. Uchida, "Low-order adaptive optics system for free-space lasercom: design and performance analysis ", in *Proc. of 2nd international workshop on adaptive optics for industry and medicine,* 364-369, (2000).

[151] K. H. Press, S. A. Teukolsky, W. T. Vetterling, and B. P. Flannery, *Numerical Recipes,* 2nd ed. (Cambridge University Press, Cambridge, 1997).

[152] P. Salamon, P. Sibani, and R. Frost, *Facts, Conjectures, and Improvements for Simulated Annealing* (Siam, Philadelphia, 2002).

[153] J. L. Chaloupka and D. D. Meyerhofer, "Observation of electron trapping in an intense laser beam", Physical Review Letters **83**, 4538-4541 (1999).

[154] J. L. Chaloupka and D. D. Meyerhofer, "Characterization of a tunable, single-beam ponderomotive-optical trap", Journal of the Optical Society of America B-Optical Physics **17**, 713-722 (2000).

[155] M. Polin, K. Ladavac, S. H. Lee, Y. Roichman, and D. G. Grier, "Optimized holographic optical traps", Optics Express **13**, 5831-5845 (2005).

[156] P. M. Prieto, E. J. Fernandez, S. Manzanera, and P. Artal, "Adaptive optics with a programmable phase modulator: applications in the human eye", Opt. Express **12**, 4059-4071 (2004).

[157] Holoeye Photonics AG, " http://www.holoeye.com/spatial_light_modulator_lc_r_2500.html".

[158] S. Osten, HOLOEYE Photonics AG, Berlin (personal communication, 2010).

[159] S. T. Wu, "Absorption measurements of liquid crystals in the ultraviolet, visible, and infrared", Journal of Applied Physics **84**, 4462-4465 (1998).

[160] CoolLaboratory, "http://www.coollaboratory.com/en/products/liquid-metalpad/".

[161] J. Oton, P. Ambs, M. S. Millan, and E. Perez-Cabre, "Multipoint phase calibration for improved compensation of inherent wavefront distortion in parallel aligned liquid crystal on silicon displays", Appl. Optics **46**, 5667-5679 (2007).

[162] E. Billauer, "http://www.billauer.co.il/peakdet.html", (2008).

[163] A. Lizana, I. Moreno, A. Marquez, C. Iemmi, E. Fernandez, J. Campos, and M. J. Yzuel, "Time fluctuations of the phase modulation in a liquid crystal on silicon display: characterization and effects in diffractive optics", Opt. Express **16**, 16711-16722 (2008).

[164] A. Hermerschmidt, S. Osten, S. Krüger, and T. Blümel, "Wave front generation using a phase-only modulating liquid-crystalbased micro-display with HDTV resolution", in *Conference on Adaptive Optics for Laser Systems and Other Applications,* Proc. SPIE 6584, E5840, (2007).

[165] J. S. Liu, N. Collings, W. A. Crossland, D. P. Chu, A. Waddie, and M. R. Taghizadeh, "Simulation and experiment on generation of an arbitrary array of intense spots by a tiled hologram", J. Opt. **12**, 085402 (2010).

[166] D. Palima and V. R. Daria, "Holographic projection of arbitrary light patterns with a suppressed zero-order beam", Applied Optics **46**, 4197-4201 (2007).

[167] A. Lizana, A. Marquez, I. Moreno, C. Iemmi, J. Campos, and M. J. Yzuel, "Wavelength dependence of polarimetric and phase-shift characterization of a liquid crystal on silicon display", J. Eur. Opt. Soc.-Rapid Publ. **3**(2008).

[168] J. R. Moore, N. Collings, W. A. Crossland, A. B. Davey, M. Evans, A. M. Jeziorska, M. Komarcevic, R. J. Parker, T. D. Wilkinson, and H. Xu, "The Silicon Backplane Design for an LCOS Polarization-Insensitive Phase Hologram SLM", IEEE Photon. Technol. Lett. **20**, 60-62 (2008).

[169] H. Aagedal, M. Schmid, S. Teiwes, and F. Wyrowski, "Theory of speckles in diffractive optics and its application to beam shaping", J. Mod. Opt. **43**, 1409-1421 (1996).

[170] H. Aagedal, F. Wyrowski, and H. Schmid, *Diffractive Optics for Industrial and Commercial Applications* (Wiley-VCH, Berlin, 1997).

[171] J. Amako, H. Miura, and T. Sonehara, "Speckle-Noise Reduction on Kinoform Reconstruction Using a Phase-Only Spatial Light-Modulator", Applied Optics **34**, 3165-3171 (1995).

[172] E. Buckley, "Invited paper: Holographic laser projection technology," in *2008 Sid International Symposium, Digest of Technical Papers, Vol Xxxix, Books I-Iii* (Soc Information Display, Playa Del Rey, 2008), pp. 1074-1079.

[173] J. W. Goodman, "Some Fundamental Properties of Speckle", Journal of the Optical Society of America **66**, 1145-1150 (1976).

[174] L. Golan and S. Shoham, "Speckle elimination using shift-averaging in high-rate holographic projection", Optics Express **17**, 1330-1339 (2009).

[175] "http://www.2dtg.com/decode.html".

[176] I. M. Barton, "Diffractive optical elements in the scalar domain," (Heriot-Watt University, Edinburgh, 1998).

[177] J. S. Liu and M. R. Taghizadeh, "Iterative algorithm for the design of diffractive phase elements for laser beam shaping", Optics Letters **27**, 1463-1465 (2002).

[178] J. S. Liu, M. Thomson, A. J. Waddie, and M. R. Taghizadeh, "Design of diffractive optical elements for high-power laser applications", Opt. Eng. **43**, 2541-2548 (2004).

[179] Hamamatsu, "LCOS-SLM X10448 series - LC driving system," (Hamamatsu Photonics UK Limited, 2010).

[180] R. Livingstone, Hamamatsu Photonics UK Limited (personal communication, 2010).

[181] BNS, "100% Fill Factor - White Paper," (Boulder Nonlinear Systems, Inc, 2008).

[182] A. Linnenberger, Boulder Nonlinear Systems (personal communication, 2010).

[183] F. Rooms, ALPAO S.A.S (personal communication, 2010).

[184] http://www.noliac.com/.

[185] D. K. Hsu and M. S. Hughes, "Simultaneous Ultrasonic Velocity and Sample Thickness Measurement and Application in Composites", J. Acoust. Soc. Am. **92**, 669-675 (1992).

[186] M. Al Ahmad and H. N. Alshareef, "A Capacitance-Based Methodology for the Estimation of Piezoelectric Coefficients of Poled Piezoelectric Materials", Electrochem. Solid State Lett. **13**, G108-G110 (2010).

[187] E. Uzgur, S.-S. Kim, E. Bryce, D. Hutson, M. Strachan, and K. Kirk, "Extension sensing of piezo actuators using time-domain ultrasonic measurement and

frequency-domain impedance measurement", Journal of Electroceramics **27**, 38-44 (2011).

[188] Boulder Nonlinear Systems, "http://www.bnonlinear.com/products/xyslm/XYSeriesDS0909.pdf", (2011).

[189] J. F. Ready, *Effects of high power laser radiation* (Academic, New York, 1971).

[190] BNS, "http://www.bnonlinear.com/products/xyslm/XY.htm", (2011).

[191] K. Gregorak, Boulder Nonlinear Systems (personal communication, 2010).